NTNU – Trondheim
Norwegian University of
Science and Technology

Design of a phased array antenna for a DVB-T based passive bistatic radar

Mathias Tømmer

Electronics System Design and Innovation
Submission date: June 2014
Supervisor: Egil Eide, IET
Co-supervisor: Idar Norheim-Næss, Forsvarets forskningsinstitutt

Norwegian University of Science and Technology
Department of Electronics and Telecommunications

Abstract

This thesis was initiated by the Norwegian Defence Research Establishment's project Military Air Surveillance. This project's work on passive radar systems has been ongoing for several years, recently on subject of DVB-T based passive bistatic radar. The main objective of this thesis is the design of a phased array antenna for a DVB-T based passive bistatic radar. Design specifications were derived based on the radar's required sectoral coverage and available DVB-T transmitters in the vicinity of the Oslo fjord. An 11 element horizontal linear array with dual polarized elements was found suitable, ensuring maximum directivity in the horizontal plane where scanning is performed. The bandwidth of the array should at least cover DVB-T channels 40-52, corresponding to 622-726 MHz.

A crossed bowtie antenna was found suitable as an array element, and modelling and simulations were done using CST Microwave Studio. The resulting simulated bandwidth was from 624-748 MHz for the horizontally polarized elements, and 600-800 MHz for the vertically polarized, with an input reflection coefficient below -10dB. In terms of radiation patterns, the center element of the array showed a half-power beamwidth in the horizontal plane of 122° and 130° for the horizontally and vertically polarized elements respectively. In the vertical plane, the corresponding beamwidths were 120° and 88°. When the array was scanned, the grating-lobe free scan range was $\theta_s = \pm 50^\circ$ at the highest achieved operating frequency of 750 MHz, where the active reflection coefficient at the center element was below -7dB throughout the whole band when scanned to this angle.

In order to validate the results from the simulations in CST, a 5-element prototype array was produced with the objective of comparing measured results with the corresponding results from CST simulations on a 5-element array. The hypothesis was that if the measured performance on the prototype array was within acceptable limits of the simulated results, then one can presume that a full 11 element array will perform according to the simulation results above. The center element of the 5-element array showed almost identical performance in terms of radiation patterns for both horizontal and vertical polarization, however with higher level of cross polarization. A 30 MHz shift in the center frequency was found in the measurements and it was found that this shift most likely stems from the fact that the quarter-wave balun used in the prototype was not included in CST simulations. Apart from this, the measurements on the prototype suggests that the simulation results on the 11 element array in CST can be expected from an 11 element prototype array. Thus serving as a motivational factor to build a full 11 element array and characterize it through measurements.

To summarize, the designed phased array antenna can potentially be used in a DVB-T based passive bistatic radar, covering channels 40-55 with a horizontal plane scan range of $\pm 50^\circ$. For future work it is recommended that the issue related to the frequency shift is sorted out, and that another row of elements stacked vertically is considered to reduce the vertical plane beamwidth. This increases the arrays total directivity, thus increasing the radar sensor detection range.

Sammendrag

Denne masteroppgaven ble gitt i forbindelse med Forsvarets Forskningsinstitutt (FFI) sitt prosjekt Luftmilitær Overvåkning, der hovedmålet med oppgaven er å utlede spesifikasjonen til- og designe en fasestyrt gruppeantenne til bruk i en DVB-T basert passiv bistatisk radar. Den passive radarsensoren er tiltenkt brukt i området rundt Oslofjorden med en horisontal overvåkningssektor på 90° med 45° vertikal dekning. Båndbredden til sensoren må dekke noen av de kanalene som brukes av DVB-T sendere i dette området og kanalene 40-52 ble satt som et passende mål, noe som tilsvarer 622-726 MHz. Da det skal gjøres digital beamforming i horisontalplanet med en 11-kanals radarmottaker, ble en lineær gruppeantenne på 11 to-polariserte elementer funnet passende. Dette gir maksimal antennevinning og høyest vinkeloppløsning i horisontalplanet. En krysset *bowtie* antenne ble valgt som et passende element da dette er bredbåndig og gir både horisontal og vertikal polarisering. Som simuleringsverktøy i oppgaven ble CST Microwave Studio brukt.

Simuleringene i CST viste en båndbredde på 624-746 MHz for de horisontalpolariserte elementene og 600-800 MHz for de vertikalpolariserte. Dette med en refleksjonskoeffisient på inngangen under -10 dB. Når det kommer til strålingsdiagrammet for senterelementet var strålebredden i horisontalplanet 122° og 130° for henholdsvis horisontal og vertikal polarisering. I vertikalplanet var strålebredden tilsvarende 120° og 88°. Når gruppeantennen ble fasestyrt var det mulig å styre hovedloben ut til $\theta_s = \pm 50^\circ$ ved den høyeste arbeidsfrekvensen på 750 MHz uten at gitterlober dukket opp. Ved denne vinkelen var den aktive refleksjonskoeffisienten for senterelementet maksimalt -7 dB i hele båndet. For å verifisere gyldigheten til simuleringsresultatene fra CST ble en prototype bygget. Med en plassbegrensning i det ekkofrie rommet på NTNU ble kun en gruppeantenne med 5 elementer produsert. Min hypotese var at dersom resultatene fra simuleringer i CST på en gruppeantenne med 5 elementer stemmer overens med målinger på en prototype, så vil en produsert fullstendig gruppeantenne på 11 elementer også ha tilnærmet lik ytelse som simuleringsresultatene tilsier.

Måleresultater fra senterelementet i prototypen stemte godt overens med de simulerte resultatene fra CST. Strålingsdiagrammene for både horisontal og vertikal polarisering var mer eller mindre like de fra simuleringene, sett bort i fra en økning i nivået av krysspolarisering. Fra impedansmålingene ble det oppdaget et skift i senterfrekvens på 30 MHz, og det ble konkludert med at grunnen til dette var at kvartbølgebalunen som ble brukt i prototypen ikke ble inkludert i simuleringene i CST. Sett bort i fra dette var resultatene i prototypen såpass like de simulerte resultatene at man kan anta at et fullt array med 11 elementer vil ha noenlunde lik ytelse som simuleringsresultatene tilsier.

Den fasestyrte gruppeantennen kan potensielt bli brukt i en DVB-T basert passiv bistatisk radar og dekker kanalene 40-55 med fasestyring i horisontalplanet ut til $\pm 50^\circ$. For fremtidig arbeid vil jeg anbefale at problemet relatert til frekvensskiftet i prototypen blir løst, og at det burde vurderes å ha to rader med elementer for å redusere strålebredden i vertikalplanet, øke den totale antennevinningen og dermed øke deteksjonsrekkevidden for radarsensoren.

Preface

This thesis is submitted for the degree of Master Of Science (MSc) at the Norwegian University of Science and Technology. The work was carried out in the period January to June 2014 under the supervision of adjunct associate professor Egil Eide (NTNU) and Idar Norheim-Næss, researcher at the Norwegian Defence Research Establishment (FFI). The assignment was given by FFI as a part of the Military Air Surveillance project as a part of a work on modern air surveillance technology.

I thank FFI for giving me the opportunity to work with this project and especially my supervisor at FFI, Idar Norheim-Næss, for supplying me with the equipment and tools needed to solve the assignment. His continuous feedback and support throughout the whole process has been invaluable for me, and for that I am very grateful. I thank Egil Eide, my supervisor at NTNU for encouraging me through the process and assisting me with the antenna design and I wish to thank the staff at the mechanical workshop at the Department of Electronics & Telecommunication; Tore Landsem and Tore Berg for helping me realize the prototype in such short notice. Last, but not least, I wish to thank Terje Mathiesen, senior engineer at the Department of electronics and telecommunication for assisting me in the whole prototype process; from purchasing the parts needed for the prototype and assisting me in the installation.

Trondheim, Norway, June 2014
Mathias Tømmer

Contents

List of Tables

List of Figures

Chapter 1

Introduction

1.1 Passive radar

Passive bistatic radar (PBR), passive covert radar (PCR) and passive coherent location (PCL) are all common names for passive radar systems exploiting transmitters of opportunity as their source of target illumination. Examples of such transmitters are terrestrial audio and TV broadcasting services such as FM, DAB and DVB-T, which covers large areas with high power transmitters. The term *passive* is due to the fact that the radar sensor does not have a dedicated transmitter and only requires a high performance receiver to detect and track targets, making it less vulnerable against radar jamming techniques. The geometry is bistatic due to the spatial separation of the transmitter and receiver, and when multiple transmitters and/or receivers are used, the situation simply becomes multistatic. In a passive radar system target detection is based on the cross-correlation between the direct signal from the transmitter being exploited and the scattered signals from one or multiple targets. These signal paths are illustrated in Figure 1.1, where the received signal is a combination of both reflected signals from a target, the direct signal and multipath components of the direct signal (reflected and diffracted).

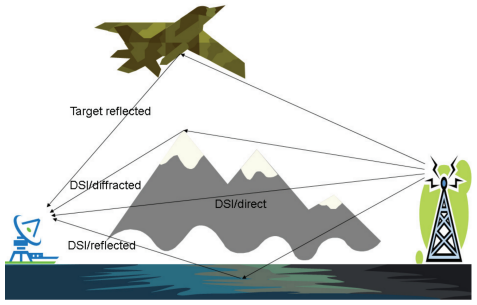

Figure 1.1: Passive bistatic radar signal paths, where both target reflection and multipath components of the direct signal can complicate the signal processing, from [1]

1.2 History

On a historical point of view the passive bistatic radar dates back to 1935, when Robert Watson-Watt and Arnold Frederic Wilkins conducted the Daventry experiment. A demonstration of their concept of aircraft detection. The transmitter of opportunity was the BBC Empire short-wave station at Daventry which operated at 6 MHz with a total of 10 kW transmitted power. Wilkins considered a monoplane bomber with a wing-span of approximately 25 metres ($\lambda/2$ at the frequency of the Daventry transmitter), as a plausible target. The Daventry transmitter antenna was an array of horizontal dipoles, producing a beamwidth of 60° in azimuth and 10° in elevation, with the main lobe directed towards the south. The experiment was carried out by positioning the receiver at a suitable distance away from the Daventry transmitter and outside its main lobe. When the Heyford bomber flew up and down into the transmitter beam, Watt & Wilkins noticed fluctuations in the received signals as the aircraft flew by, indicating a variable and measurable amount of reflected radio signals from the passing aircraft [4, p.28]. This experiment and further work culminated in the Chain Home early warning radar system. A chain of radar transmitters and receivers along the south and east coast of England, operating at a frequency between 20 and 30 MHz, transmitting 350 kW. One of the Chain Home installations is shown in Figure 1.2.

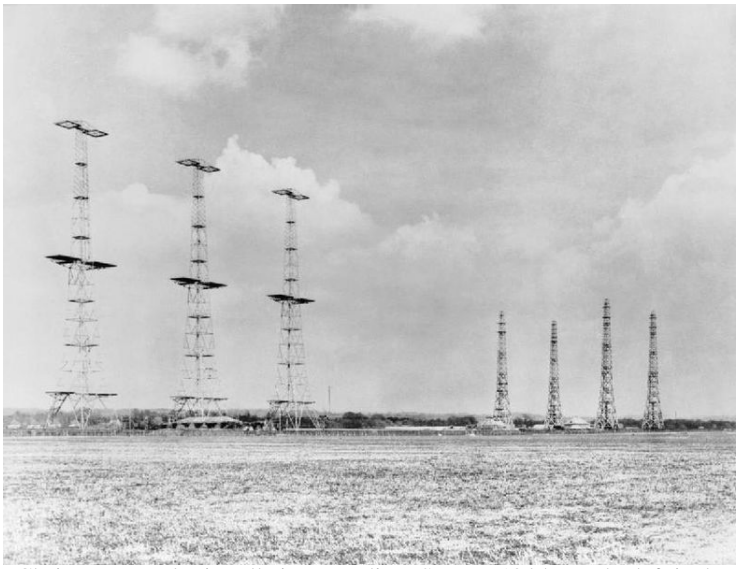

Figure 1.2: Chain Home radar installation at Poling, Sussex, 1945. To the left is three 110m tall transmitter towers, and to the right is four 73m tall receiving towers in a rhombic formation. From [2]

During World War II the Germans developed a passive bistatic radar known as Klein Heidelberg, which *exploited* the Chain Home radars as transmitters of opportunity. This was actually the first first operational passive bistatic radar using non-cooperative transmitters. Figure 1.3(b) illustrates the geometry of a Klein Heidelberg receiver located in Oostvoorne exploiting a Chain Home radar transmitter in Dover (baseline L). An incoming aircraft is detected and its location lies somewhere on the ellipse illustrated and absolute position is found by solving the bistatic triangle consisting of the baseline L and the transmitter-target-receiver path $R_t + R_s$. The Klein Heidelberg passive radar was distributed along the coast and used a planar antenna array with six-by-two dipole antennas located in front of a reflector plane [10], as shown in Figure 1.3(a).

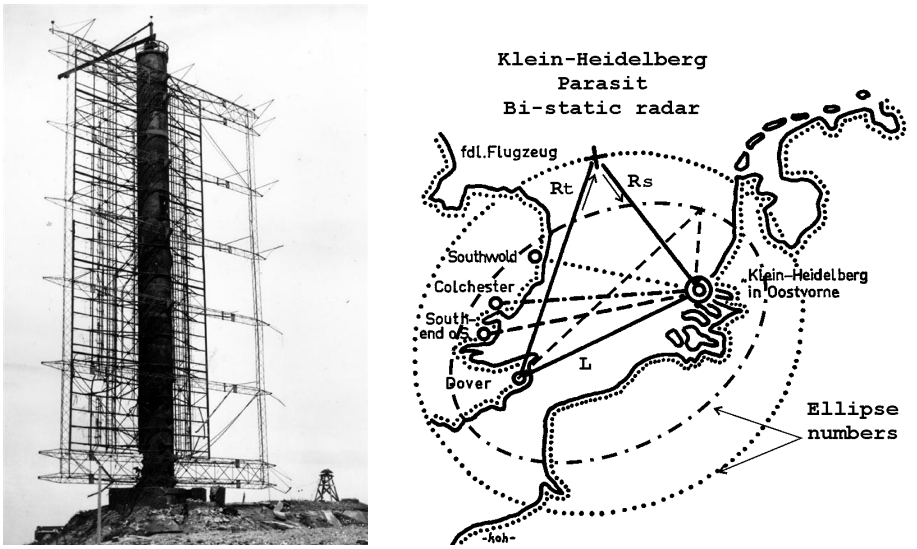

(a) (b)

Figure 1.3: a)The Klein Heidelberg antenna array [3] and b);a diagram of the principle of Klein Heidelberg showing a receiver at Oostvoorne using a transmission from a Chain Home radar at Dover. A measurement of the bistatic range $R_T + R_s$ defines an ellipse on which the target lies [3]

Since that time, the interest for passive radar systems has been going in cycles with a periodicity of 15 to 20 years and is at the moment at a wide peak. This is mostly due to the rapidly emerging PBR technology being at an acceptable performance-vs-cost level and the radar's potential as a sensor for military air surveillance[1]. Two well-known commercially available PBR systems are Silent Sentry 3 from Lockheed Martin (Fig. 1.4(c)) and Homeland Alerter 100 from Thales (Fig. 1.4(d)) which are both FM-based passive radar systems. The next generation of PBR systems exploit digital audio (DAB) and TV (DVB-T) broadcasts with increased channel bandwidth (8 MHz DVB-T versus 200 kHz FM), yielding higher range resolution. Examples of such systems are Aulos from Selex (Fig.1.4(a)) and Silent Guard from ERA (Fig. 1.4(b)) which exploits both FM and DVB-T transmitters.

(a) Selex Aulos, photo: Selex

(b) ERA Silent Guard, photo: ERA

(c) Lockheed Martin Silent Sentry, photo: Lockheed Martin

(d) Thales HA-100, photo: Thales

Figure 1.4: Four commercially available FM based passive radar systems

1.3 Motivation and goals

The Norwegian Defence Research establishment's (FFI) work on passive radar systems has been ongoing for several years with multiple published papers on FM based passive bistatic radar [11][12]. Most recently on the utilization of terrestrial digital video broadcasts (DVB-T) in passive bistatic radar to detect airborne low-flying targets [13][14][15]. From a military aspect, this passive radar may serve as a gap filler covering areas where the long-range active radars does not suffice, and since the system is passive there is no limitation on deployment sites due to RF emissions. Deployment sites can be chosen more or less based on available transmitters of opportunity and the surrounding landscape. One of the major limitations in passive bistatic radar is the detection of a weak target echo in the presence of strong direct signal from the transmitter being exploited. This interference is often referred to as direct-signal interference (DSI) which must be reduced in order to detect weak targets. One method of direct-signal cancellation is to use digital beamforming techniques on an antenna array and placing nulls in the radiation pattern in the direction of the transmitter being exploited.

FFI has a goal of conducting bistatic and multistatic measurements on a DVB-T based passive radar system in the Oslo fjord area, using digital beamforming techniques on an antenna array to reduce the DSI. A 12 channel superheterodyne receiver developed at Fraunhofer FHR capable of beamforming and PBR signal processing is available, making it possible to form 11 simultaneous surveillance beams when one channel is used as reference channel. Common for the commercial passive radar systems in Figure 1.4 is that they all utilize circular antenna arrays in order to obtain a full 360° horizontal surveillance sector. With 11 channels available for surveillance, FFI wants to reduce the surveillance sector to 90° horizontally and 45° vertically to obtain higher antenna gain and greater radar range according to the bistatic radar equation Eq.(2.4). The beamforming takes place in the horizontal plane, where all the beams are packed into the 90° sector to obtain higher angular resolution.

Figure 1.5 illustrates a hypothetical radar sensor deployed at Mågerø and FFI respectively, showing the different DVB-T transmitters in the vicinity of the Oslo fjord. Most of these transmitters are located high up in the terrain, transmitting between 30 and 60 kW, ensuring target illumination all the way down to ground level. With an estimated range of 50 km in a 90° horizontal surveillance sector, the color coding shows the height above ground level at which the two receivers has a line of sight (LOS), based on terrain profiles. A sensor located at Mågerø has a LOS down to 10 metres above sea level across the fjord and 50-100 metres otherwise. The sensor located at FFI is somewhat more restricted by terrain shielding, where the line of sight at 50 km is between 400 and 3000 metres in the upper part of the Oslo fjord.

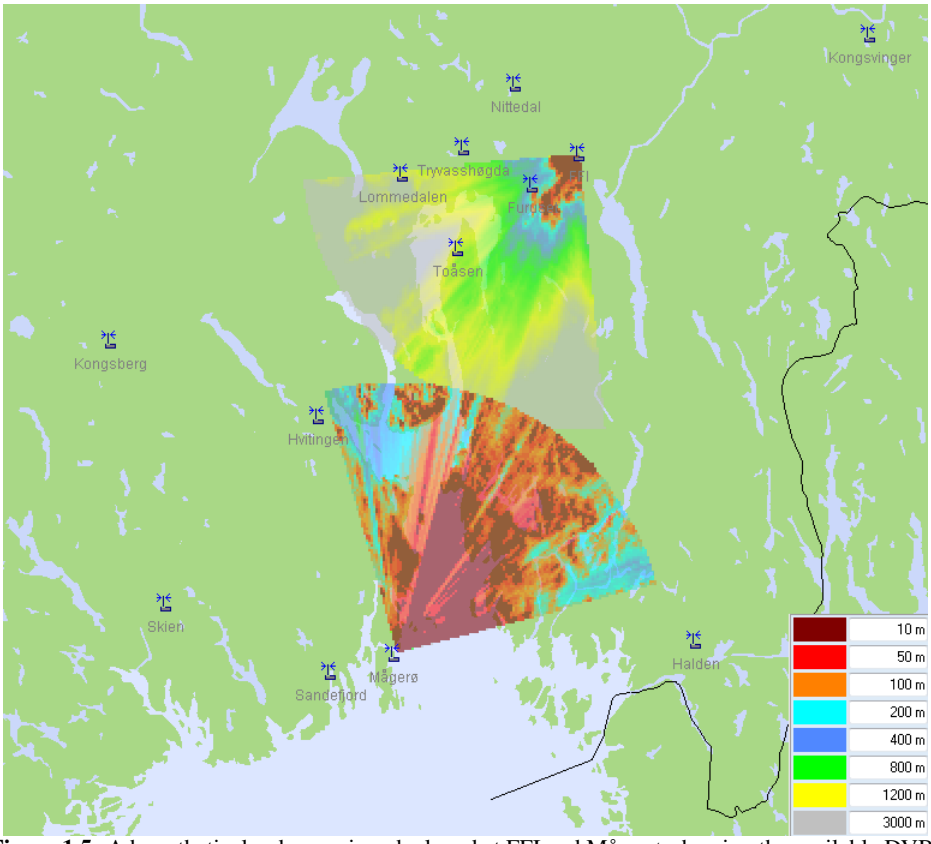

Figure 1.5: A hypothetical radar receiver deployed at FFI and Mågerø, showing the available DVB-T transmitters surrounding the Oslo fjord. A 90° surveillance sector is shown with an estimated range of 50 km. The color coding indicates the height at which the receiver has line-of-sight

The goal of this thesis is to derive the specifications and design an antenna array suitable for this application. Each antenna element must have a unidirectional radiation pattern with a half-power beamwidth of 90° in the horizontal plane and 45° in the vertical plane. The bandwidth should cover at least two, preferable three DVB-T channels in the single-frequency networks in the vicinity of the Oslo fjord and the solution should be as low cost as possible.

Chapter 2

Background Theory

The purpose of this chapter is to provide a short overview of the theoretical background on passive bistatic radar and the utilization of DVB-T transmitters as sources of target illumination. Furthermore, a short introduction to the theory of linear antenna arrays is provided and finally, a brief description of the simulation tool used in the thesis is given.

2.1 Passive Bistatic Radar

A passive bistatic radar (PBR) operates with spatially separated transmitter and receiver, and exploits transmitters of opportunity as its source of target illumination. Common transmitters utilized for this application are terrestrial broadcasting services covering large areas with high power transmitters, such as analog or digital audio and TV broadcasts. One of the primary motivations for military applications is detection and tracking of low flying aircrafts, and that the system can be made low-cost since there is no need for a dedicated radar transmitter. However, the advantages are limited due to more complex geometry where topography may limit the the number of useful deployment sites, in e.g. where a mountain limits the sensors field of view. If at the same time the transmitter being exploited is non-cooperative, there is no control of the transmitted signal, making the signal processing more complex and raising the need for a high performance receiver [16].

2.1.1 Geometry and target location

The geometry and signal propagation paths of a bistatic radar is shown in Figure (2.1) with a north-referenced coordinate system [4, p.71]. The direct path between the transmitter and receiver is often referred to as the baseline with length L, while R_T and R_R denotes the distances between the transmitter and target, and receiver and target respectively. The bistatic radar measures the time-difference of arrival (TDOA) τ between the direct signal from the transmitter and the signal scattered from the target. If the transmitter and receiver locations are known, the baseline L can be estimated and the bistatic range sum $R_T + R_R$ can be calculated using equation (2.1) [4, p.86]

$$(R_T + R_R) = c\tau + L \tag{2.1}$$

The measured range sum $R_T + R_R$ constitutes an ellipse (in the 2D bistatic plane) with focal points at the transmitter and receiver locations as shown in Figure (2.2(a)). Each ellipse corresponds to all possible target locations in the bistatic plane of figure (2.1) and is often referred to as an isorange contour or a contour of constant range sum, and each target echo generates such an ellipse in the receiver [1, p.57].

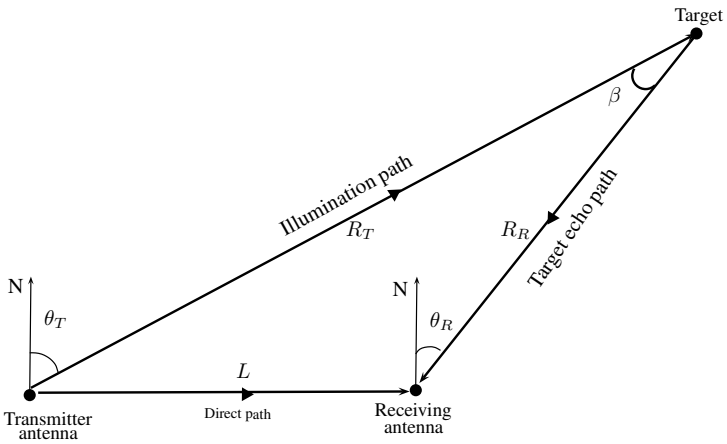

Figure 2.1: Passive bistatic radar geometry showing the paths of the transmitted and reflected signals, North-referenced coordinate system from [4]

The isorange contours in Figure 2.2(a) only gives information on all possible target locations. To be able to resolve the targets position in the bistatic plane, one can use an estimate of the direction in which the target echoes arrive at the receiver (θ_R in figure (2.1)). This is often referred to as the direction-of-arrival (DOA). With an estimate of the target echo's DOA (θ_R) and the bistatic range $R_T + R_R$, the location of the target can be calculated using Equation (2.2), assuming L is known [4, p.65].

$$R_R = \frac{(R_T + R_R)^2 - L^2}{2(R_T + R_R + L\sin\theta_R)} \tag{2.2}$$

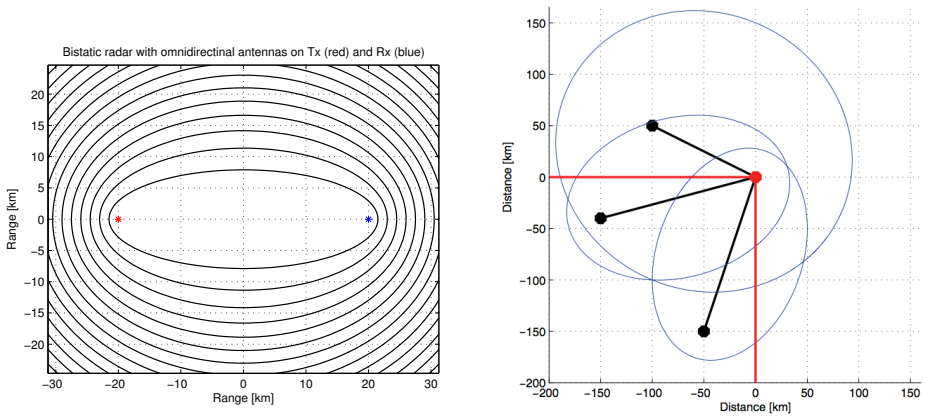

(a) (b)

Figure 2.2: **(a)** Isorange contours where each contour corresponds possible target locations in the bistatic plane based on the measured target echo TDOA [1], **(b)** Multistatic radar system with three transmitters(black dots) and one receiver (red dot), where a target is present at position (-100km,-100km). The target's constant range profile is drawn for each of the three transmitter-receive pairs (black lines), also showing three ghosts. The red line indicate a quadrant with respect to the receiver, mimicking coarse DOA estimation at the receiver [1, p.60]

When there exist multiple transmitters being exploited or multiple spatially separated receivers are deployed, the situation becomes multistatic. Figure 2.2(b) depicts this situation with one receiver and three transmitters (black dots), where the receiver now receives both direct signal and target echo from each transmitter simultaneously. For each transmit/receive pair there exists a corresponding isorange contour (blue ellipses) from the three measured TDOA's. This results in multiple intersection points of the three isorange contours, where the intersections *not* corresponding to real targets are referred to as ghosts. The maximum number of ghosts [4] $f(M,T)$ in the simplified 2D situation generated by T targets and M transmit-receive pairs is given by equation (2.3).

$$f(M,T) = (2T^2 - T)(M^2 - M)/2 \tag{2.3}$$

The number of ghosts could be drastically reduced if an indication of the target direction is available. Yet again, an estimate of the target echo's DOA (θ_R) prove useful, where even a coarse estimate would decrease the number of ghosts and provide the target range from Eq. (2.2). Estimating the DOA in figure (2.1) can be done using digital beamforming techniques on an antenna array [1].

2.1.2 Performance and limitations

The bistatic radar equation is analogous to that of the monostatic case and can be used to predict the performance of a passive radar system and is given as[16]

$$\frac{P_r}{P_n} = \frac{P_t G_t}{4\pi {R_T}^2} \sigma_b \frac{1}{4\pi {R_R}^2} \frac{G_r \lambda^2}{4\pi} \frac{1}{kT_0 BF} L \tag{2.4}$$

where

- $P_t =$ Received signal power $[W]$,
- $P_n =$ Received noise power $[W]$,
- $P_t =$ Transmitter power $[W]$,
- $G_t =$ Transmitter antenna gain,
- $R_T =$ Transmitter-to-target range $[m]$,
- $\sigma_b =$ Target bistatic radar cross-section $[m^2]$,
- $R_R =$ Target-to-receiver range $[m]$,
- $G_r =$ Receiver antenna gain ,
- $\lambda =$ Signal wavelength $[m]$,
- $k =$ Boltzmann's constant $[J/K]$,
- $T_0 =$ Noise reference temperature $[K]$,
- $B =$ Receiver effective bandwidth $[Hz]$,
- $F =$ Receiver effective noise figure,
- $L(< 0) =$ System losses

Details on the different parameters and their effect on the bistatic radar performance can be found in [16].

The receiver in figure (2.1) attempts to detect an echo from a target in the presence of a strong direct signal from the transmitter being exploited. This direct signal can be 80 to 90 dB greater in magnitude than the target echo [16]. Other noise and interference sources degrading the radar performance are reviewed by Griffits and Baker in [17]. As Howland [18] stated

> "The greatest limitation on system performance is the interference received from the transmitter being used to detect aircraft. This unwanted direct signal correlates perfectly with the reference signal and produces range and Doppler side lobes that are several orders of magnitude greater than the echoes that are sought. To detect anything but the closest of targets it is necessary to remove this signal, by both angular nulling with the antenna and adaptive echo cancellation in the receiver. However, eventually the dynamic range of the receiver limits the cancellation and so the principal limitation on system performance lies with the analogue-to-digital converter technology."

It is therefore of utmost importance to reduce the direct signal interference in a passive bistatic radar. Different methods of reducing the direct signal interference have been reported in literature [17][18], using physical shielding, spatial cancellation and spectral methods. Physical shielding is an effective and low cost alternative and can be be done using radar absorbent materials or by deploying the receiver on a site shielded from the transmitter by topography [17][18]. These methods limit the antenna's field of view resulting in only sectoral coverage, which may or may not be a desired effect. Spatial cancellation methods involves placing the antenna so that the direct signal path is within a null or low side lobe in the antenna radiation pattern [18], or by using analog or digital beamforming on an antenna array. The first method of spatial cancellation requires the radiation pattern null to be broadband, while the latter is limited by the ability to create nulls and control the radiation pattern of the array either in an analog or digital fashion. Digital beamforming techniques have been studied extensively over several decades in both radar and communication systems and the beamforming can be done by the means of a digital signal processor. With adaptive beamforming techniques one can adjust for non-stationary effects caused by changes in the signal environment[16].

2.1.3 Signal Processing Scheme

Figure 2.3 illustrates a generic signal processing scheme for a passive radar system, proposed by Paul Howland [5]. At first the system consists of two separated channels, a reference channel which records the direct signal from the transmitter being exploited, and a surveillance channel. The antenna used for the reference channel should be as directive as possible in order to obtain a good reference signal, while the antenna array making up the surveillance channel should cover the desired field-of-view and be suitable for digital beamforming.

The beamformer, be it analog or digital, needs to be able to form wide nulls in the radiation pattern of the antenna array in the direction of the direct-signal interference and its multipath components. By using an array of N-elements one have the ability to form *N* main beams steered to cover the desired field-of-view, where each beam can have *N-1* nulls steered to the direction of interfering signals[19, p.3], reducing the direct-signal interference in the surveillance channel. It should also be mentioned that the antenna array can also be used to generate a beam pointing towards the transmitter, where this beam represents the reference channel. Both Lockheed Martin's Silent Sentry and Thales Home Alerter 100 use this technique.

Signal conditioning is applied to do channel equalization to improve the reference signal and remove unwanted structures in the digital signals to improve the radar ambiguity function, and possibly reconstruction of the received signal. After an adaptive cancellation block removing any additional direct-signal interference from the surveillance channel, the cross correlation between the reference and surveillance channel takes place. It is the cross-correlation step which makes the basis for target detection, producing range-Doppler surfaces where the targets are detected. The results are follows by a line tracker after CFAR detection. Details on any of the blocks except for the antenna array will not be given, as it is not within the scope of this report.

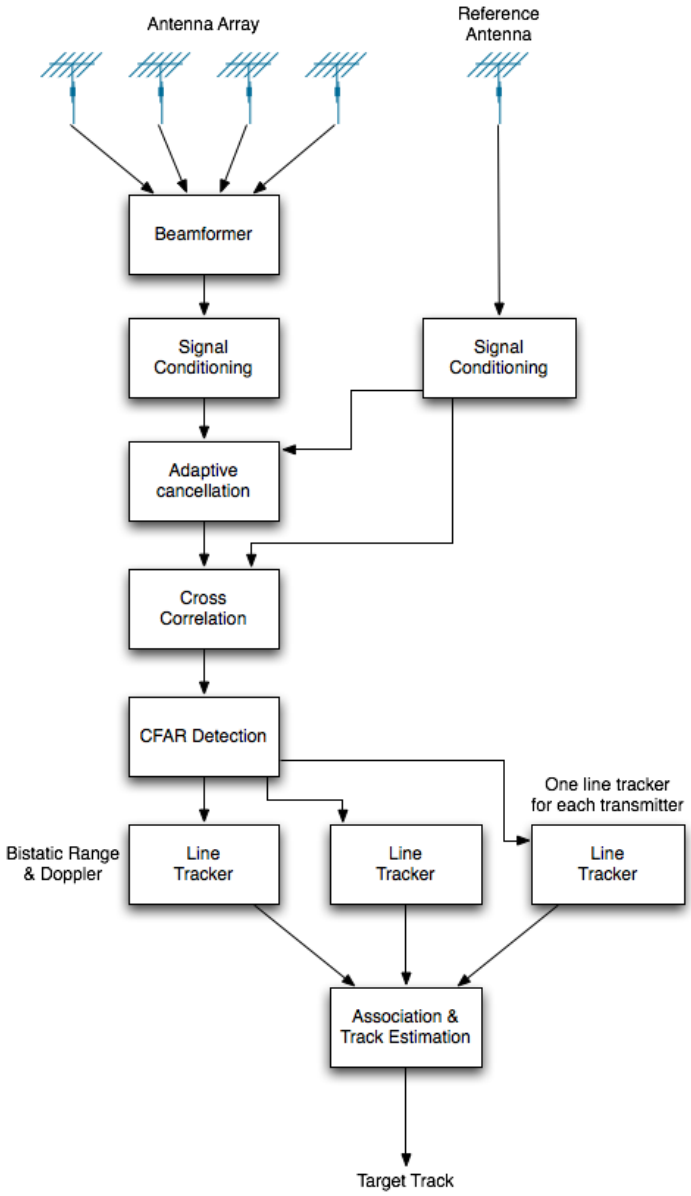

Figure 2.3: A generic passive radar signal processing scheme, from [5]

2.1.4 Exploiting DVB-T transmitters in PBR

There exists multiple terrestrial broadcasting services in the VHF and UHF frequency bands which could be exploited in a PBR system, such as FM, DAB and DVB-T. This part of the spectrum is not normally available for radar purposes and stealth treatment of targets may be less effective at these frequencies [16] [20]. The DVB-T frequency band in Norway covers 470 - 790 MHz and the signal is described by the ETSI standard *EN300744*. Each channel is 8 MHz wide coded OFDM (COFDM) with carriers modulated with either 16/64 QAM or QPSK. Compared to the FM signals which are narrowband and have bandwidth fluctuating with the information, the DVB-T signal has a wide and constant bandwidth. Figure 2.4 shows the spectrum of one channel averaged over two seconds, where the peaks are due to constant pilot carriers.

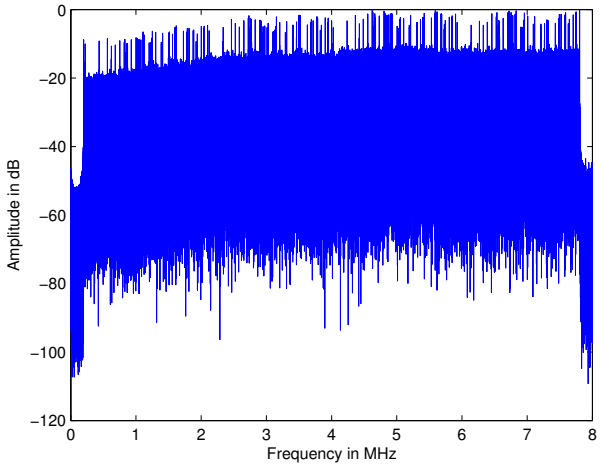

Figure 2.4: DVB-T channel spectrum averaged over 2 seconds[6]

Transmitters around the country constitutes multiple single-frequency networks (SFN), where multiple transmitters operating at the same frequency serves the same area to enhance coverage. This is possible due to the cyclic prefix in the DVB-T signal which acts as a guard interval, where the duration of the guard interval is equal to the maximum propagation delay between the transmitters.

As discussed earlier, when there exists multiple transmit/receive-pairs, erroneous target detections due to target ghosts can occur. For a PBR exploiting a transmitter in a single-frequency network, ghosts can appear due to another transmitter broadcasting the same signal. This further emphasizes the need for null-steering on the antenna array to reduce the DSI from not only the transmitter being exploited, but also other transmitters in the same SFN.

A list of some transmitters near the Oslo fjord and their channel frequencies is given in Table 2.1 below.

Table 2.1: Transmitters and channels in close proximity to Oslo

Transmitter	Channel	Frequency (MHz)	Transmitted power (W)
Tryvasshøgda	30	546	33884
	40	626	33884
	46	674	33884
	52	722	33884
	57	762	1000
	58	770	33884
Jonknuten	34	578	50119
	43	650	50119
	44	658	50119
	51	714	50119
	60	770	50119
Kongsvinger	24	498	44668
	28	530	44668
	41	634	44668
	48	690	44668
	55	746	44668
Skien	24	498	39811
	34	578	39811
	44	658	39811
	54	738	39811
	60	786	39811
Halden	21	474	63096
	34	562	63096
	38	610	63096
	42	642	63096
	45	666	63096

2.2 Antenna arrays

In a radar system, the antenna acts as a transducer between the system's transmission lines and free-space propagating radio waves, defining the radar's field-of-view and angular resolution. When a radar is transmitting, the main purpose of the antenna is to focus as much energy as possible in a given direction within the surveillance sector to illuminate possible targets. When it is switched back to receiving mode to listen for an echo, the antenna must collect as much of the backscattered energy as possible from the same direction while suppressing interference from others. In order to do this a highly directive radiation pattern is required. In fact, almost all radars use antennas with high directivity [21, p.539].

In the bistatic radar equation, Eq.(2.4), the gain G_t & G_r of the transmitting and the receiving antenna have major influence on the performance in terms of received signal SNR. Increasing the gain of the antennas increases the range of the radar as well as the probability for target detection. For the passive bistatic radar in Figure 2.1 both transmitted power P_t and transmitter antenna gain G_t are fixed by the transmitter being exploited. Terrestrial broadcasting services the radiation patterns are usually omnidirectional in azimuth with some beam suppression in elevation to ensure ground coverage and not wasting too much energy by transmitting upwards. For a radar receiver with a fixed minimum SNR to detect targets, the range of the radar can be extended by increasing the gain of the receiving antenna G_r. The only way to increase the radar antenna's gain is by increasing its electrical size [7, p.283], which can be done using a large reflector antenna or by grouping multiple antennas together to form an antenna array.

Antenna arrays offer multiple degrees of freedom and are often utilized in modern radar systems to give some form of control over the radiation pattern. By controlling the amplitude and phase excitation of each element in the array, one has the ability to form the radiation pattern and steer the main lobe (direction of maximum radiation) to arbitrary angles. This is known as a phased array, where the main lobe direction is determined by the element phase excitation and the amplitude excitation controls the shape of the radiation pattern. There are no limitations to element arrangement in antenna arrays, however they are usually linear, planar (as shown in Figure 2.5) or circular and the elements within the array are often identical and uniformly spaced.

An example of a large phased array radar is shown in Figure 2.5. The 11-story tall phased array radar at Clear Air Force Station, constructed in 1978 serves as a system for missile warning and space surveillance, operating at frequencies between 420 and 450 MHz. The array contains two faces with a total of *2677* crossed dipole elements arranged in a triangular lattice, however only 1792 elements are connected to a transceiver and the rest are dummy elements. The faces are tilted 20° to reduce ground clutter and allow for an elevation coverage from 3° to 85°, where the two array faces result in a total surveillance sector of 240° in azimuth . The active antenna elements in the array are connected to a complex network of exciters, signal processors, radar controllers, beam steering units and communication equipment [22]. To further illustrate one of the primary motivations for phased arrays, imagine how a large structure as this could be rotated in both azimuth and elevation to steer the main beam. It would simply be impractical.

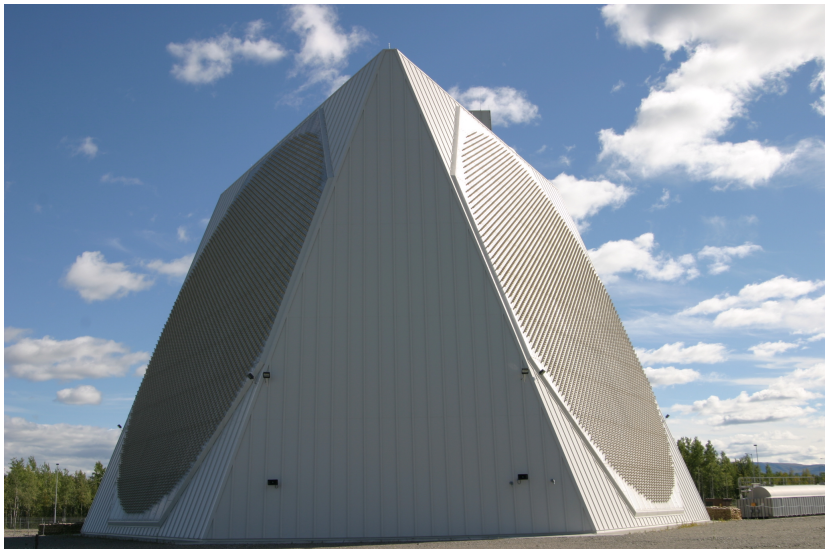

Figure 2.5: 11-story tall phased array radar (PAVE PAWS) at Clear Air Force Station used for missile warning and space surveillance

The analysis of antenna arrays of different geometries and elements have been extensively covered in literature [7][23][24]. Only a simplified analysis on linear antenna arrays is presented here to illustrate the concept and its limitations. Even though the array analysis is for an array in transmitting mode, the results are equally valid for a receiving array through the principle of reciprocity.

2.2.1 Linear array

Figure (2.6) illustrates a linear array of N identical elements (black dots) located on the x-axis, equally spaced with an inter-element spacing d. For simplicity all the elements are assumed to occupy an infinitesimal volume and that there exist no interaction between the elements, such that each element behaves as if they were isolated.

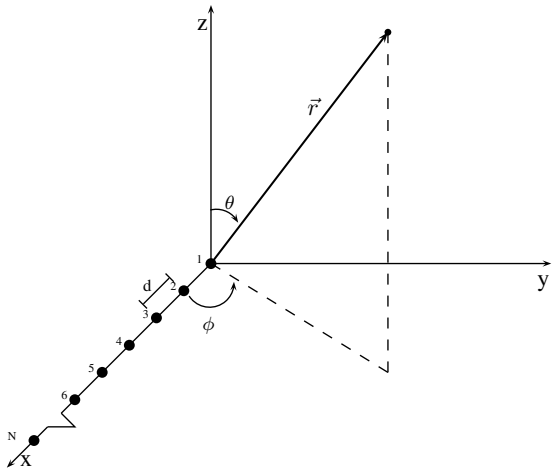

Figure 2.6: Geometry of a linear antenna array with N infinitesimal elements along the x-axis with an inter-element spacing d

The total radiated electric field from the array $\mathbf{E_t}$ is found from the superposition of the fields radiated by each element, and under the assumption of linear elements (such as the dipole antenna), the electric field radiated by the i'th element in the array can be expressed as

$$\mathbf{E_i}(\theta, \phi) = A_i \frac{e^{-jkr_i}}{r_i} \mathbf{E_e}(\theta, \phi) \tag{2.5}$$

where A_i is the complex excitation coefficient (both amplitude and phase) of the element, $\mathbf{E_e}(\theta, \phi)$ is the radiation pattern of the element, $k = 2\pi f/c$ is the wavenumber and r_i is the distance between the element and the observation point $p(r, \theta, \phi)$. The total radiated electric field from the array is then expressed as the sum of the radiated field from each element and is given by Eq. (2.6) [23, p.6].

$$\mathbf{E_t} = A_1 \frac{\exp(-jkr_1)}{r_1} \mathbf{E_e}(\theta, \phi) + A_2 \frac{\exp(-jkr_2)}{r_2} \mathbf{E_e}(\theta, \phi) \cdots + A_N \frac{\exp(-jkr_N)}{r_N} \mathbf{E_e}(\theta, \phi) \tag{2.6}$$

Since the elements in the antenna array are spatially separated, the radial distance r_i between the i'th element and the observation point in space is not identical for each element in the array. As the radial distance increases the difference due to the spatially separation of the elements decreases, and since we are only interested in the far-field radiation of the antenna array, the far-field approximation can be applied. Looking at the radial distance terms r_i in Equation (2.6), there is one associated with the amplitude of the radiated field and another with its phase (in the complex exponential). In the far-field approximation the terms associated with the amplitude is approximated as equal $r_i \approx r$, while the phase terms are approximated with Equation (2.7) [23, p.6]

$$r_i = r - (i-1)d\sin(\theta)\cos(\phi) \qquad i = 1, 2, \ldots, N \tag{2.7}$$

By expressing the element excitation as in Eq. (2.8)

$$A_i = a_i e^{j(i-1)\beta} \qquad i = 1, 2, \ldots, N \tag{2.8}$$

where a_i is the amplitude excitation of the element and β is the relative phase shift between the elements, then the total electric field radiated from the array can be written as Eq. (2.9)

$$\begin{aligned}\mathbf{E_t} = \mathbf{E_e}(\theta,\phi)\frac{\exp(-jkr)}{r}\Big[a_1 + a_2\exp(j[kd\sin\theta\cos\phi+\beta]) \\ \cdots + a_N\exp(j(N-1)[kd\sin\theta\cos\phi+\beta])\Big]\end{aligned} \tag{2.9}$$

The total radiated electric field from the array, Eq. (2.9),is the product between the isolated element behaviour and the factor within the brackets, where the latter is often referred to as the *array factor*. The array factor is dependent on the excitation of the elements (both amplitude and phase), the total number of elements N and the inter-element spacing d, and can be written as Eq. (2.10).

$$AF = \sum_{i=1}^{N} a_i e^{j(N-i)[kdsin\theta\cos\phi+\beta]} \tag{2.10}$$

Assuming we restrict ourselves to the X-Z plane in Figure 2.6 ($\phi = 0$) and by expanding the sum, the array factor can be re-written as Eq. (2.11) [7, p.293].

$$AF = \left[\frac{\sin\left(\frac{N}{2}\psi\right)}{\sin\left(\frac{1}{2}\psi\right)}\right] \tag{2.11}$$

where $\psi = kd\sin\theta + \beta$
Next, the directivity of the linear array will be derived since this is a commonly used performance parameter related to antennas.

2.2.2 Array directivity

The IEC definition of directivity is "the ratio of the radiation intensity in a given direction from the antenna to the radiation intensity averaged over all direction" [7, p.44], and can be expressed as

$$D(\theta) = \frac{U(\theta)}{U_0} = \frac{4\pi U(\theta)}{P_{rad}} \tag{2.12}$$

The directivity of the antenna is a measure on how the antenna focuses energy in different directions. For the linear antenna array, the total directivity can be found from the isolated element directivity and the array factor directivity from the property of pattern multiplication. For the linear array in Figure 2.6 the array factor radiation intensity U_{AF} can be written as Eq.(2.13) [7, p.314].

$$U_{AF}(\theta) = [(AF)_n]^2 = \left[\frac{\sin\left(\frac{N}{2}(kd\sin\theta+\beta)\right)}{\frac{N}{2}(kd\sin\theta+\beta)}\right] = \left[\frac{\sin(Z)}{Z}\right]^2 \tag{2.13}$$

where $Z = \frac{N}{2}(kd\sin\theta+\beta)$, and the averaged array factor radiation intensity is Eq.(2.14)

$$\begin{aligned} U_{AF_0} &= \frac{1}{2}\int_{\frac{-\pi}{2}}^{\frac{\pi}{2}} \left[\frac{\sin(Z)}{Z}\right]^2 \cos\theta \,\mathrm{d}\theta. \\ &= \frac{1}{Nkd}\int_{\frac{-N(kd-\beta)}{2}}^{\frac{N(kd+\beta)}{2}} \left[\frac{\sin(Z)}{Z}\right]^2 \mathrm{d}Z \\ &= \frac{1}{Nkd}\frac{2ZS_i(2Z)+\cos(2Z)-1}{2Z}\Big|_{\frac{-N(kd-\beta)}{2}}^{\frac{N(kd+\beta)}{2}} \end{aligned} \tag{2.14}$$

where $Si()$ is the sine-integral. The directivity is often given in dB by Eq.(2.15)

$$D_{AF}(\theta)_{dB} = 10\log_{10}\left(\frac{U_{AF}(\theta)}{U_{AF_0}}\right) \tag{2.15}$$

Figure 2.7 shows the array factor directivity D_{AF} for a linear array with 5 elements for three different inter-element spacings d and uniform amplitude and phase excitation. For each doubling of the inter-element spacing, the directivity is also doubled (+3dB). As the element spacing is increased to λ another maxima appears at $\pm 90°$, this is also known as grating lobes and will be discussed later. It should be noted that the array factor directivity is only plotted for $-90° \leq \theta \leq 90°$, however the array factor Eq. (2.11) is symmetrical around the array axis (x-axis ($\phi = 0$) in Fig. 2.6).

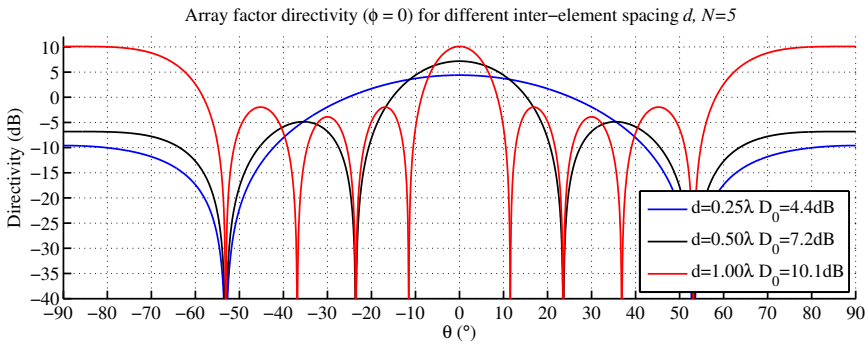

Figure 2.7: Array factor directivity for N=5 elements with different inter-element spacing, d and uniform amplitude and phase excitation. The maximum directivity D_0 is doubled for each doubling of element spacing d

Figure 3.3 below shows the array factor directivity for a given element spacing d and uniform amplitude excitation, with different number of elements N. Here it is seen that the maximum directivity D_0 is doubled for each doubling of elements. Both of these results is a direct consequence of doubling the aperture of the antenna array, resulting in twice the directivity.

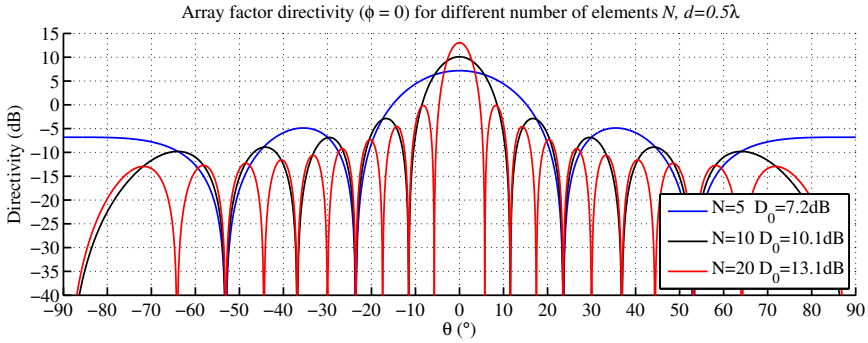

Figure 2.8: Array factor directivity for $d = 0.5\lambda$ elements with different number of elements N=5, N=10 and N= 20 and uniform amplitude excitation. As the number of elements is doubled, the maximum directivity is also doubled.

From both Fig. 2.7 and Fig. 3.3 the beamwidth decreases as the directivity increases. For a linear array with uniform amplitude excitation, the half-power beam width (HPBW) of the array factor, which is the beamwidth where the array factor directivity has dropped down 3 dB from its maximum, is given as Eq. (2.16)[7, p.300]. As the antenna array aperture is doubled (twice the directivity), the HPBW is approximately halved.

$$\Theta_h \approx 2\left[\frac{\pi}{2} - \arccos\left(\frac{1.391\lambda}{\pi N d}\right)\right] \tag{2.16}$$

2.2.3 Phased linear array

As mentioned earlier, by controlling the amplitude and phase excitation of the elements within the array according to Eq. (2.8), one can form the radiation pattern and steer the direction of maximum radiation to arbitrary angles. The array factor in Eq. (2.11) is at its maximum when $\psi = kd\sin\theta + \beta = 0$. For a linear array where all the elements are excited with the same phase ($\beta = 0$), then the array factor maximum is at $\theta = 0°$ as shown in Figure 2.7 and 3.3. The direction of maximum radiation can be steered to arbitrary angles by choosing a phase shift between neighbouring elements β according to Eq. (2.17).

$$\psi = kd\sin\theta + \beta\Big|_{\theta=\theta_s} \Rightarrow \beta = -kd\sin\theta_s \tag{2.17}$$

By inserting Eq. (2.17) into Eq. (2.11), the new array factor can be written as Eq. (2.18), which has its maximum at $\theta = \theta_s$.

$$AF = \left[\frac{\sin\left(\frac{N}{2}kd(\sin\theta - \sin\theta_s)\right)}{\sin\left(\frac{1}{2}kd(\sin\theta - \sin\theta_s)\right)}\right] \tag{2.18}$$

Due to the property of pattern multiplication in antenna arrays, the total array directivity can be found by multiplying the directivity of the antenna elements with the directivity of the array factor. This is illustrated in Figure 2.9, where the array consists of 10 horizontal dipole antennas located above an infinite ground plane with an element spacing $d = 0.5\lambda$. The array is excited with uniform amplitude and scanned to $0°$, $-20°$ and $-40°$. It can be seen from the figure that the total array directivity decreases with the element directivity, and the beam widt broadens as it is scanned away from broadside.

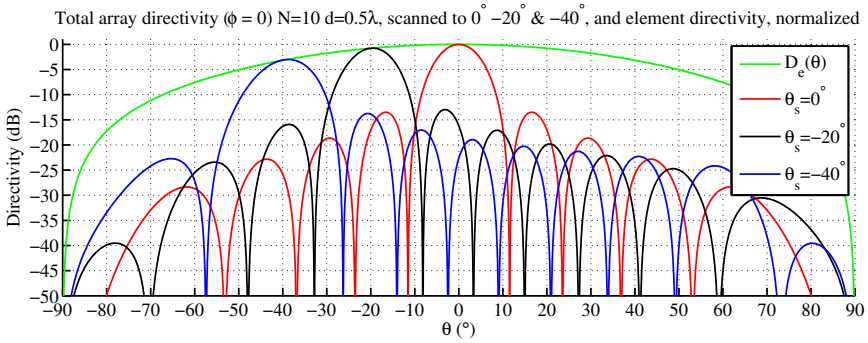

Figure 2.9: Total array directivity for N=10 and $d = 0.5\lambda$ scanned to $0°$, $-20°$ and $-40°$ with uniform amplitude excitation. The elements are horizontally aligned dipole antennas suspended above a ground plane at a distance of $\lambda/4$ with the corresponding element directivity D_e

2.2.4 Grating lobes

In Figure 2.7 it is apparent that another maxima exists in the array factor at $\pm 90^\circ$ when the inter-element spacing $d = \lambda$. Depending on the element spacing in an array, the array factor, given by Eq. (2.11), can have multiple maxima's due to the periodicity of the sine function, resulting in multiple lobes other than side lobes. These extra main lobes are often referred to as grating lobes and are generally unwanted in radar systems. Due to pattern multiplication, the grating lobe appearing at an angle where the element directivity is severely attenuated may not be visible, however when the array is scanned the grating lobe location changes and can appear within the element radiation pattern. This will, for a transmitting array cause a substantial amount of radiated energy in an unwanted direction. For a passive bistatic radar where digital beamforming techniques are utilized, the effect is just the same and is referred to as spatial aliasing. If a grating lobe appears at an angle where the DSI is nulled with beamforming, the net result would make the nulling futile.

The total array directivity of the same array as in Figure 2.9 is shown in Figure (2.10), where the element spacing has been increased to $d = 0.8\lambda$. As the array is scanned towards -40° a grating lobe appears at $\theta \approx 38^\circ$ having the same level as the main lobe at -40°.

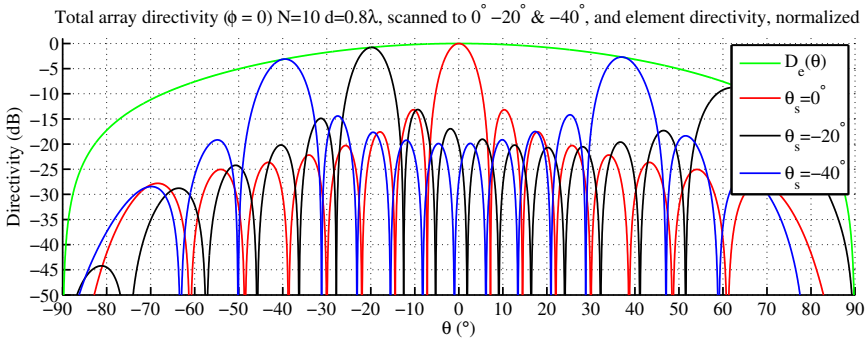

Figure 2.10: Total array directivity for N=10 horizontal dipole antennas spaced at $d = 0.8\lambda$ with uniform amplitude excitation. As the array is scanned to -40° a grating lobe appears at $\theta \approx 38^\circ$ at the same level as the main lobe at -40°

Grating lobes can be avoided in antenna arrays by choosing an inter-element spacing d according to equation (2.19), where λ is the free-space wavelength at the arrays highest operating frequency and the maximum desired scan angle is θ_s [24, p.27].

$$d \leq \frac{\lambda}{(1 + |\sin(\theta_s)|)} \tag{2.19}$$

2.2.5 Amplitude tapering

Up to this point, all the elements in the array have been excited with equal amplitude only with a phase shift in order to scan the main beam. For continuous radiation sources, the far-field radiation pattern and the excitation distribution along the source is linked through the Fourier transform [7, p.394]. An antenna array may be regarded as a discrete approximation to a continuous source, making it possible to shape the radiation pattern of antenna arrays by controlling the amplitude of the element excitation along the array.

Using amplitude coefficients a_i in Eq. (2.8) as samples of the continuous excitation distribution, an approximating to a desired radiation pattern can be obtained. A uniform amplitude excitation yields maximum directivity and a side-lobe level of approximately -13.5 dB [7, p.296], which can be too large for certain applications. Other amplitude distributions along the array can be chosen to shape the antenna array to obtain lower side-lobe levels and spatial nulling, at the cost of reducing the maximum directivity and broadening the main lobe. There exist numerous methods of beam shaping [7, ch.7], but this is not within the scope of this report. However, to illustrate the concept, a comparison of using a uniform amplitude excitation versus a -20 dB Dolph-Tschebyscheff excitation is shown in Figure (2.11) and (2.12). With a Dolph-Tschebyscheff excitation, a constant side-lobe level is obtained at the expense of decreased directivity and a greater beamwidth.

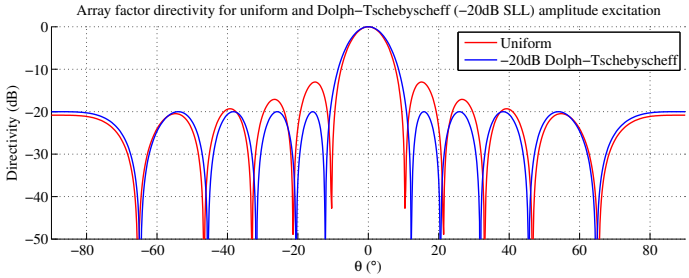

Figure 2.11: Array factor directivity for uniform and -20dB Dolph-Tschebyscheff amplitude excitation, $N = 5$ and $d = 0.5\lambda$. The Dolph-Tschebyscheff excitation shows a -20dB constant SLL

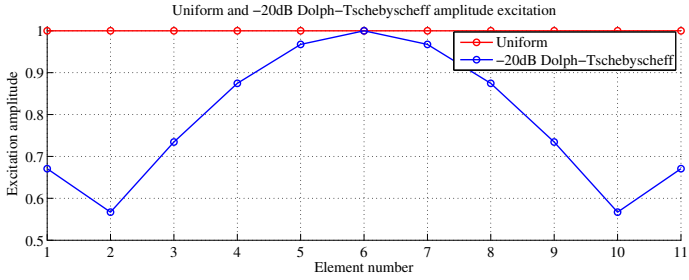

Figure 2.12: Normalized element excitation amplitude for uniform and -20dB Dolph-Tschebyscheff

2.2.6 Digital beamforming

For transmitting antenna arrays, one can steer the main lobe of the radiation pattern by exciting each antenna element with a corresponding phase for beam steering and amplitude for beam shaping using analog circuitry (variable gain amplifiers & phase shifters). For a receiving antenna array, variable gain LNA's and phase shifters can be used, or one can use digital beamforming signal processing techniques.
The term digital beam-forming is usually used when a receiver is able to form multiple beams by the means of a digital signal processor. Even though a single beam can be formed, it is usually considered when multiple simultaneous beams are sought. To be able to have multiple beams covering the system's total field-of-view, each antenna element in the array has to have a beamwidth covering this field-of-view [21, p.610].

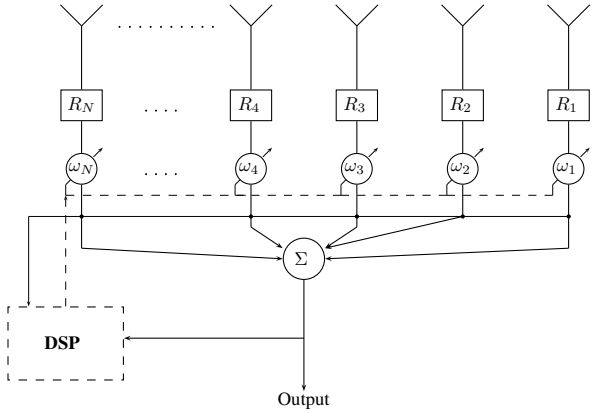

Figure 2.13: Digital beamformer where each antenna element is connected to a dedicated receiver channel which converts the signals from RF either to an intermediate (IF) frequency or to baseband before analog-to-digital conversion is done on each channel. A digital signal processor is used to multiply the samples with complex weights (ω_i) in order to do beamforming and beam steering.

In the antenna array in figure (2.13), the signals from each antenna element is band-pass filtered and down-converted to a lower frequency where it is sampled and digitized with a high performance A/D-converter. The beamforming is then done by weighting the samples from each antenna element digitally, by multiplying the samples with weighing coefficients ω_i before summation. When a linear phase weight is applied to the signals from each element, the resulting response makes the beam appear as if steered to a different angle. There is no actual change in the antenna arrays radiation pattern, however the process is equivalent to sampling signals from a given direction in space.

By downconverting the signal to a lower frequency, the A/D-converter's requirements of bandwidth and dynamic range can be eased, compared to when the RF signal being sampled directly. The process of weighing the samples from each antenna element does not degrade the signal since the SNR is established at the A/D-converter [21, p.610] compared to analog beamformers which introduce losses and degradation of the SNR.

The bistatic radar receiver in Figure 2.1 needs to have the ability to reduce the direct-signal interference (DSI) in order to detect weak targets. At the same time it needs estimate the target echo's direction-of-arrival in order to reduce the amount of ghosts and provide the target-receiver range R_r. By using digital beamforming techniques, a null can be placed in the radiation pattern in the direction of the direct-signal interference, and it is at this point that the flexibility of digital beamforming gets apparent. With N individual receiver channels one can form *N* independent beams in different directions, where each beam can have a null in the direction of the direct signal or even serve as a reference channel. Different signal processing techniques for beam-forming and estimation of DOA can be found in [7, p.961-964] as they are not within the scope of this thesis.

2.3 Mutual coupling in arrays

The analysis in the previous section was based on the assumption of having antenna elements occupying an infinitesimal volume and that there existed no interaction between the elements whatsoever. This made it possible to see the pattern multiplication property in antenna arrays, however the validity of this assumption is somewhat gross. When antennas are located to nearby objects, be it other antennas or support structures, there will be a mutual interaction and the antenna will not behave as if it were in isolation. In antenna arrays all the elements will have neighbouring elements and they all interact with each other. Depending on the magnitude of these interactions, they will cause changes in each antennas current distribution, radiated field and input impedance [7, p.468].

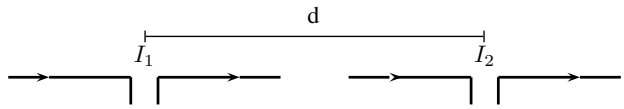

Figure 2.14: Two dipole antennas colinearly oriented

2.3.1 Mutual impedance

Figure 2.14 shows two thin dipole antennas in a collinear configuration separated by a distance d with respect to the point of excitation. The two antennas can be represented as a linear two-port network as shown in Figure 2.15 [7, p.468], where the port voltage-current relationships are given in Eq. (2.20) and (2.21).

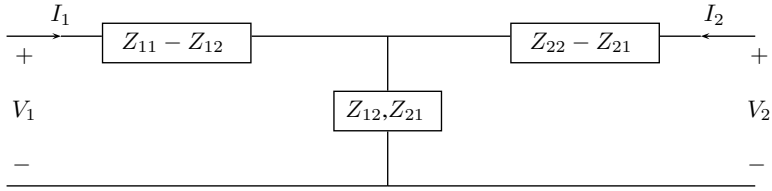

Figure 2.15: Two-port network T-equivalent from [7, p.468]

$$\begin{aligned} V_1 &= Z_{11}I_1 + Z_{12}I_2 \\ V_2 &= Z_{21}I_1 + Z_{22}I_2 \end{aligned} \tag{2.20}$$

$$Z_{11} = \left.\frac{V_1}{I_1}\right|_{I_2=0} \quad Z_{12} = \left.\frac{V_1}{I_2}\right|_{I_1=0} \quad Z_{21} = \left.\frac{V_2}{I_1}\right|_{I_2=0} \quad Z_{22} = \left.\frac{V_2}{I_2}\right|_{I_1=0} \tag{2.21}$$

Under the assumption of identical feeding configuration of the two antennas, the network becomes reciprocal ($Z_{12} = Z_{21}$). From Eq. (2.20), the terminal voltage on each antenna is not only dependent on the antennas self-impedance Z_{11}, but also the mutual impedance as well as the current (amplitude and phase) in the other antenna I_2. In the presence of another antenna element, the apparent input impedance of one antenna is modified and the extent of this effect depends on the antenna types and their relative positioning. It should here be noted that Z_{11} is the antenna self impedance when radiating into an unbounded medium (in isolation) [7, p.469]. Using Eq.(2.20) and (2.21), the driving-point impedances of the two antennas can be written as Eq.(2.22)

$$Z_{1d} = Z_{11} + Z_{12}\left(\frac{I_2}{I_1}\right) \tag{2.22}$$

$$Z_{2d} = Z_{22} + Z_{21}\left(\frac{I_1}{I_2}\right) \tag{2.23}$$

It is the driving point impedances in Eq.(2.22) to which the antennas must be impedance matched, which may be difficult as it depends on both the load connected to the other antenna, as well as the relative current ratios on the two antennas (amplitude and phase) [7, p.476]. Calculating the mutual impedance between antennas can for simple models be done using the induced emf method, otherwise more complex structures requires more comprehensive analysis such as the Integral Equation-Moment Method. For thin dipole antennas, the coupling is stronger in a side-by-side configuration compared to that in the collinear configuration in Figure 2.14 since the elements are placed along their direction of maximum radiation, whilst for the collinear configuration, the other antenna appears in null of the far-field radiation pattern, thereby reducing the mutual coupling [7, p.478].

2.3.2 Coupling in transmitting and receiving arrays

As mutual coupling is unavoidable in antenna arrays it must be taken into consideration rather than being ignored. The following qualitative analysis on mutual coupling in antenna arrays is taken from a well-written report on the subject [8]. Figure 2.16 shows different coupling paths for antennas in transmitting and receiving mode. When both antennas are either transmitting or receiving they will both receive parts of the other antennas transmitted or received energy, this continuous exchange of energy is often referred to as mutual coupling.

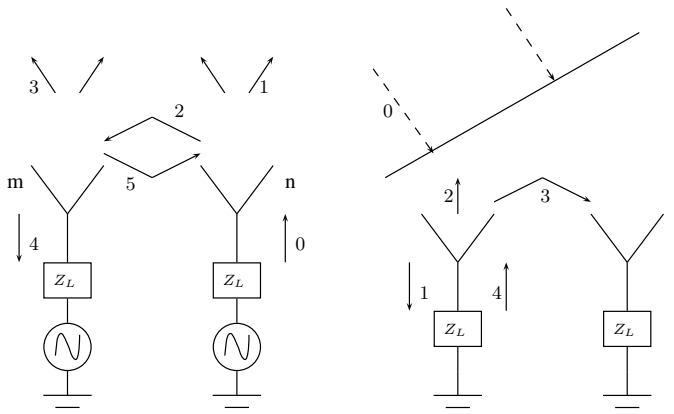

(a) Transmitting (b) Receiving

Figure 2.16: Transmitting and receiving mode coupling paths between antennas m and n, from[8]

Transmitting arrays

To illustrate the mechanisms of mutual coupling between two elements in an array. Antenna *n* in Figure 2.16(a) is excited by a generator with internal impedance Z_L (0) of which some energy is radiated into free space (1) and some is coupled to antenna *m* (2). The coupled energy causes a current to flow in antenna *m*, of which some is radiated (3) and some is launched as a wave towards the generator (4). If both antennas are transmitting simultaneously the mutually coupled energy is added vectorially to the energy from each generator, altering the apparent amplitude and phase excitation of the elements. As Allen stated [8]

> Thus, the total contribution to the far-field pattern of a particular element in the array depends not only on the excitation furnished by its own generator (the direct excitation), but also on the total parasitic excitation, which depends on the couplings from and the excitation of the other generators

The net effect of the coupling phenomena is an apparent change in antenna impedance (seen from the generator), dependent on both excitation and location of the neighbouring antenna. Matching the antenna elements to this impedance is only valid for that one set of excitation coefficients (amplitude and phase).

Receiving arrays

For the receiving array in Figure 2.16(b), the receiver at each element is represented as a passive load Z_L. A plane wave (0) is incident on the array and hit antenna *m* first, launching a wave towards the receiver (1) and re-scatters some of the energy back into free space (2), while some is coupled into antenna *n*. The coupled wave (3) adds vectorially at antenna *n* to the wave directly incident from space, resulting in a time-delay between the two contributions at antenna *n* which is dependent on the angle of incidence of the plane wave. How much the coupled energy alters the signal received at antenna *n* depends on both the time-delay and the magnitude of the coupling between the elements. In order to obtain maximum power extraction from the incident wave (0), one must choose a terminating impedance at the elements which minimizes the total energy backscattered into space. This can be done by actually mismatching the antenna to the receiver with a reflected wave (4) back to the antenna which cancel the wave that would have been rescattered if the receiver was matched to the actual antenna impedance. Furthermore, as stated by Allen, using the principle of reciprocity[8].

> The proper impedance depends on the placement and excitation of the other elements. In fact, the optimum receiver input impedance is precisely the same as the optimum generator impedance for the same array for transmitting energy in the same direction.

Effects on array performance

As mentioned earlier, the degree of mutual coupling in antenna arrays is dependent on the elements, the element spacing d, excitation and load impedance. Allen divides the effect on array performance into two classes [8], those effects which arise from the apparent variation in antenna driving point impedance and those which arise from the multipath nature of excited waves from each generator to the far field causing distorted element radiation patterns.
For a phased array antenna, the apparently changing element impedance results in variations in array radiation efficiency. If there is low mutual coupling between the elements, then the change in element impedance would be less and probably not varying too much with the element excitation. However, when there is significant mutual coupling its is almost impossible to match the antenna elements taking all possible excitations into consideration. These impedance mismatch effects distorts the receiving antennas transfer coefficients, both in amplitude an phase, and if a DOA estimation algorithm is performed on the array errors in element phase and amplitude compared to the theoretical values results in poor performance. The variations in element radiation pattern for small arrays is substantial due to the dominating edge effects, compared to large arrays where the pattern distortion is averaged away[8], making the array property of pattern multiplication a valid approximation for large arrays only.

2.3.3 Active reflection coefficient

To further emphasise the effect of having an array element input impedance which is dependent on the relative excitation of neighbouring elements, the active reflection coefficient is introduced. The derivation of the active reflection coefficient Γ_a, is taken from Pozar's review article on the subject [25].

By representing an N-element linear antenna array as an N-by-N port network, the scattering parameters of the network can be written as Eq. (2.24),

$$S_{mn} = \left.\frac{V_m^-}{V_n^+}\right|_{V_k^+=0 for k\neq n} \tag{2.24}$$

where V_m^+ and V_m^- is the incident and reflected voltage wave magnitude at the m'th element which are related by

$$V_m^- = \sum_{n=1}^{N} S_{mn} V_n^+ \tag{2.25}$$

When the array is scanned and the amplitude excitation is uniform, the port excitation at the n'th element can be written as

$$V_n^+ = V_0 e^{-jknd\sin\theta_s} \tag{2.26}$$

The active reflection coefficient at the m'th element is then found from Eq. (2.25) and Eq. (2.26) and is given by

$$\Gamma_{a_m}(\theta_s) = \frac{V_m^-}{V_m^+} = e^{jkmd\sin\theta_s} \sum_{n=1}^{N} S_{mn} e^{-jknd\sin\theta_s} \tag{2.27}$$

When there is no mutual coupling present, the active reflection coefficient is reduced to $\Gamma_{a_m} = \Gamma_m = S_{mm}$, which is just the input reflection coefficient of the m'th element, as expected. However when there is mutual coupling present, the active reflection coefficient depends on the input return loss of the antenna and the *phased* mutual impedances.

For a transmitting array, if the active reflection coefficient $\Gamma_a = 1$, then all the impinging element power is being reflected back into the source (probably a power amplifier), which can break down. When the antenna array is receiving, the effect is just the same due to the principle of reciprocity. As Allen stated, that the optimum receiver impedance is just the same as the optimum generator impedance for transmitting in the same direction. By assuming that the antenna array is being excited by a plane wave, one can assume that the amplitude excitation of each element is uniform with a relative phase shift between elements related to the plane waves direction of arrival. Due to mutual coupling between the elements, the apparent impedance changes as in the transmitting case.

2.4 CST Microwave studio

The tool used to model and simulate antennas in this thesis is CST Microwave Studio, which is a general purpose electromagnetic simulator with a powerful CAD engine. The simulator is based on the finite-integration technique, which provides a universal spatial discretization scheme. By *meshing* a structure into small cells, the method solves integral form of Maxwell's equation on the cell boundaries numerically. The transient solver in CST allows for simulation of a structure in a wide frequency range within a single run, making it an efficient simulator for antennas. For any structure in CST, one have to restrict the total computation domain with a bounding box, for antenna simulations a open boundary (perfectly matched layer) with additional spacing is used to ensure good quality on the near-to-farfield transformation.

Chapter 3

Specifications

One of the goals in this thesis is to derive the specifications for an array suitable for DVB-T based passive bistatic radar. The purpose of this chapter is to firstly provide an overview of the RF front-end of the PBR receiver followed by the derivation of antenna array specifications. The specifications include; impedance bandwidth, array size, polarization and radiation pattern, and finally a summary of design specifications.

3.1 System overview

A simplified RF front-end of a passive radar receiver is shown in Figure 3.1. With an N-channel receiver, N-1 array elements can be processed simultaneously along with the reference channel. Each channel RF front-end consists of of a channel filter, low-noise amplifier, down-converter, ADC and a digital signal processing unit where all signal processing takes place. The RF signal from each antenna element is channel limited to the whole DVB-T frequency spectrum (470 MHz - 790 MHz in Norway) through an RF filter, which must have low attenuation within the band and high roll-off factor outside to avoid out-of-band interference from other transmitters (e.g. cellular). Low-noise amplification should be performed as close to the antenna as possible in order to reduce the system's noise factor and maximize the signal-to-noise ratio in each channel. This LNA should have high gain and low noise factor. Each channel is then mixed to a an intermediate frequency (IF) with a common oscillator and is filtered and amplified to a level suitable for analog-to-digital conversion. At this point each channel is sampled coherently and the first stage in the signal processing scheme begins, the digital beamformer. Figure 3.2 shows the passive radar receiver available at FFI, developed by Fraunhofer FHR.

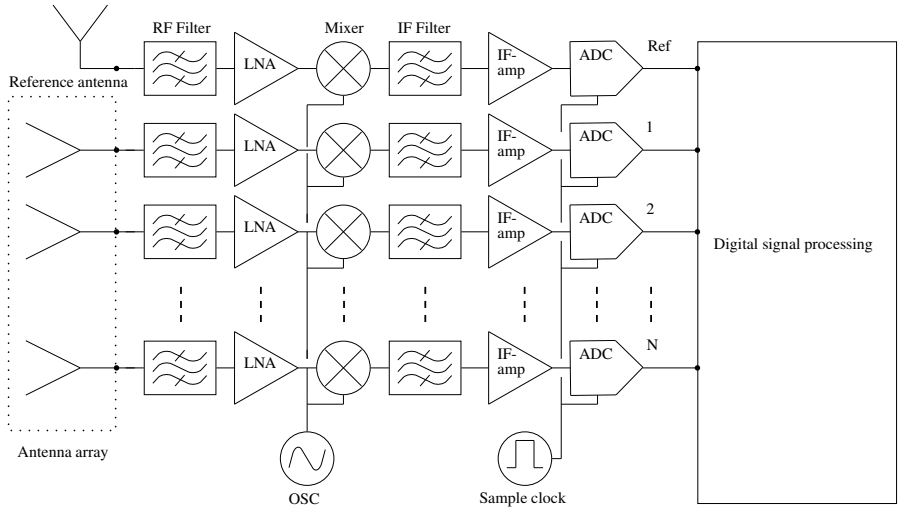

Figure 3.1: A general passive radar receiver with N surveillance channels and one reference. The received signals are converted to an intermediate frequency (IF) before sampling.

From the theory of linear antenna arrays and phased array in Section 2.2 it was assumed that, when a plane wave was impinging the array from the direction normal to the array axis (broadside), the received signals on each antenna element would have equal amplitude and phase. In reality there are multiple source of errors both in amplitude and phase in the whole signal chain, starting within the antenna array. Since the antenna array is small each antenna element have different impedance and mutual coupling to other elements which results in phase and amplitude errors in the array. Furthermore inequalities between the filters, amplifiers and mixers will also be a source of errors. Errors in channel amplitude and phase is simply added to the array factor in Eq. (2.6), where amplitude errors is added to the element excitation coefficients a_i and phase errors is added in the exponential along with the element phase shift β used to steer the beam. These errors in amplitude and phase can result in modified beam shape properties [26] and raises the need for calibration of both the receiver itself as well as the antenna array.

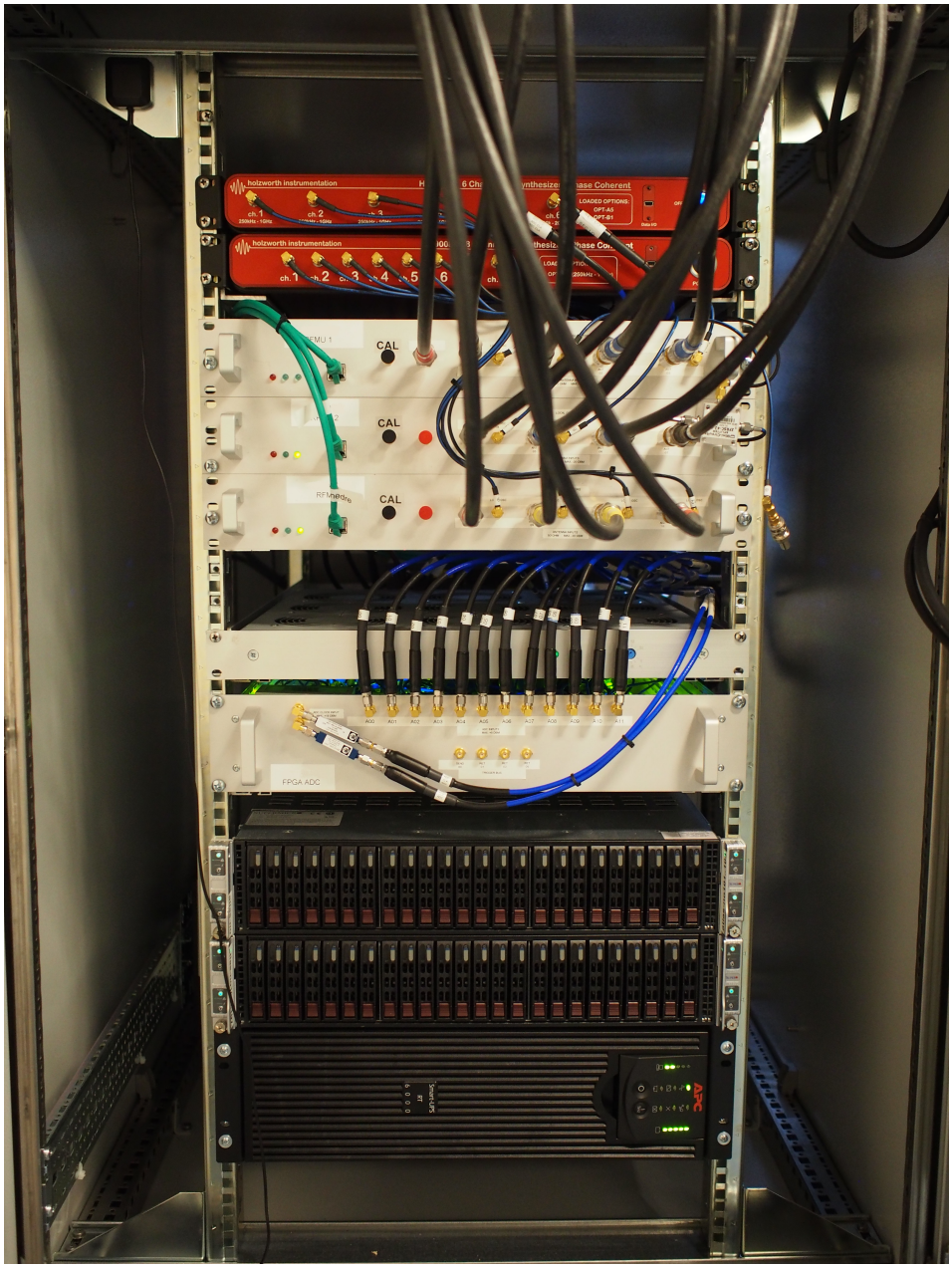

Figure 3.2: The DVB-T based passive bistatic radar receiver at FFI developed by Fraunhofer FHR. From the top: (1) phase-coherent channel references, (2) RF front-end including filtering, amplification and downconversion, (3) analog-to-digital converter, (4) computer rack and finally (5) power supply unit

3.2 Array specifications

Some passive bistatic radar systems use circular arrays with omnidirectional antennas in order to obtain $360°$ surveillance in azimuth [27],[28],[29]. The PBR system at FFI needs only sectoral coverage, thus making it possible to use antenna elements with higher gain (more narrow beam) to increase the radar performance according to the bistatic radar equation Eq.(2.4). A narrow main lobe also makes it possible to more accurately determine the direction-of-arrival (DOA) of the target echoes, providing a better estimate of the targets location.

3.2.1 Geometry and number of elements

As mentioned in section (2.2) there are no limitations on how the elements are arranged within an antenna array, however they are usually arranged in a linear, planar or circular fashion. However, since the beamforming is taking place in the horizontal plane only, a horizontal linear array provides the highest array directivity and angular resolution. With the receiver in Figure 3.2 11 channels are available for surveillance, making it possible to form 11 simultaneous beams within the $90°$ horizontal sector. The whole can be covered by scanning the beams to $0°$ $\pm 9°$ $\pm 18°$ $\pm 27°$ $\pm 36°$ & $\pm 45°$. This is illustrated in Figure 3.3, where the phased array directivity scanned to the respective angles is plotted for a linear array of 11 horizontal dipole antennas separated with a distance $d = 0.5\lambda$ using uniform amplitude weighing. The half power beamwidth at broadside is approximately $10°$ and as the array is scanned, the beamwidth increases and directivity decreases as a direct consequence of the array factor and the attenuation in the dipole radiation pattern.

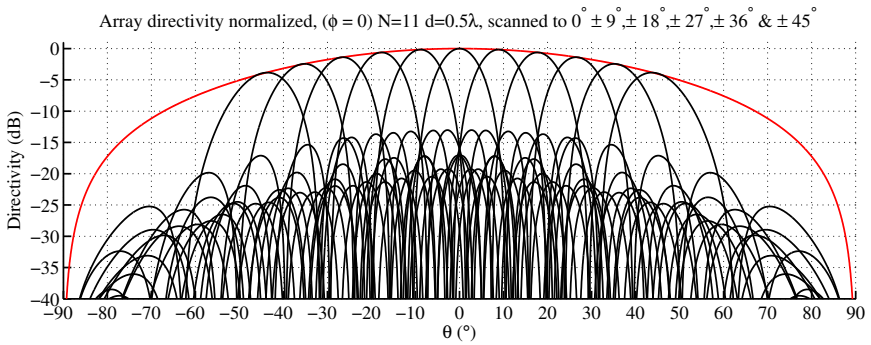

Figure 3.3: A $d = 0.5\lambda$ $N = 11$ uniform amplitude, static beams, target DOA based on best SNR from each beam, element factor is a half-wavelength dipole antenna

The vertical plane surveillance sector should be at least $45°$, however there is no point in making the sector any wider, since the radar is mainly supposed to detect low-flying targets. Furthermore there is a limitation related to the target illumination from the DVB-T transmitters, which tends to focus most of its transmitted energy towards the ground where coverage is needed. By keeping this sector as narrow as possible results in maximum antenna gain and radar range.
If the HPBW of the antenna elements exceeds $45°$ in the vertical plane then multiple rows of elements can be stacked vertically. With two rows of elements, where each column is connected to a -3dB power splitter (in phase) the vertical plane beamwidth is halved and the array gain is doubled due to the doubled array aperture. This however, doubles the cost of the array. Figure 3.4 shows the normalized array factor (in elevation) for 2 and 3 elements stacked vertically, resulting in a half-power beamwidth of $60.7°$ and $36.4°$ respectfully. It is clear that the required beamwidth in elevation is too narrow using 3 rows stacked vertically, while using 2 rows result in a beamwidth slightly larger than required.

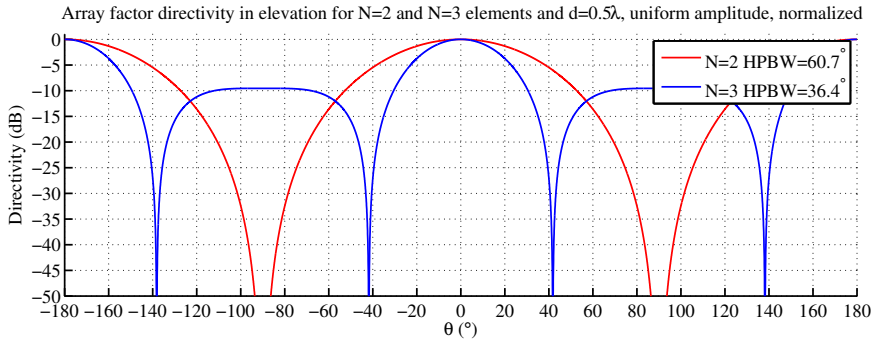

Figure 3.4: Elevation plane array factor directivity for N = 2 and N = 3 elements excited in-phase

Whether the array should be designed for one or two rows of elements stacked vertically only needs to be considered if the beamwidth of the antenna elements used in the array exceeds the desired beamwidth in elevation significantly. From a cost perspective, doubling of the number of elements more than doubles the cost of the array when power-splitters are taken into account. Based on this and the increased computational complexity in simulations, the array will be designed with only one row, and the stacking of elements to increase the gain is left for future work.

3.2.2 Frequency range and impedance bandwidth

The passive bistatic radar receiver is planned on being deployed in the Oslo-fjord area to do bistatic and multistatic measurements. Information on available transmitters broadcasting DVB-T signals in this area and their channel frequencies is available from Norkring [30], and a summary of the different transmitters is given in table (2.1). The antenna array should fulfil the specifications within two, preferably three different channel frequencies in each single-frequency network in this area. Based on the limited number of useful deployment sites (geographical peaks) and the information available from Norkring, three different bandwidth requirements were formed,where the antenna element should be suitable for the application within at least one of these frequency bands.

1. 622 MHz - 726 MHz CH. 40-52 (15.4% relative. BW)
2. 622 MHz - 750 MHz CH. 40-55(18.6% relative. BW)
3. 574 MHz - 750 MHz CH. 34-55(26.5% relative. BW)

An antenna acts as a transducer between the characteristic impedance of an RF system and the impedance of free space. It is desirable to maximize the power transfer from the incoming plane waves to the receiver, thus requiring the impedances of the antenna and the receiver must be matched. The bistatic receiver in figure (3.1) has a characteristic impedance of 50Ω to which the impedance of the antenna must be matched. The input reflection coefficient is given by Eq. (3.1)

$$S_{11} = \Gamma = \frac{Z_A - Z_0}{Z_A + Z_0} \tag{3.1}$$

Where Z_A is the antennas input impedance and Z_0 is the systems characteristic impedance (50Ω). The input reflection coefficient gives information on how much of the power delivered to the antenna is reflected at its port, and with perfect impedance matching no power will be reflected. A commonly used impedance matching level is $|S_{11}| \leq -10dB$, where the impedance bandwidth is the frequency range in which the reflection coefficient is below this level.

3.2.3 Array element polarization

Most of the DVB-T transmitters in the Oslo fjord area are horizontally polarized, based on measurements conducted at FFI using a linearly polarized antenna and a spectrum analyzer. The received signal power was approximately 15dB stronger when the antenna was horizontally oriented compared to vertically. However, there is no information available from Norkring on whether the polarization of every transmitter in Norway is the same.
Choosing polarization on the receiving antenna array, could possibly be motivated by the assumption that the reflected waves from targets primarily have the same polarization as the transmitter illuminating it. The IEEE definition of *monostatic* radar cross section (RCS) can be expressed as Eq.(3.2)[31, p.220], where R is the trasmitter/receiver-target range, $\mathbf{E_{inc}}$ is the E-field impinging on the target and $\mathbf{E_{scat}}$ is the scattered E-field. The scattered field depends on target geometry and material composition, the position of the transmitter and receiver relative to the target, the frequency and the polarization for the transmitter and/or receiver. The reflected signal may well contain major cross-polar components [31, p.221].

$$\sigma = \lim_{R \to \infty} 4\pi R^2 \frac{|\mathbf{E_{scat}}|^2}{|\mathbf{E_{inc}}|^2} \tag{3.2}$$

From a passive radar point of view, where the direct-signal interference is one of the major limitations for target detection, one can utilize cross-polarized antenna elements in the surveillance channel to reduce the direct-signal interference. Ideally, if the polarization of the receiving and transmitting antennas are orthogonal, there would be no power extracted by the receiving antenna due to polarization losses [7, p.78]. In reality this is not the case, as polarization purity is limited in real antennas. The co-polar components of the scattered E-field will also be attenuated with the same level as the direct signal, but if the target echoes contain a useful magnitude of cross-polar components, then target detection may still be obtainable. If the antenna elements would have dual polarization it would allow reducing the direct signal interference and at the same time opens the possibility to use both polarizations for target recognition [21, p.383]. Furthermore it allows for greater flexibility in sensor deployment sites where the transmitters of opportunity have either vertical or horizontal polarization.

Due to uncertainties regarding the polarization of the receiving antenna array, a short measurement survey on whether dual polarized antennas could be used to detect targets was conducted at FFI in the spring of 2014, using the receiver in Figure 3.2 and a set of three wideband log-periodic dipole antennas. The reference antenna (one of the log-periodic's) was horizontally polarized, the same as the direct-signal from the transmitter being exploited in order to obtain a good reference channel. Two surveillance channels were used, where one of the antennas were horizontal polarized and the other vertically. Cross-correlation between the reference channel and each of the surveillance antennas produced the bistatic range-doppler maps in Figure 3.5 and 3.6.

In Figure 3.6, where both surveillance and reference antennas were horizontally polarized there are two targets visible (marked with red circles) at (16 Km, -376 Hz) and (0.71 Km, -140 Hz), target 1 and target 2 respectively. Target 1 had a SNR of 18.98dB compared to 14.72dB for target 2. The range-doppler map from the vertically polarized surveillance antenna is shown in Figure 3.6. Target 1 had a SNR of 11.98 dB, a reduction of 7dB compared to the results obtained using a horizontally polarized surveillance antenna. Target 2 however, shows a SNR of 20.06dB, an *increase* of 5.34dB when a vertically polarized surveillance antenna was used. It should be noted that these results were obtained without any channel compensation or adaptive filtering to reduce the DSI, the data presented are raw-data bistatic range-doppler maps. These results shows that different targets have different SNR for the two orthogonal polarizations. Looking closer at the zero-doppler line, there is a great attenuation of the direct signal when the surveillance antenna is vertically polarized. At approximately 11 Km bistatic range, there is another transmitter visible which is greatly attenuated for the vertical-horizontal case.
These results may suggest that it might be beneficial to have dual polarized antenna elements, which increases the flexibility of the system is to be tested in places where the transmitters use vertical polarization. Furthermore it allows for the possibility of using switches to change the polarization of the receiving antenna. This motivates that the receiving antenna element should have dual polarization, both horizontal and vertical.

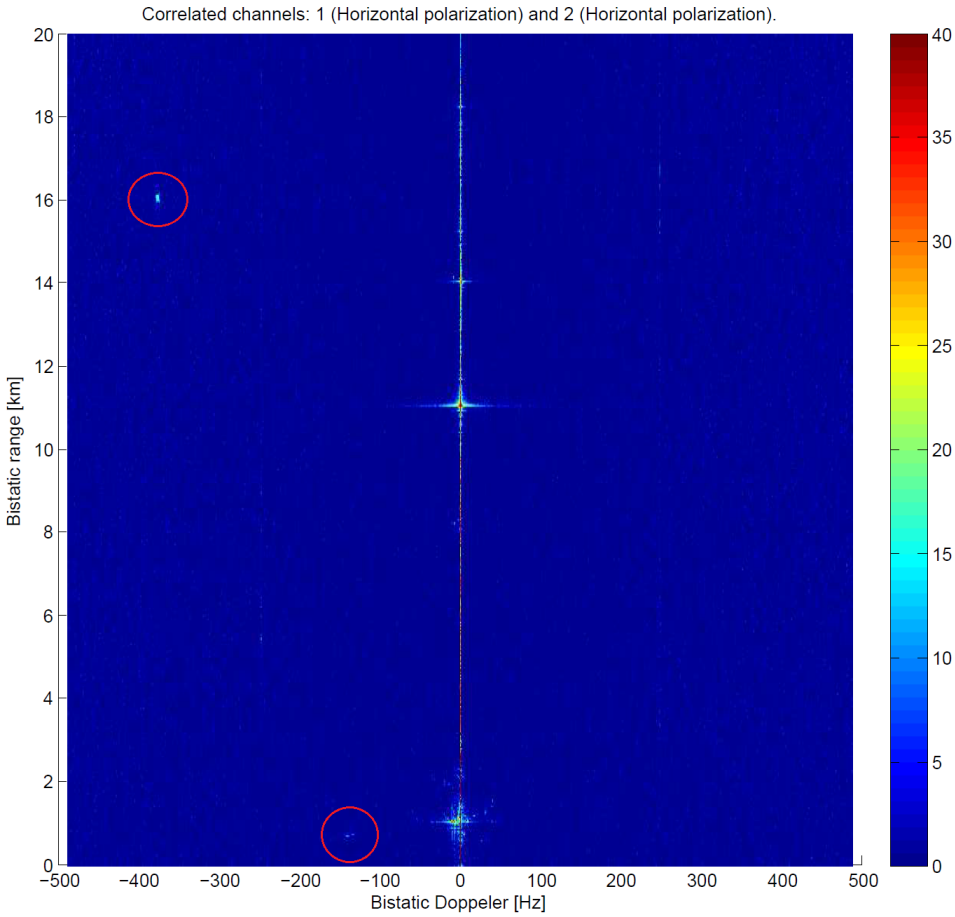

Figure 3.5: Bistatic Range-Doppler with horizontally polarized surveillance and reference antenna. Two targets (in red circles) appears at (16 Km,-376 Hz) and (0.71 Km,-140 Hz) with a measured SNR of 18.98 dB (target 1) and 14.72 dB (target 2) respectively. Another transmitter in the single-frequency network is visible at approximately (11 Km, 0Hz), Figure courtesy of FFI

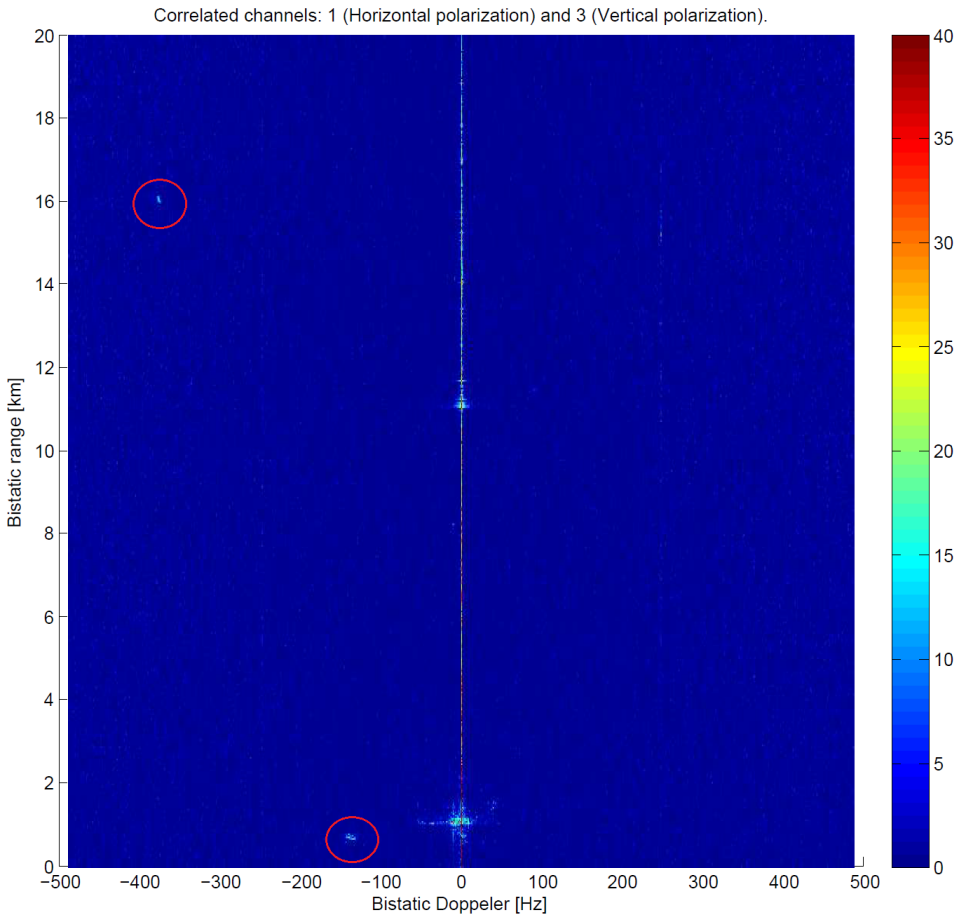

Figure 3.6: Bistatic Range-Doppler with horizontally polarized reference antenna and vertically polarized surveillance antenna. Two targets (in red circles) appears at (16 Km,-376 Hz) and (0.71 Km,-140 Hz) with a measured SNR of 11.98 dB (target 1) and 20.06 dB (target 2) respectively. Another transmitter in the single-frequency network is visible at approximately (11 Km, 0Hz), however severely attenuated compared to that in Figure 3.5, Figure courtesy of FFI

3.2.4 Array element radiation pattern

The required sectoral coverage of the system is $\geq 90°$ in azimuth and $\geq 45°$ in elevation and target position in azimuth is found using digital beamforming in this plane. From section (2.2.6), the required half-power beamwidth of the antenna in the two principal planes must cover at least the required field-of-view. For a horizontally polarized antenna, the E-plane lies in the horizontal plane whilst the H-plane is in the vertical plane. For a vertically polarized antenna it is just the opposite. Figure 3.7 shows the desired radiation pattern in the two principal planes for a horizontally polarized antenna with half-power beamwidth of $90°$ azimuth and $45°$ elevation.

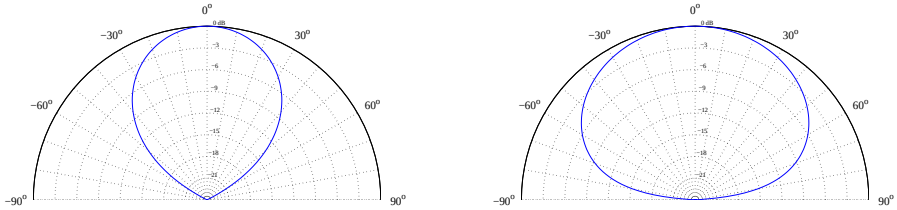

(a) Optimal H-plane pattern (elevation), HPBW $45°$ (b) Optimal E-plane pattern (azimuth), HPBW $90°$

Figure 3.7: Optimal H- and E-plane radiation patterns for the horizontally polarized antenna elements, the E- and H-plane patterns are switched for vertical polarization

3.2.5 Element spacing and element form factor

From Section (2.2), there is a limitation on how large the spacing between elements in a phased array can be before grating lobes starts to appear. This spacing d, between the feed-points of two neighbouring elements, is a function of the wavelength at the arrays maximum operating frequency λ_H and the required scan range away from broadside θ_s, and is given by Eq. 2.19. The three bandwidth requirements dictates different requirements for maximum element spacing, with $\lambda_h = 726$ MHz or $\lambda_h = 750$ MHz. Table (3.1) below shows some of the values of d for the two maximum operating frequencies and different scan angles.

Table 3.1: Inter-element spacing d for different scan range requirements and maximum operating frequencies

f_H(MHz)	θ_s	d(mm)	f_H(MHz)	θ_s	d(mm)
750	90°	200	726	90°	206
	60°	214		60°	221
	55°	220		55°	227
	50°	226		50°	233

As the required surveillance sector in azimuth is $90°$, there should not be any grating lobes appearing when the array is scanned to $\pm 45°$. If any grating lobes is to appear close to this limit, say $\pm 60°$, then the effect can only be ignored *if* the roll-off in the element radiation pattern is high enough attenuating the grating lobes to insignificant levels. When the array is designed, a trade-off between grating lobe-free scan range and mutual coupling is unavoidable. Furthermore the maximum inter-element distance also limits the size of the element itself when arranged in a horizontal linear array.

3.3 Design specifications summary

A summary of the specifications is given below

- Array geometry: horizontal linear array
- Number of elements: 11
- Frequency band 1: 622 - 726 MHz
- Frequency band 2: 622 - 750 MHz
- Frequency band 3: 574 - 750 MHz
- Impedance matching level: $|S_{11}| < -10dB$
- Polarization: Horizontal and vertical
- HPBW E-plane (azimuth): $90°$
- HPBW H-plane (elevation): $45°$
- Element spacing: $200mm \leq d \leq 233mm$

Chapter 4

Design and analysis

4.1 Design methodology

The design of the antenna array for the DVB-T based passive bistatic radar is based on the specifications derived in the previous chapter. In a wilderness of different antenna elements which can be suitable for the application, only elements used in commercially available PBR systems and those reported in literature on the subject are considered as possible candidates due to limited available time. The simulation tool used in the design process is CST Microwave Studio which is a general purpose electromagnetic simulator. By making the CAD model in CST parametrized in terms of geometrical parameters, one can perform parameter sweep and optimization routines until acceptable performance is obtained. The use of a simulation tool such as this also motivates prototyping of the simulated array to verify the results obtained from simulations.

The specifications in the previous section dictates the need of an 11 element antenna array, which can be challenging to conduct measurements on solely based on the sheer size of the array in the frequency range of interest. Assuming an inter-element spacing of $d = \lambda/2$ at 674 MHz with 11 elements in a horizontal linear array, the length of the array would be approximately 2.5 metres. As the anechoic chamber at NTNU has its limitations on array size, only a partial array can be measured. With a 5 element array, the center element is surrounded by two neighbouring elements on each side and its performance in terms of impedance bandwidth and radiation pattern should be comparable to the center elements in the full array. If the results from the prototype are within acceptable limits, a full array can be constructed.

4.2 Antenna elements used in PBR arrays

Figure 1.4 shows four commercially available passive radar systems from Selex, ERA, Lockheed Martin and Thales, where the two latter systems use thin vertically oriented cylindrical half-wave dipole antennas arranged in a circular array. These elements have also been reported in [28], [29], but only for FM-based passive radar. Simple dipole antennas like this have narrow impedance bandwidth, typical 3% [7, p.509], which may be a useful element if a single DVB-T channel is found suitable, however not with the bandwidth requirements given in the previous section. The antenna array used in ERA's Silent Guard is shown in Figure 4.1, consisting of 6 horizontally oriented biconical wire antennas in a circular array. Each element is suspended in front of a ground plane with reflector planes at each side, resulting in unidirectional element radiation pattern. Being a broadband dipole antenna it could be suitable for the DVB-T based PBR array, and by crossing two biconical antennas one can obtain dual polarization which is desired, all-in-all making this element a possibly suitable candidate. The array used in Selex's Aulos system in Figure 1.4(a), consists of eight broadband monopole ground plane antennas arranged in a circular array. This element is vertically polarized with an omnidirectional radiation pattern in azimuth. Since it is not possible to obtain dual polarization with this antenna, it is found not suitable for the array in question.

Figure 4.1: Silent Guard antenna array, photo: ERA

The Fraunhofer Institute for High Frequency Physics and Radar Techniques (FHR) has developed a wideband antenna array for DVB-T based passive bistatic radar [27] with a disc-cone antenna covering the entire DVB-T frequency band. This element is omnidirectional in azimuth with antenna pattern much like that of the dipole antenna [32, p. 249] with wideband impedance bandwidth. It is comparable to the ground-plane antenna used in Selex's Aulos, however with the disc-cone the monopole is replaced with a circular disk. This element shows promising characteristics in terms of impedance bandwidth, however it is not found suitable as a dual polarized solution.

Figure 4.2: The disc-cone antenna array developed at Fraunhofer FHR, photo: Fraunhofer FHR

Figure 4.3 shows the antenna array in the CORA system (*Co*vert *Ra*dar) developed by FGAN FHR (now Fraunhofer FHR). This system was the first passive covert radar to demonstrate air and maritime target detection exploiting both DAB and DVB-T transmitters of opportunity [10]. The array is made out of elements covering 150-350 MHz (bottom part) and 400-700 MHz(upper part), using different dipole antennas. Broadband wide flat dipole antennas are located in the upper right on the array along with crossed cylindrical dipoles to the left. The bottom array consists of 16 crossed wire bowtie antennas obtaining both horizontal and vertical polarization, as with the crossed cylindrical dipoles.

Figure 4.3: Cora demonstration radar antenna, photo: Fraunhofer FHR

From the investigated antenna arrays, the one array which shows good promise in terms of bandwidth is the lower elements of the Cora radar with crossed wire bowtie antennas. This antenna is a geometrical approximation of the biconical antenna used in the Aulos array, inheriting some of its broadband performance. Being a flat antenna makes production simpler and cheaper. With the crossed bowtie antenna dual polarization can be obtained as well as higher impedance bandwidth than the crossed cylindrical dipoles.

4.3 Bowtie Antenna

The bowtie antenna shown in Figure 4.4(a) is a geometrical approximation of the broadband biconical dipole antenna, consisting of two flat triangles of length L_{arm} with a flare angle α. Being a flat antenna makes it possible to be etched or milled out on a piece of PCB or sheet metal, reducing production costs at the expense of reduced bandwidth. By crossing the two arms of the bowtie one can obtain dual polarization as that in the CORA demonstration radar in Figure 4.3.
A wideband bowtie antenna designed by Bailey [33] was suggested as an element in a wideband phased array antenna. The bowtie length was 0.3λ with a flare angle of $60°$, suspended above a ground plane at a height $3/8\lambda$ resulting in a VSWR$\leq$ 2 between 500 and 700 MHz. Due to the large height above the ground plane, the radiation pattern had a degradation at zenith for higher frequencies, which is as expected from theory [32, p.224]. Based on this, the bowtie antenna serves as a possibly suitable candidate for the PBR antenna array in question.

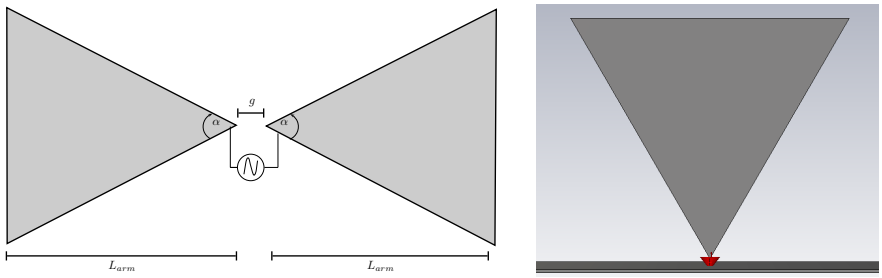

(a) (b)

Figure 4.4: a) Bowtie antenna, consisting of two triangles of length L_{arm} and flare angle α and a feed gap g b) Unipole antenna mounted on a ground plane, as described in [9]

4.3.1 Simulation tool verification

A comprehensive experimental study on the triangular unipole Figure 4.4(b) was conducted by Woodward & Brown [9] in 1945, where both impedance and radiation characteristics of the antenna was investigated with respect to the antenna length and flare angle. These results are equally valid for dipoles, however the impedance values must be doubled [9] when applied for dipole design. In order to evaluate the simulation software CST Microwave Studio, a triangular unipole antenna like that in the experiments of Woodward & Brown was modelled and simulated. The length of the antenna L_{arm} is expressed as the *electrical* length (in degrees) referenced to a design center frequency, here at $f_0 = 674$ MHz. The input resistance and reactance of the unipole was then evaluated at this frequency, as in [9]. Figure 4.4(b) shows the unipole as modelled in CST Microwave Studio, with a ground plane of size $2\lambda_0$ by $2\lambda_0$. The unipole is fed by a discrete face port with a generator impedance of 50Ω.

Figure 4.5 and 4.6 shows both the results from the experiments of Woodward & Brown and the results obtained from the simulations in CST Microwave Studio. The results are in good agreement with those reported in [9], which could imply that the simulation software delivers results of high quality. It should be noted that Figure 4.5(a) and 4.6(a) also contains a plot of $\alpha = 5°$, which was omitted from the simulations in CST. As pointed out in [9], the fluctuations in resistance and reactance is lower for larger flare angle α, yielding higher bandwidth.

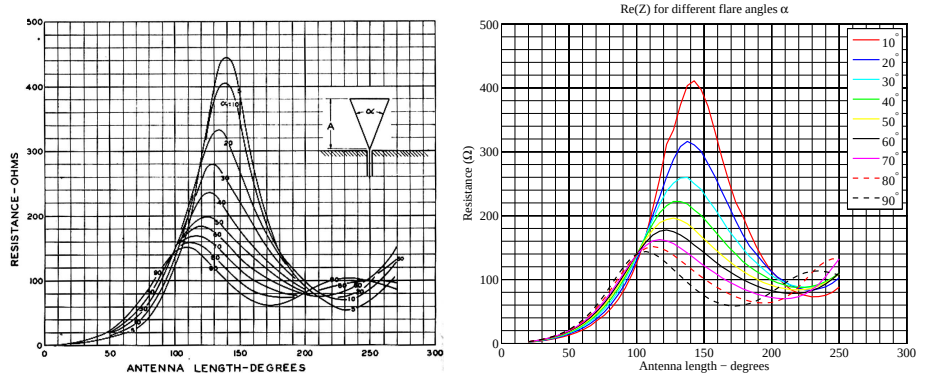

(a) (b)

Figure 4.5: a) Measured resistance from [9], b) simulated resistance for different antenna lengths and flare angles of the unipole antenna

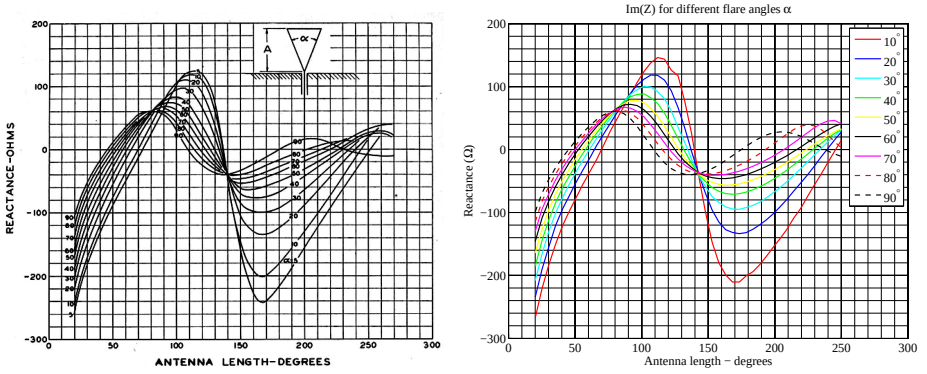

(a) (b)

Figure 4.6: a) Measured reactance from [9], b) simulated reactance for different antenna lengths and flare angles of the unipole antenna

4.3.2 Bowtie suspended above a ground plane

Background

In the passive bistatic radar with sectoral coverage, the antenna needs to have a unidirectional radiation pattern, and to obtain this with a dipole antenna one can suspend it above a conducting ground plane as shown in Figure 4.7. The horizontally aligned dipole antenna suspended at a height h above a ground plane is a popular element in phased array, as it more than doubles the gain by limiting the radiation pattern in one direction [32, pp. 223-225]. Both radiation pattern and input impedance changes with the height h above the ground plane, but this height is usually kept between $\lambda/4$ and $3\lambda/8$ to obtain a unidirectional radiation pattern [24, p.234]. As the height is lowered towards zero the input impedance approaches zero due to the dipoles interactions with its odd-mode image [32, p.224], and above $3\lambda/8$ the gain at zenith decreases and the radiation pattern eventually becomes multi lobed as the height is increased [24, p.234], this is shown in Figure 4.8.

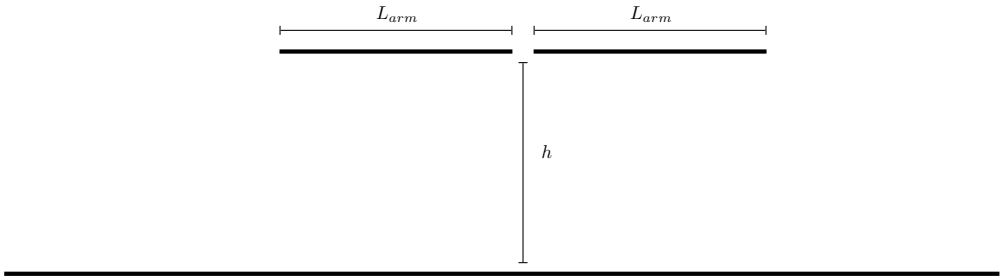

Figure 4.7: A dipole antenna consisting of two arms of length L_{arm} suspended above a ground plane at a height h, as viewed from the side

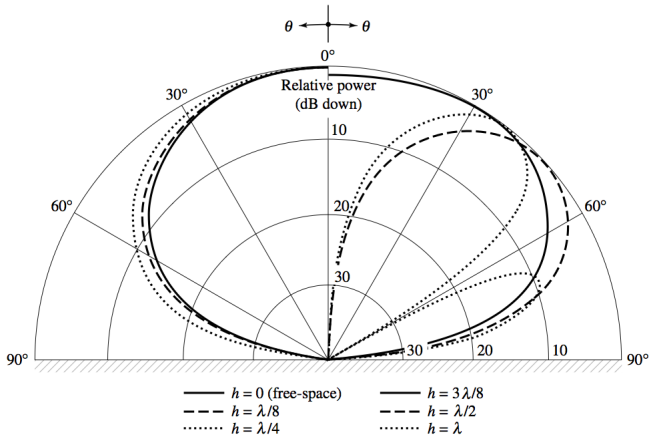

Figure 4.8: Horizontal plane amplitude patterns of a horizontal infinitesimal electric dipole for different heights above an infinite ground plane[7, p.201]

Design

For simplicity the antenna was designed for the smallest bandwidth requirement (622-726 MHz) with a center frequency of 674 MHz ($\lambda \approx 445$mm). By using the design curves from Woodward & Brown and keeping in mind to double the values for dipole design, the length of the element should be $45° < L_{arm} < 70°$ depending on the flare angle, to match the antenna to a characteristic impedance of $Z_0 = 50\Omega$. To obtain design curves for a bowtie antenna suspended above a ground plane at a height $\lambda/4$, the antenna was modelled and simulated in CST. The ground plane measured 2λ-by-2λ and the bowtie was excited using a discrete face port with internal generator impedance of 50Ω. By conducting the same parameter sweep of antenna arm length and flare angle as in the experiments of Woodward & Brown, new impedance design curves were obtained and is shown in Figure 4.9.

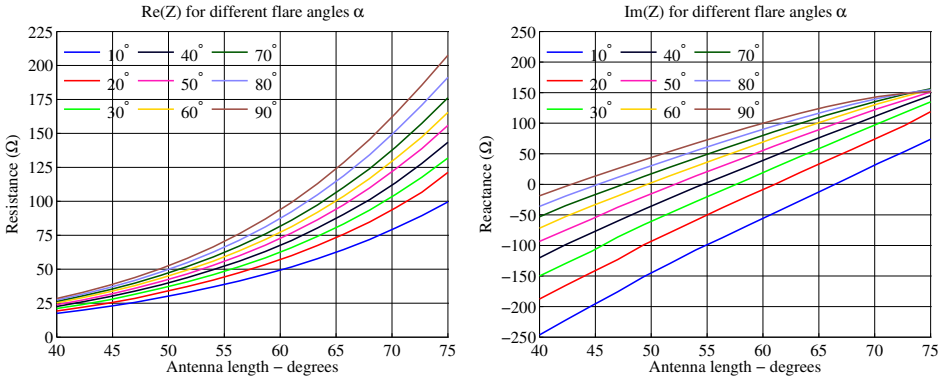

(a) (b)

Figure 4.9: Resistance and reactance design curves for a bowtie suspended above a ground plane at a height $h = 90°$ (quarter wavelength) for different flare angles α and dipole arm length L_{arm}.

Using the design curves in Figure 4.9 the length of the antenna should be $45° \leq L_{arm} \leq 60°$ depending on the flare angle, to match the antenna to $Z_0 = 50\Omega$. It can be seen that for a fixed antenna length, the resonance frequency is decreased as flare angle increases. This is as expected as the current is more concentrated along the edges of the bowtie antenna and when the flare angle increases, the outer path length increases, resulting in a lower resonance frequency. It can also be seen from the reactance plots that as the flare angle increases, the slope of the reactance decreases, resulting in more broadband characteristics, like with the biconical dipole antenna [7, p.505].
Choosing the flare angle $\alpha = 60°$ as in [33], the length of the dipole arms L_{arm} and height above the ground plane h were adjusted until the required impedance bandwidth was fulfilled. The resulting antenna parameters were; $L_{arm} = 50°$, $\alpha = 60°$, $h = 105°$ with an antenna thickness of $t = 1mm$.

Results

Figure 4.10 shows the simulated input reflection coefficient S_{11}, which is below the -10 dB limit from approximately 614 MHz to 739 MHz, fulfilling the lowest bandwidth requirement of 622-726 MHz. The corresponding input impedance of the antenna is shown in Figure 4.11, where the resonance frequency (Im(Z)=0) is approximately 660 MHz.

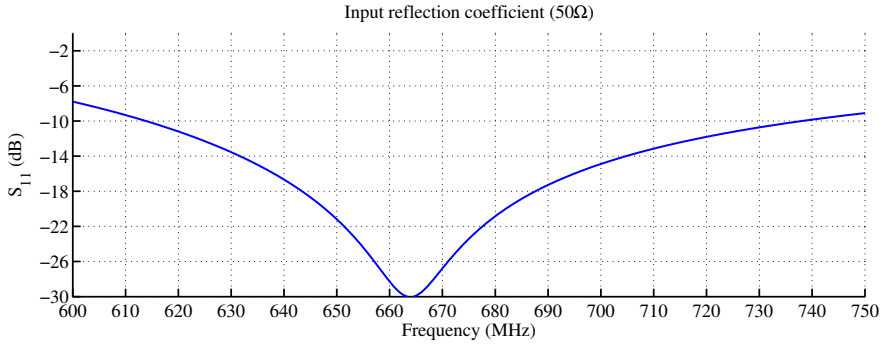

Figure 4.10: Simulated input reflection coefficient, magnitude plotted in dB for the bowtie antenna. The -10 dB bandwidth of the antenna is 125 MHz from 614 to 739 MHz

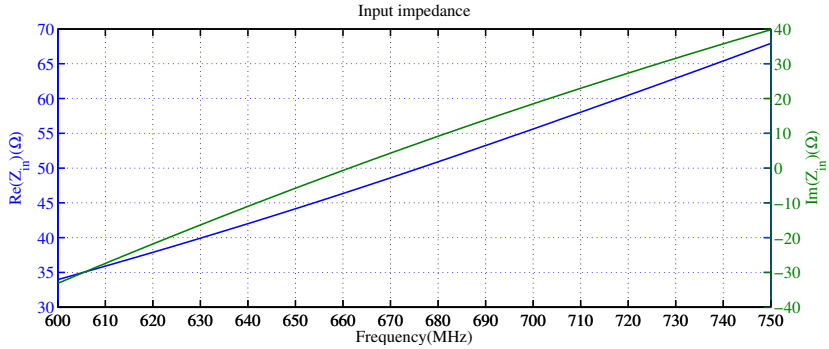

Figure 4.11: Simulated input impedance of the bowtie antenna, showing both input resistance and reactance in Ω

The resulting E- and H-plane directivity patterns are shown in Figure 4.12 and 4.13 for 622 MHz, 674 MHz and 726 MHz. Frequencies corresponding to edges and center in the lowest bandwidth requirement. The half-power beamwidth is approximately $87°$ in the E-plane which is close to the required $90°$, and the H-plane HPBW is approximately $122°$ which is more than twice of the required $45°$. In both of the radiation patterns there is a slight degradation at zenith ($\theta = 0°$ which gets larger as the frequency increases. This is as expected from theory [32, pp. 223-225], since the height h above the ground plane is slightly above $\lambda/4$ at 674 MHz. The maximum directivity at zenith decreases and the degradation at zenith is worst at 726 MHz and is approximately 1 dB below the maximum directivity of $D_0 = 6.2$ dB.

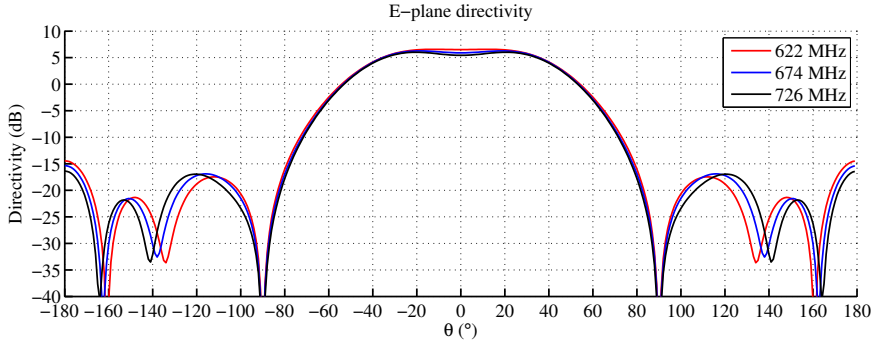

Figure 4.12: E-plane directivity at 622, 674 and 726 MHz showing a maximum directivity of $D_0 = 6.2$dB with half-power beamwidth of approximately $87°$

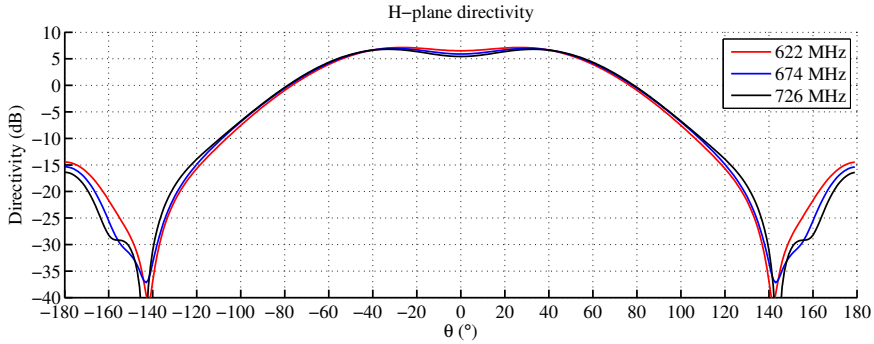

Figure 4.13: H-plane radiation pattern at 622, 674 and 726 MHz showing a maximum directivity of $D_0 = 6.2$dB with half-power beamwidth of approximately $122°$

4.3.3 Crossed Bowtie Antenna

By crossing two bowtie antennas dual polarization is obtained, where one port corresponds to horizontal polarization and the other to vertical polarization if the elements are aligned correspondingly. Figure 4.14 shows the crossed bowtie antenna suspended above a ground plane (viewed from above) as modelled in CST, by duplicating the bowtie from the last section and rotating one of the bowties $90°$. The antenna is excited with two discrete face ports (one for each polarization) with generator impedance 50Ω and when one of the bowties is simulated, the other one is terminated with its own generator impedance. In order to obtain the same impedance bandwidth as the single dipole, the bowtie arm lengths had to be adjusted $50°$ to $52.5°$ using the same flare angle $\alpha = 60°$. Again, the materials used for the dipole arms was perfect electric conductor (PEC).

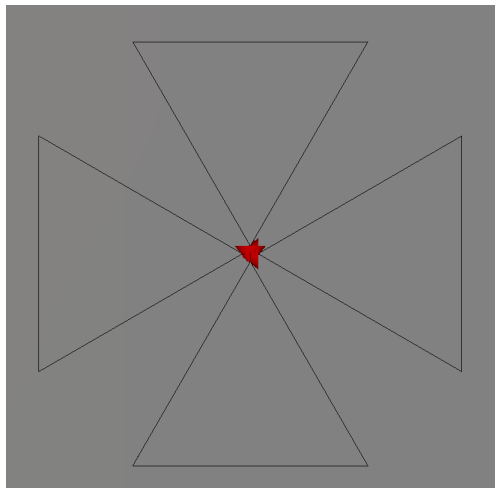

Figure 4.14: The crossed bowtie antenna as modelled in CST. Each dipole is connected to a 50Ω discrete face port in a feed gap of 5mm. $L_{arm} = 53°$, $\alpha = 60°$

The simulated input reflection coefficient of the two ports is shown in Figure 4.15,where both curves are approximately equal which is expected as the two dipoles are identical. The reflection coefficient is below the -10 dB level between 615 and 750 MHz, fulfilling the second bandwidth requirement of 622-750 MHz. This is a slight increase in bandwidth compared to the single bowtie dipole, which has also been reported in [34].

Figure 4.16 shows the simulated mutual coupling between the horizontal and vertical bowtie, where extremely low coupling (i.e. high isolation) below -50dB was obtained. In [34] it is pointed out that there is a high amount of mutual coupling between the bowtie antennas and that it is the *parasitic* excitation of one element which alters the impedance of the other. The coupled current have a distribution which is strictly symmetrical with respect to the bowtie center, giving no potential difference between the two feed points and resulting in a situation where no induced current can flow into the port giving high isolation. In order to obtain such an isolation between the elements, the ports must be absolutely isolated and symmetrical, which might not be possible to realize in a prototype.

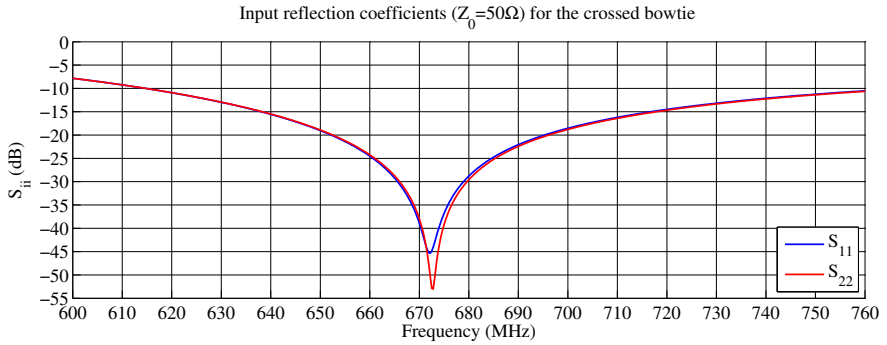

Figure 4.15: Simulated input reflection coefficient for the crossed bowtie antenna. $S_{11} \approx S_{22}$ as expected since the two dipoles are identical. The impedance bandwidth (-10dB) is 135 MHz from 615-750 MHz with resonance frequency at approximately 674 MHz

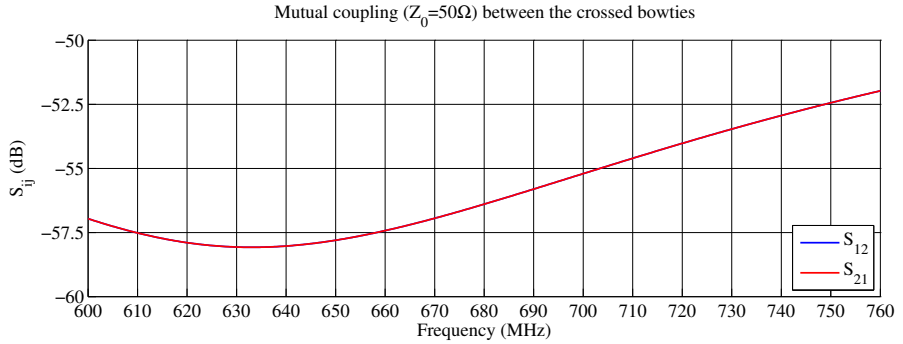

Figure 4.16: Simulated mutual coupling (isolation) between the two ports of the crossed bowtie antenna. $S_{12} = S_{21}$ as expected, since the two-port network is reciprocal. Good isolation of < -50 dB is obtained in the whole bandwidth

Radiation pattern

The simulated E-plane co- and cross-polarization directivity for both the horizontal and vertical polarized bowtie is shown in Figure 4.17 & 4.18 for 622, 674 and 726 MHz. The half-power beamwidth in the E-plane (co-pol) is approximately $87°$, and the E-plane directivity is equal for both horizontal and vertical polarization as expected, since the elements are equal. This is also true for the simulated H-plane co- and cross-polarization directivity in Figure 4.19 and 4.20, where the H-plane (co-pol) shows a HPBW of approximately $122°$. The maximum directivity is again $D_0 \approx 6.2$ dB, whilst the maximum cross-polar directivity is ≈ -47dB in both planes for both polarizations.

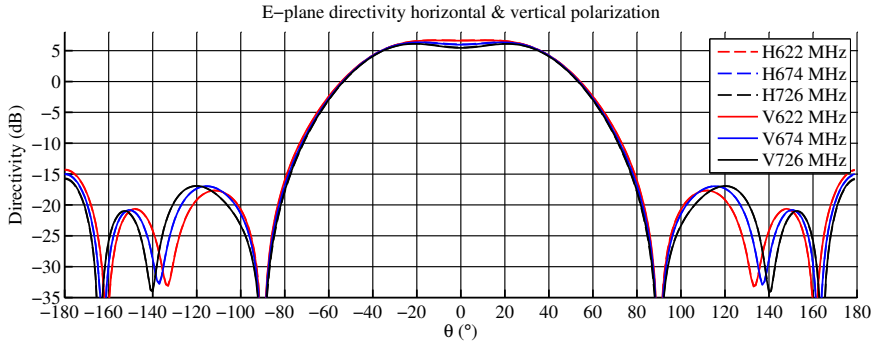

Figure 4.17: Simulated E-plane co-polarization directivity for the horizontal and vertical bowtie. The HPBW is $\approx 87°$ with a maximum directivity $D_0 \approx 6.2$ dB

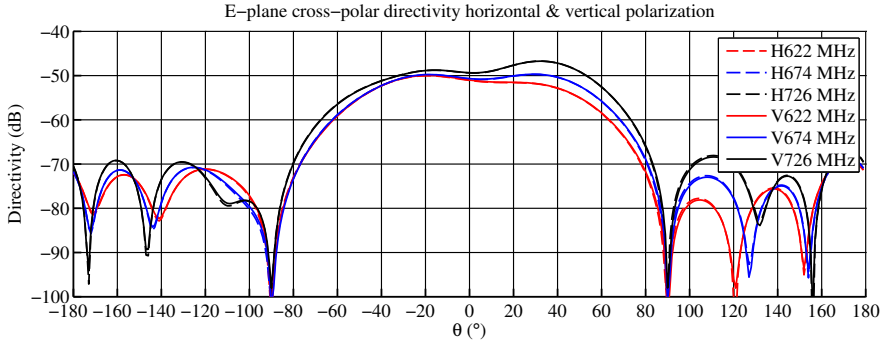

Figure 4.18: Simulated E-plane cross-polarization directivity for the horizontal and vertical bowtie

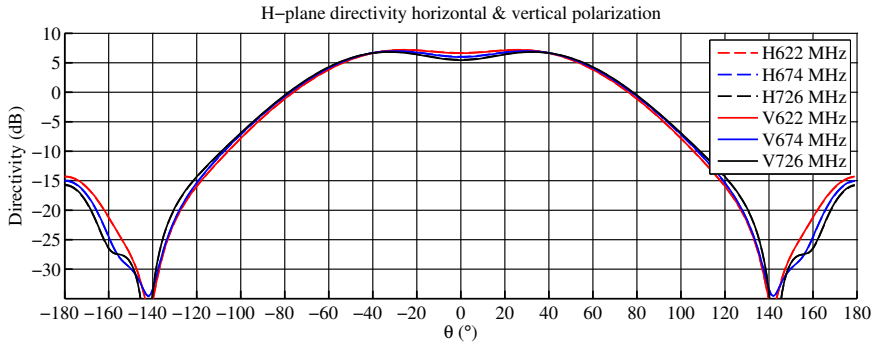

Figure 4.19: Simulated H-plane co-polarization directivity for the horizontal and vertical bowtie. The HPBW is $\approx 122^\circ$ with a maximum directivity $D_0 \approx 6.2$ dB

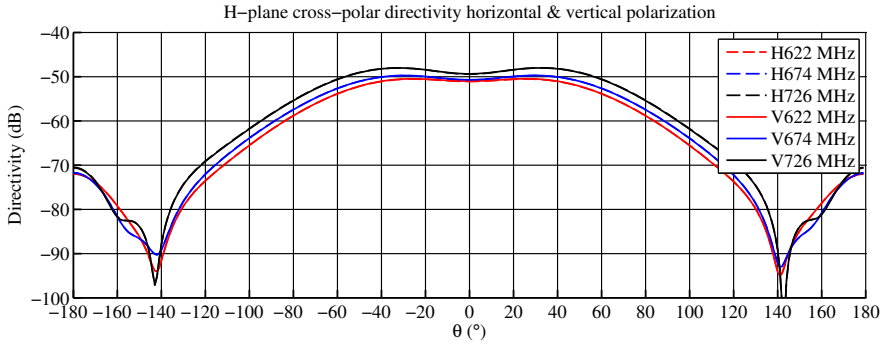

Figure 4.20: Simulated E-plane cross-polarization directivity for the horizontal and vertical bowtie

From simulations in CST, the crossed bowtie antenna shows promising characteristics in terms of impedance bandwidth and radiation pattern. One downside however, is the large beamwidth in the H-plane which is large compared to the desired 45°. The low cross-polar levels are probably due to the high isolation between the antenna ports, resulting in low cross-polar excitation.

4.4 Linear array of 11 elements

4.4.1 Array simulations in CST

Array simulations in CST Microwave Studio can be carried out in two different ways; either simulating the whole array or by using the infinite array approach. The infinite array approach emulates the situation of an infinite array with all the elements excited simultaneously, by simulating a single element. This is done by applying periodic boundary conditions on the bounding box in the array axis planes, where a phase shift can be added between the boundaries to emulate a phased array. In terms of simulation time, the infinite array approach is a cost-effective solution when rigorous array optimization is necessary. This method however, can only be used to predict the performance of large arrays and is not suitable for small antenna arrays, which are dominated by edge element effects with each element having different characteristics (impedance and radiation patterns). To simulate small arrays in CST, all the elements must be excited either simultaneously or sequentially with the elements not excited being terminated with their generator impedances. This leads to a significant increase in computational load making array optimization routines impractical for semi-large arrays.
In terms of post-processing, when all the ports and modes have been excited in an array, the results can be combined with arbitrary excitation conditions to obtain phased array performance. The results from combining either scattering parameters to get the active reflection coefficient at the elements, or combining the simulated fields to get the scanning radiation pattern yields the same results as if all the ports in the array was excited simultaneously [35].

4.4.2 Design

The crossed bowtie element from the previous section showed promising characteristics as an array element based on the obtained impedance bandwidth and radiation pattern. An 11-element horizontal linear array of the this antenna is shown in Figure 4.21 as modelled in CST. All the elements in the array must be simulated, since this is a small array, where the infinite array approach leads to inaccurate results.

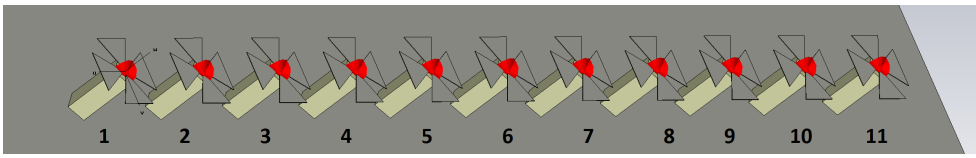

Figure 4.21: 11-element horizontal linear array of crossed bowtie antenna suspended above a ground plane. Discrete face ports are indicated in red

The whole structure in Figure 4.21 yields a large simulation domain (bounding box), in which the meshing must be dense enough to obtain sufficient accuracy. The size of the bounding box needs to be at least $\lambda/8$ at the lowest far-field monitor frequency to obtain an accurate near- to far-field transformation. In total, this yields a high number of mesh cells which increases the simulation time for each element significantly.

As the crossed bowtie antenna is placed in an array it is expected that the characteristics of the antenna in terms of radiation pattern and impedance will change due to the interaction with other elements. It may be necessary to tune some of the antenna parameters, which as mentioned earlier may take a long time due to the large simulation domain. In order to reduce the simulation time when tuning the elements within the array, some simplifications needed to be done. As the array in Figure 4.21 contains 11 dual polarized elements, which is a total of 22 ports that needs to be excited. Reduced simulation time was obtained by replacing the finite ground plane with a perfect electric conductor (PEC) boundary, which can be regarded as an infinite ground plane. Furthermore, by terminating all elements except for the center element (6) with 50Ω, the tuning of the center element in the array would not take too much time. This can be done since the middle element and its neighbours in the array will have approximately the same characteristics.

The antenna array is characterized by 4 parameters; bowtie arm length L_{arm}, flare angle α, the height above the ground plane h and the inter-element spacing d. Choosing a suitable element spacing d is, as mentioned earlier a trade-off between the required scan range at the highest operating frequency and the level of mutual coupling between the elements. Table 3.1 shows different element spacing and the corresponding maximum scan range for two maximum operating frequencies. By choosing $d = 220$ mm, the grating-lobe free scan range is $\theta_s = \pm 60^\circ$ at 726 MHz and $\theta_s = \pm 55^\circ$ at 750 MHz, which is above the required scan range of $\pm 45^\circ$. Keeping the height above the ground plane at $h = 130$ mm, the bowtie arm length L_{arm} and flare angle α was tuned until the impedance bandwidth of the center element was acceptable. The total number of mesh cells used in the simulation was approximately 8 million and the resulting geometrical parameters were;

$$L_{arm} = 65.5\text{mm}, \alpha = 62^\circ, h = 130\text{mm}, d = 220 \text{ mm}.$$

After tuning the center element, the whole array was simulated (22 excitations) with the infinite ground plane replaced with a ground plane of size 2640 mm x 880 mm.

4.4.3 Results

Impedance bandwidth

The simulated input reflection coefficient for each horizontally polarized element is shown in Figure 4.22, which is below the required -10dB between 624 MHz and 748 MHz for the center elements and 615-760 MHz for the edge elementes (1 and 11). As shown in the figure, the reflection coefficient for the center elements (2-10) has approximately the same reflection coefficient, while the edge elements deviates with higher bandwidth. These results almost fulfil the second bandwidth requirement (622-750 MHz).
For the vertically polarized elements the simulated input reflection coefficient is shown in Figure 4.23. It can be seen from the figure that the response of the center elements deviate a lot in resonance frequency (shifted down 15 MHz) compared to the edge elements which resonate at approximately 655 MHz. The bandwidth of both center and edge elements however, is below the -10 dB limit between 600 MHz and 800 MHz for the center elements and 605 MHz to 795 MHz for the edge elements. These results are even better than

the ones obtained from a single crossed bowtie element, which could imply that there is a significant amount of parasitic excitation between the vertically polarized elements.

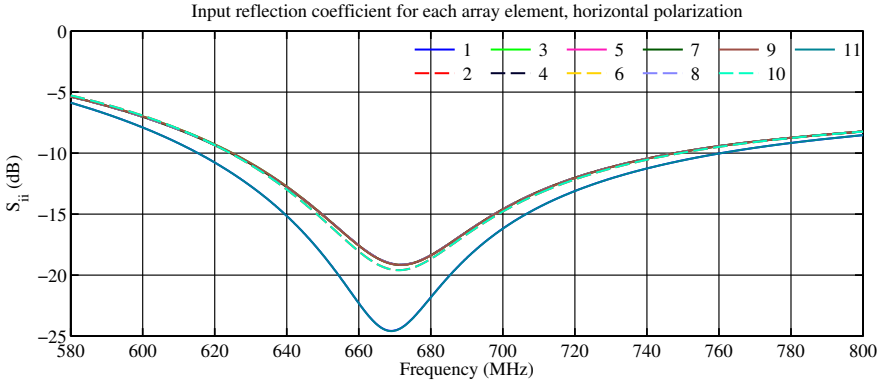

Figure 4.22: Input reflection coefficient for each horizontally polarized element in the linear array. The center elements (3-9) have overlapping characteristics, while element 2 and 10 deviate only slightly from this. The edge element (1 and 11) also has overlapping characteristics, however with a wider bandwidth than the center elements.

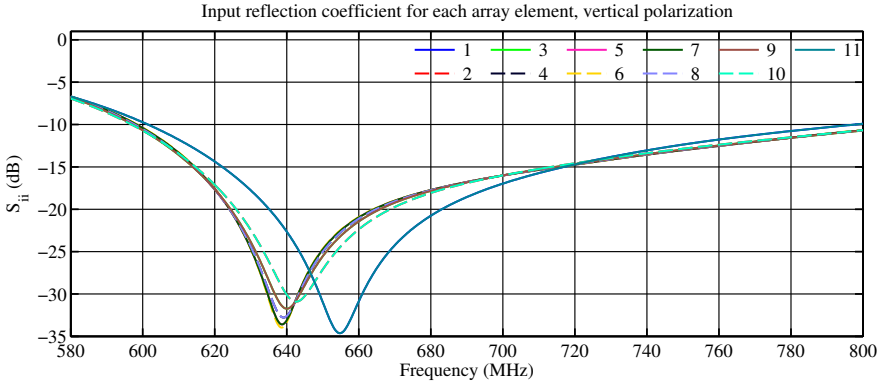

Figure 4.23: Input reflection coefficient for each vertically polarized element in the linear array. The center elements (2-10 shows more or less equal characteristics with an impedance bandwidth of approximately 200 MHz while the edge elements shows a bandwidth of 190 MHz with a resonance frequency at 655 MHz compared to 640 MHz for the center elements.

Mutual coupling

The mutual coupling between the center elements and its neighbours is shown in Figure 4.24 and 4.25 for the horizontally and vertically polarized elements respectively. For the horizontally polarized element, the coupling to its closes neighbour ($S_{5,6} = S_{7,6}$) is at -12 dB maximum at approximately 650 MHz. The maximum coupling for the vertically polarized element ($S_{5,6} = S_{7,6}$) is ≈ -11.5 dB at 620 MHz. When comparing the results in the two figures, it can be seen that the coupling is stronger for the vertically polarized elements throughout the frequency range. This difference in mutual coupling for the two polarizations is expected, since dipoles arranged in a side-by-side configuration (the vertically polarized elements) exhibit higher mutual coupling than the co-linearly arranged dipoles (the horizontally polarized elements)[7, p.469].

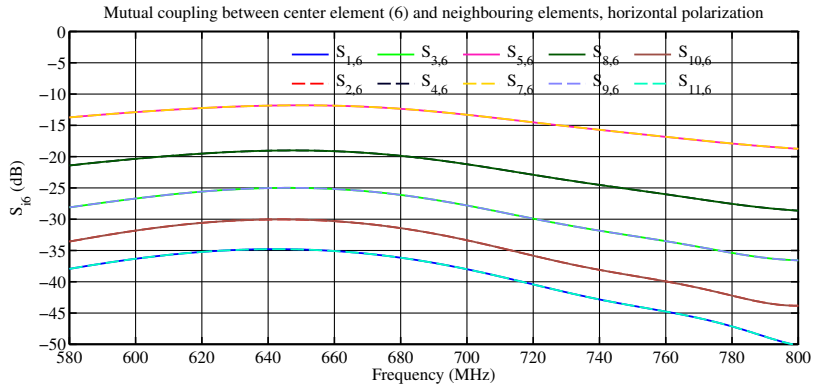

Figure 4.24: Mutual coupling expressed by scattering parameters between the center element and its neighbouring elements, horizontal polarization

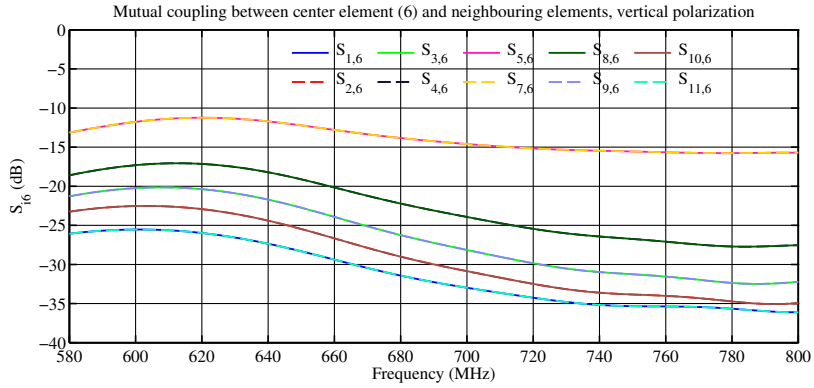

Figure 4.25: Mutual coupling expressed by scattering parameters between the center element and its neighbouring elements, vertical polarization

Center element radiation pattern

Horizontal polarization

Figure 4.26 and 4.27 shows the simulated E-plane co- and cross-polar directivity for the horizontally polarized bowtie for 622, 674 and 726 MHz. The maximum E-plane directivity is $D_0 \approx 6.36$ dB at approximately $\theta = 55°$, where the directivity at zenith is 1.2 dB below this. The half-power beamwidth is approximately $122°$, which is $35°$ wider than what was obtained with the single crossed bowtie. There is obviously a lot of parasitic excitation of other elements in the array, increasing the beamwidth. The cross polarization directivity is at -65 dB maximum at 726 MHz, which is extremely good polarization purity, which cannot be expected to be realized.

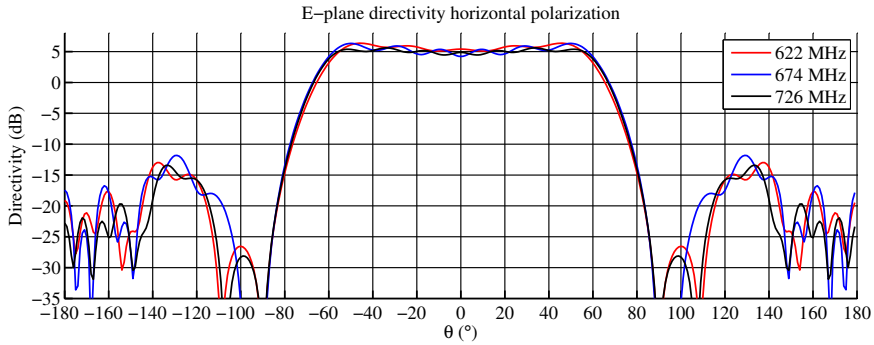

Figure 4.26: E-plane co-polar directivity horizontal polarization. The maximum directivity is approximately 6.3dB with a 1.2dB ripple at zenith. The HPBW is $122°$

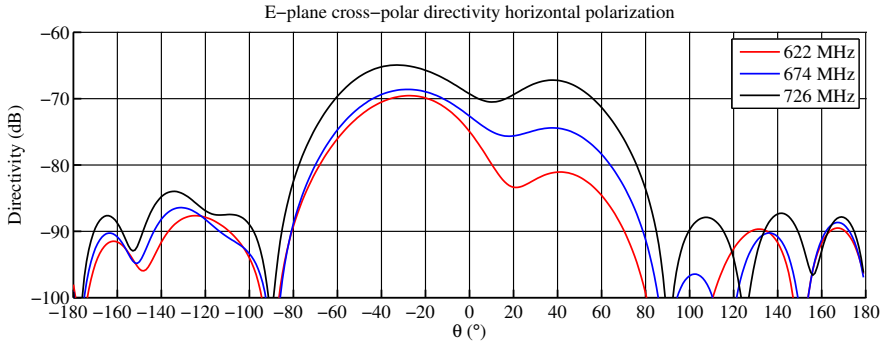

Figure 4.27: E-plane cross-polar directivity horizontal polarization, with a maximum cross-polar level of -65dB

The H-plane directivity in Figure 4.28 shows a maximum directivity of $D_0 \approx 5.8$ dB with a half-power beamwidth of $120°$, which is almost the same as what was achieved with the single element. This is expected as there are no elements stacked vertically to obstruct the radiation in this plane.

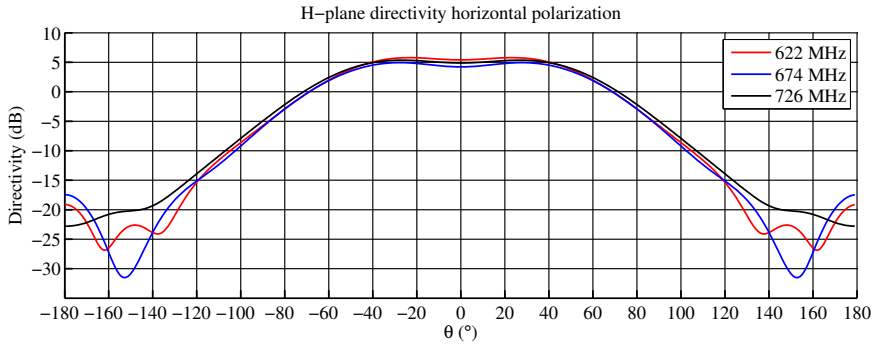

Figure 4.28: H-plane co-polar directivity horizontal polarization. The maximum directivity is approximately 5.8dB with a ripple of 1.2dB at zenith. HPBW of approximately $120°$

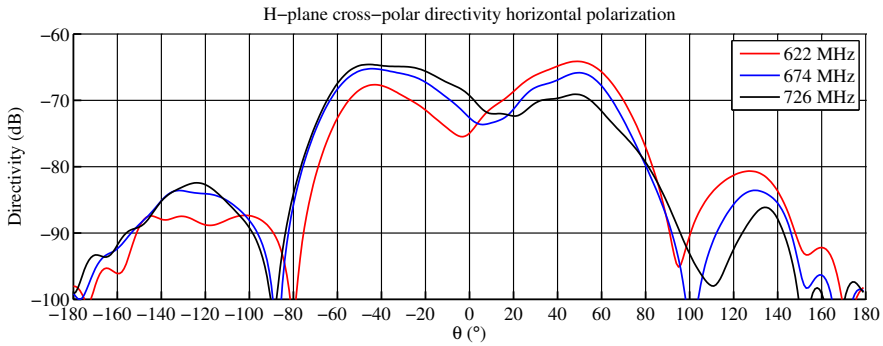

Figure 4.29: H-plane cross-polar directivity horizontal polarization with a maximum cross-pol level of -65dB

Vertical polarization

Figure 4.30 shows the simulated E-plane co-polar directivity for the vertically polarized element, where the maximum directivity is approximately 7dB at 726 MHz and 5.4 dB at 622 MHz. The half-power beamwidth is approximately 88°. As with the H-plane for the horizontally polarized element, this plane is not obstructed by any neighbouring elements, making the radiation pattern almost equal to that for the single element. The cross-polar directivity is shown in Figure 4.31 with a maximum cross-polar level of -64dB.

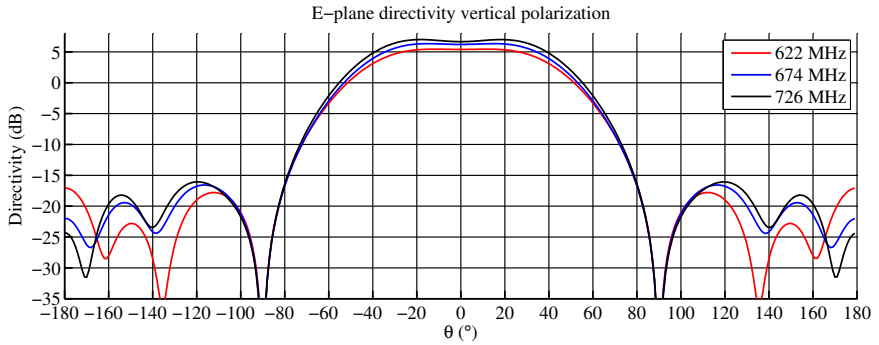

Figure 4.30: E-plane co-polar directivity vertical polarization, with a maximum directivity of 7dB at 726 MHz and 5.4 dB at 622 MHz. The HPBW is approximately 88°

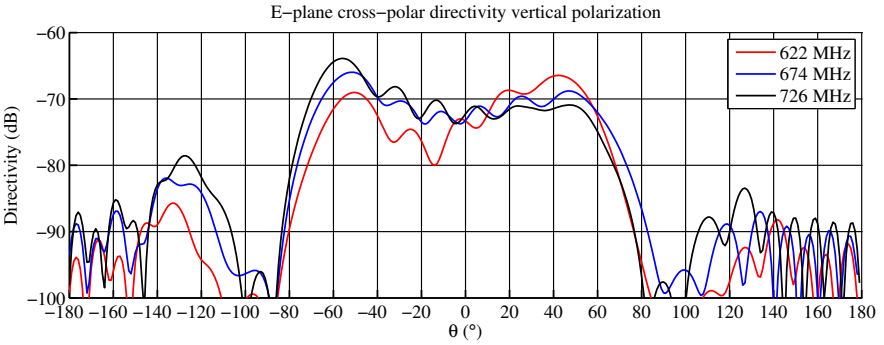

Figure 4.31: E-plane cross-polar directivity vertical polarization, maximum cross-polar level approximately -64dB

The simulated H-plane co- and cross-polar directivity is shown in Figure 4.32 & 4.33 for the vertically polarized element. As the H-plane for the vertically polarized element is the horizontal plane, changes in the radiation pattern is expected as with the E-plane for the horizontally polarized element. The maximum H-plane directivity is approximately 7.56dB with a 0.9dB ripple at zenith, and the HPBW is approximately 126° at 726 MHz and 130° at 622 MHz. There is evidently a significant amount of parasitic excitation of neighbouring elements, resulting in ripples in the pattern. The cross-polar H-plane directivity in Figure 4.33 shows a maximum cross-polar level of approximately -72dB.

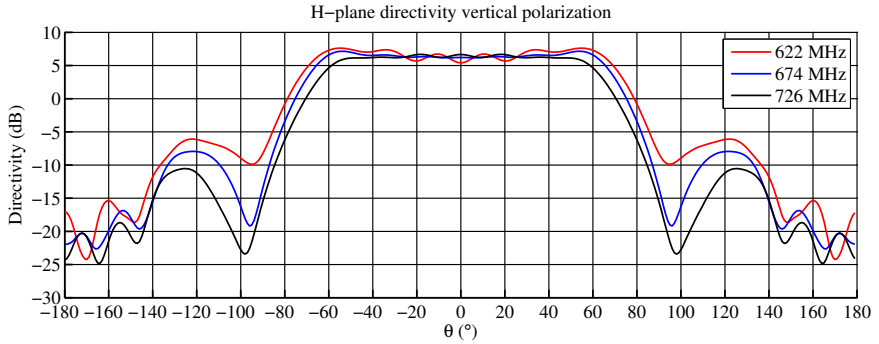

Figure 4.32: H-plane co-polar directivity vertical polarization, showing a maximum directivity of 7.56dB with a 0.9dB ripple at zenith. The HPBW is approximately 130° at 622 MHz.

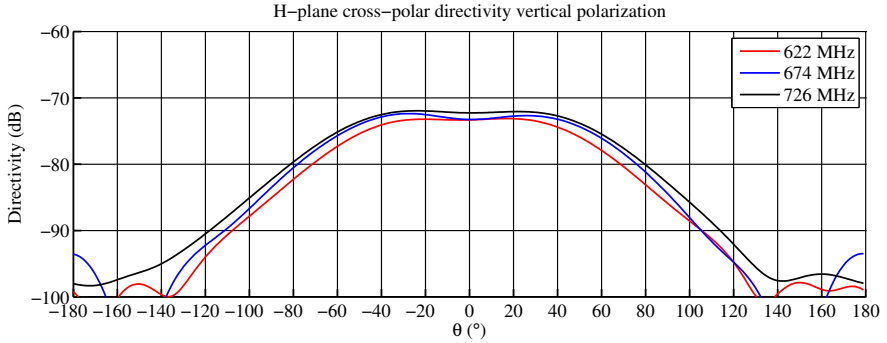

Figure 4.33: H-plane cross-polar directivity vertical polarization, showing a maximum cross-polar level at -72dB

4.4.4 Phased array performance

The antenna array is designed to work as a digital beamforming array, however it is just as valid to design the array as a transmitting phased array due to reciprocity. Assuming that the receiver itself is calibrated so that each channel is phase coherent and without amplitude errors, then the result from combining the signals digitally with a linear phase weight produces the same spatial pattern response as if the array was transmitting. Evaluating phased arrays in CST can be done either by simultaneous excitation of all the elements, or by combining the results from the simulations of *all* the elements. These two approaches are equivalent and produce the same results in CST [35]. Using the method of field combination, the total phased array directivity can be found by applying uniform amplitude weighing and a linear phase shift to the results from each element. The phase increment used to scan the array is calculated using Eq.(2.17).

E-plane scan directivity, horizontal polarization

The E-plane phased array directivity for the horizontally polarized elements is shown in Figure 4.34, 4.35 & 4.36 for 674, 726 and 750 MHz respectively. The array is scanned from broadside and out to -60° and the results are normalized to the maximum directivity at broadside. In the specification section the anticipated phased array directivity for a 11 element array was plotted in Figure 3.3, where the element factor corresponded to a half-wave dipole suspended above a ground plane. By comparing this with the phased array directivity obtained here it can be seen that as the array is scanned, the main lobe gets wider as expected from the array factor but the maximum directivity is not reduced. The maximum array directivity is approximately 1 dB higher at -60° than at broadside, which can be explained by looking at the E-plane radiation pattern of the center element. This radiation pattern actually has its maximum directivity at approximately $\pm 55^\circ$ with approximately 1.2 dB higher directivity as compared to 0°.

The side-lobe level (SLL) at broadside is approximately -12.5dB, which is slightly greater than the theoretical achievable SLL of -13.5dB on arrays exited with uniform amplitude. When the array is scanned, the SLL increases and at -60 degrees the SLL at $\theta \approx -35^\circ$ is approximately -7.5dB. As the frequency increases and the array is scanned to -60°, a growing grating lobe appears at $\theta \approx 60^\circ$. At 674 MHz this side-lobe is at approximately -13dB, increasing to -8.2dB at 726 MHz and all the way up to -3.6dB at 750 MHz. This behaviour is expected, as the inter-element spacing d was chosen based on a compromise between grating-lobe free scan range and mutual coupling. From the Specification section, the grating-lobe free scan range should have been 60 degrees at 726 MHz and 55 degrees at 750 MHz with a 220 mm inter-element spacing. The obtained results is actually somewhat better than expected, since the condition on grating-lobe free scan range is based on when the grating lobe is at the same level as the main lobe. At 726 MHz the grating lobe is located at $\approx 68^\circ$ is attenuated due to the element radiation pattern at this angle.

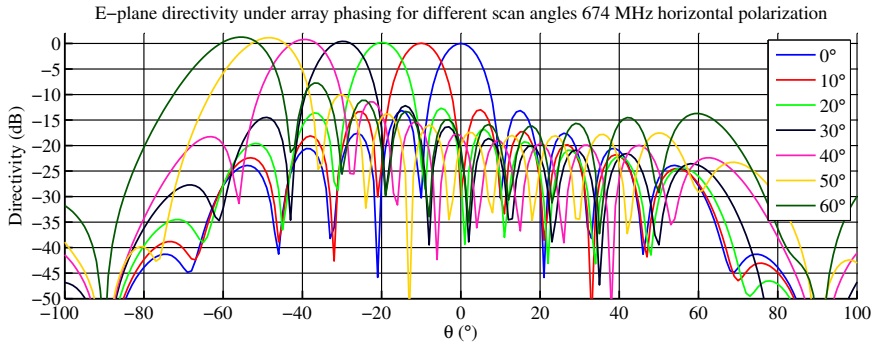

Figure 4.34: E-plane phased array directivity scanned from broadside to 60°, horizontal polarization, 674 MHz, normalized with respect to the maximum directivity at broadside

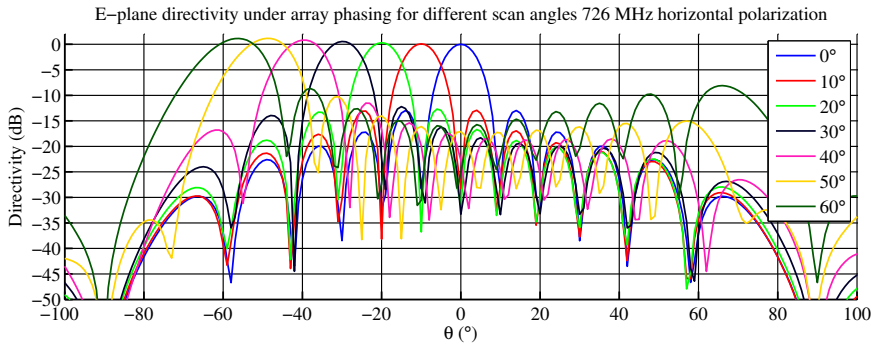

Figure 4.35: E-plane phased array directivity scanned from broadside to 60°, horizontal polarization, 726 MHz, normalized with respect to the maximum directivity at broadside

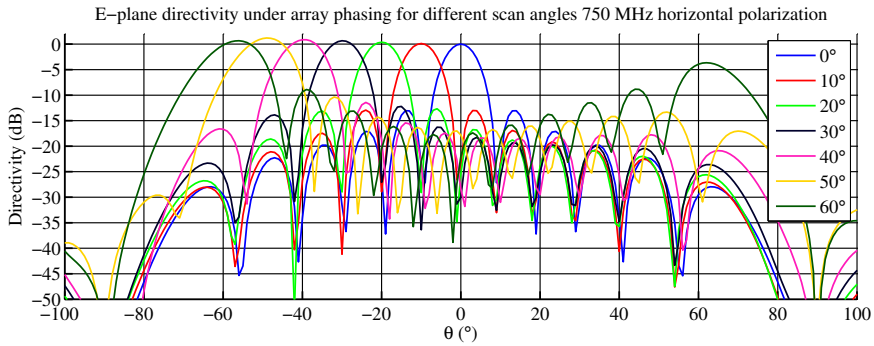

Figure 4.36: E-plane phased array directivity scanned from broadside to 60°, horizontal polarization, 750 MHz, normalized with respect to the maximum directivity at broadside

H-plane scan directivity, vertical polarization

For the vertically polarized elements, the horizontal scan corresponds to a H-plane scan. Again the simulated phased array directivity is shown in Figure 4.37, 4.38 & 4.39 for 674, 726 and 750 MHz respectively. Many of the results found in the E-plane scan for the horizontally polarized elements are also valid here. One of the major differences is that the element radiation pattern for the vertically polarized element (H-plane) has a wider beamwidth, where the maximum directivity is at $\approx 60^\circ$ for 674 MHz. The roll-off factor in this plane is also smaller, resulting in the wide main lobe when the array is scanned to -60 degrees away from broadside. As with the horizontally polarized elements, there is a grating lobe appearing when the array is scanned to -60 degrees. At 726 MHz the grating-lobe level is at -7.5 dB and even greater at 750 MHz at a level of approximately -3dB.

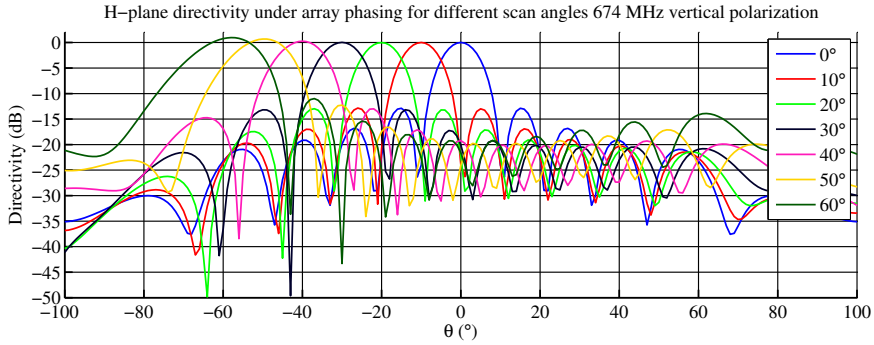

Figure 4.37: H-plane phased array directivity scanned from broadside to 60°, vertical polarization, 674 MHz, normalized with respect to the maximum directivity at broadside

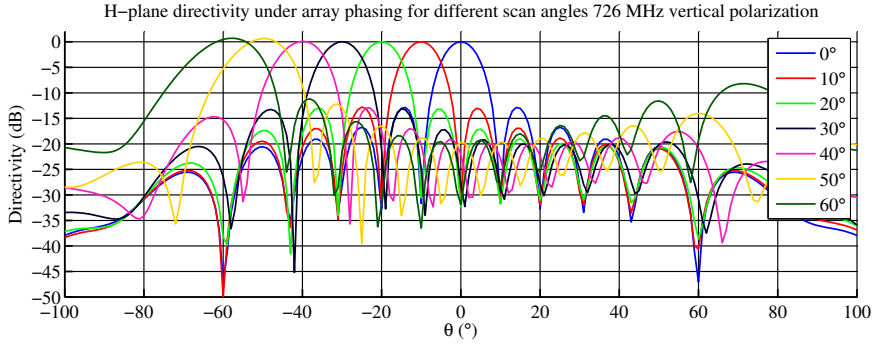

Figure 4.38: H-plane phased array directivity scanned from broadside to 60°, vertical polarization, 726 MHz, normalized with respect to the maximum directivity at broadside

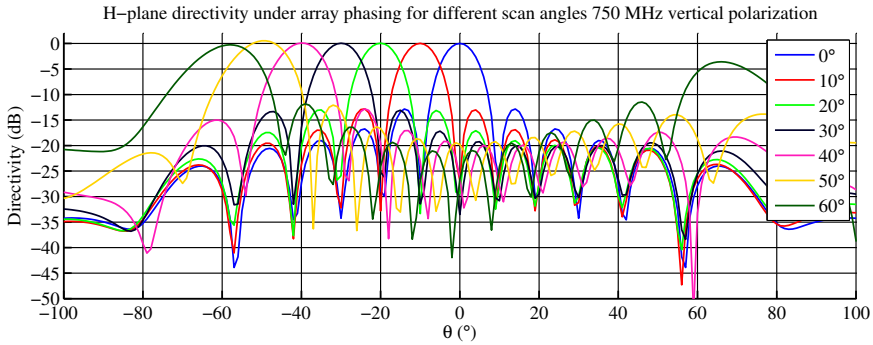

Figure 4.39: H-plane phased array directivity scanned from broadside to 60°, vertical polarization, 750 MHz, normalized with respect to the maximum directivity at broadside

To summarize, the grating-lobe free scan range is $\pm 50^\circ$ in both planes up to 750 MHz, where a scan range of $\pm 60^\circ$ is obtainable *if* the grating lobes can be reduced using pattern nulling at these angles.

Active reflection coefficient

Although the center element has an acceptable impedance bandwidth when it is the only excited element and the other elements are terminated in 50Ω, this might not be the case as when all the elements are excited simultaneously. Assuming that all the elements are excited with uniform amplitude, then the active reflection coefficient (ARC) Γ_a at the center element can be calculated with Eq.(2.24) using the simulated scattering matrix of the antenna array. This represents the reflection coefficient as seen from the generator when all the elements in the array are excited with uniform amplitude, taking the mutual coupling into account. Since good isolation between the vertically and horizontally polarized elements was good (≥ 50dB), only mutual coupling from co-polarized elements are taken into account in the active reflection coefficient.

Figure 4.40 shows the active reflection coefficient for the horizontally polarized elements with the array scanned from 0 to 60 degrees away from broadside, as for the phased array directivity in the previous section. When all the elements are excited simultaneously and scanned from 0 to 30 degrees, the reflection coefficient is below the -10dB limit from 590MHz to 775MHz, fulfilling the second bandwidth requirement. However, when the array is scanned further the reflection coefficient deteriorates, being below -10dB from 605 to 730 MHz when scanned to 40 degrees. Scanning to 50 degrees and 60 degrees severely deteriorates the reflection coefficient. One important result here is that there is no scan blindness appearing for either scan angles $\Gamma_a = 0$dB.

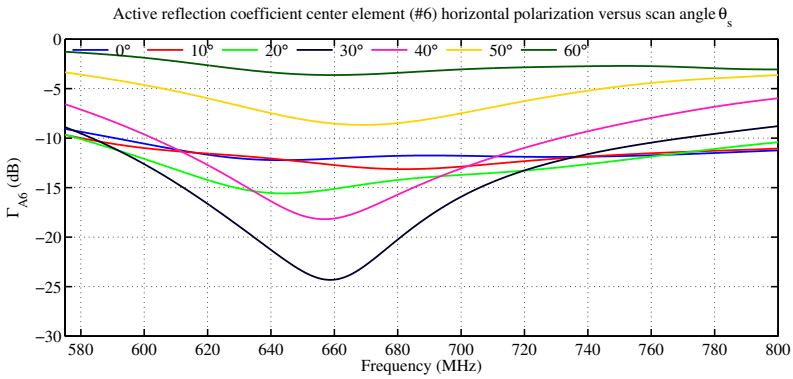

Figure 4.40: Active reflection coefficient for the center element, horizontal polarization, when scanned from 0 to 60 degrees

For the vertically polarized elements, the mutual coupling is stronger and thus affecting the active reflection coefficient severely. Figure 4.41 shows the simulated ARC for the same conditions as for the horizontally polarized elements. Even at broadside, the reflection coefficient is not below below the -10dB limit in any of the bandwidth specifications. The effect of strong mutual coupling between the elements in the frequency range 600-660 MHz is affecting the ARC severely at these frequencies. The ARC is below the -10dB limit for the first bandwidth requirement only when the array is scanned to 30 and 40 degrees. When the array is scanned to 50 degrees, the mutual coupling effect actually makes the array quite wideband in the frequency range 560 MHz to 680 MHz.

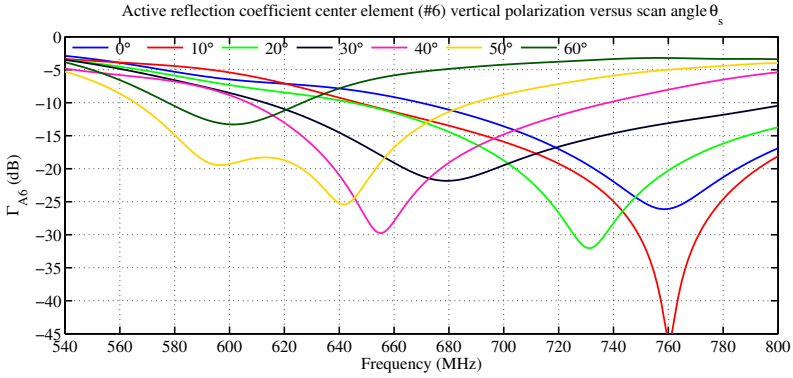

Figure 4.41: Active reflection coefficient for the center element, vertical polarization, when scanned from 0 to 60 degrees

To illustrate how the active reflection coefficient is affecting the antenna array, one can relate the reflection coefficient with the directivity of the different elements. The absolute gain G_{abs} of a lossless antenna (with no conductor- or dielectric losses) is given by Eq.(4.1), where Γ is the input reflection coefficient of the antenna and $D(\theta, \phi)$ is the directivity [7, p.67].

$$G_{abs} = (1 - |\Gamma|^2)D(\theta, \phi) \tag{4.1}$$

When all the elements in the 11-element array is excited with uniform amplitude with a linear phase shift in order to scan the main lobe to arbitrary angles, the reflection coefficient at the center element as seen from the generator is given as the active reflection coefficient. The ARC can replace the reflection coefficient in Eq.(4.1), making the absolute gain of the center element depend on the how the array is scanned and the degree of mutual coupling between the elements. The factor $(1 - |\Gamma|^2)$ can be regarded as a antenna mismatch loss, and can be expressed in dB by Eq.(4.2). This mismatch loss can be subtracted from the element maximum directivity to evaluate the absolute maximum gain.

$$ML = -10\log_{10}(1 - |\Gamma_a|^2) \tag{4.2}$$

Looking at the active reflection coefficient for the center element of the 11-element array (Fig. 4.42 & Fig. 4.43). When the array is scanned to 60 degrees, the ARC is approximately -3dB for both horizontal and vertical polarization. This leads to a mismatch loss of 3dB, resulting in half the radiation efficiency of the center element. When the array is scanned to 50 degrees, the maximum ARC is approximately -7dB for both polarizations, corresponding to a mismatch loss of approximately *1 dB*. If now the ARC is equal for all the elements within the array, this mismatch loss would simply decrease the total directivity of the whole antenna array with approximately 1 dB, from the property of pattern multiplication. However, the active reflection coefficient cannot be approximated as equal for all the elements in a small antenna array, thus the effect is different for each antenna element in the array.

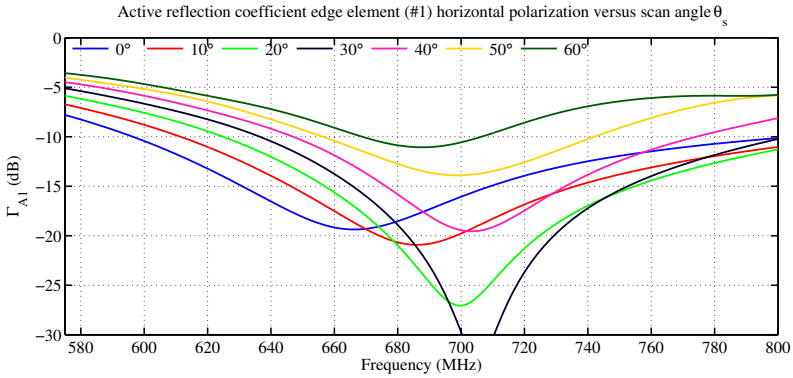

Figure 4.42: Active reflection coefficient for the edge element (1), horizontal polarization, when scanned from 0 to 60 degrees

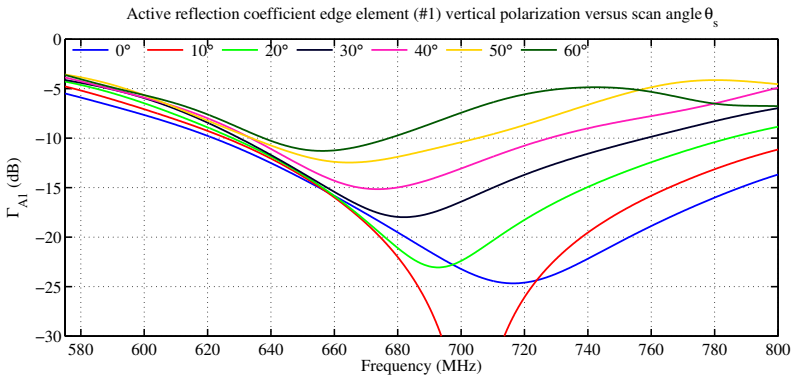

Figure 4.43: Active reflection coefficient for the edge element (1), vertical polarization, when scanned from 0 to 60 degrees

Figure 4.42 & 4.43 shows the active reflection coefficient for the horizontally and vertically polarized edge element of the full array (element 1). As can be seen in the figures, the ARC for the edge element is less severe than for the center element. One can then use the center element ARC as an estimate of a worst case scenario in terms of mismatch loss due to the mutual coupling in a phased array.

Relating the results to the passive bistatic radar array in question, it is just a matter of array efficiency in extracting energy from impinging plane waves. Since the effect of receiving a plane wave with a direction of arrival of, lets say, $\theta = 50°$, is the same as for a phased array transmitting in the same direction, it is found that a reduced maximum directivity of the whole array of approximately 1 dB is within acceptable limits. If the array were transmitting, the case would be quite differently as the mismatch would result in power being reflected back into the source, which could potentially cause amplifier break down or severe heating.

4.5 Summary of the simulated results

Table 4.1: Obtained simulation results versus desired for the center element in the 11-element array

	Simulated	Desired
Element impedance bandwidth h-pol	624-748 MHz	622-750 MHz
Element impedance bandwidth v-pol	600-800 MHz	622-750 MHz
E-plane HPBW h-pol	122°	90°
H-plane HPBW h-pol	120°	45°
E-plane HPBW v-pol	88°	45°
H-plane HPBW v-pol	130°	90°
Grating-lobe free scan range h-pol	±50°	±60°
Grating-lobe free scan range v-pol	±50°	±60°
Max. ARC. within bandwidth h-pol	-6.8 dB @ $\theta_s = 50°$	-10 dB @ $\theta_s = 60°$
Max. ARC. within bandwidth v-pol	-7.2 dB @ $\theta_s = 0°$	-10 dB @ $\theta_s = 60°$

4.6 Array prototype

The results from the previous section looked promising in terms of impedance bandwidth and radiation patterns, and needs to be verified through measurements on a realized array. As the anechoic chamber at NTNU has a size limitation on antennas being measured, only a partial array can be constructed. By building a 5-element array, the center element has two neighbouring elements at each side which should give an approximation to how the center elements in a full array performs. Figure 4.44 shows the 5-element array as modelled in CST, where the results from these simulations are given in the next chapter, where a comparison between the measured and simulated results is presented.

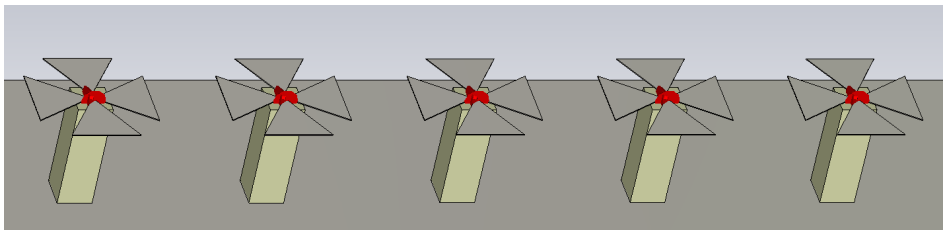

Figure 4.44: A 5-element linear array of crossed bowtie antennas as modelled in CST

The antennas simulated in CST had a thickness of 1 mm which can be approximated with a thin sheet of metal on a printer circuit board. By milling the elements out of a 1 mm thick FR-4 substrate ($\epsilon_r \approx 4.4$) coated with a thin layer of copper on each side, a low cost production is obtained. According to Bailey, the loading effect the substrate has on the antenna at these frequencies are negligible [33], making the antenna insensitive to variations in permittivity in the cheap FR-4 substrate.

4.6.1 Balun

The dipole antenna is a balanced structure and must therefore be excited from a balanced transmission line, such as the twin-lead transmission line. Connecting the dipole arms directly to the inner and outer conductors of a coaxial transmission line, results in in an unbalanced excitation causing a net current flow on the outside of the outer conductor of the coaxial cable[7, p.539]. The unbalanced currents give rise to unwanted radiation, and since the phase balance of the dipole is deteriorated, there will be a squint in the radiation pattern.[32, p.252]. A balun is a device which properly connects a balanced transmission line, such as the dipole antenna, to an unbalanced transmission line (balanced-*un*balanced). Some baluns also work as impedance transformers and therefore baluns are often referred to as balun transformers. There exists numerous of different baluns, in e.g. coaxial, ferrite and tapered [32, p.255-259]

Figure 4.45(a) illustrates the quarter-wave coaxial balun on a thin dipole antenna of length L, where one dipole arm is connected to the outer conductor of the main coaxial line whilst the other is connected to the main coaxial line center conductor. In order to obtain a balanced excitation of the dipole, an auxiliary quarter-wave coaxial line is connected

to dipole arm excited by the center conductor of the main coaxial. The auxiliary coaxial is shorted together with the main coaxial line outer conductor at the ground plane. The current flow on the outer conductor of the main coaxial line is cancelled at the point where the main and auxiliary lines are shorted, and does not necessarily needs to be exactly a quarter wavelength long in order to obtain balanced excitation [7, p.540]. Figure 4.45(b) shows the quarter-wave balun for the crossed bowtie antenna as modelled in CST, where the bowtie is a thin metal sheet on a piece of FR4 substrate

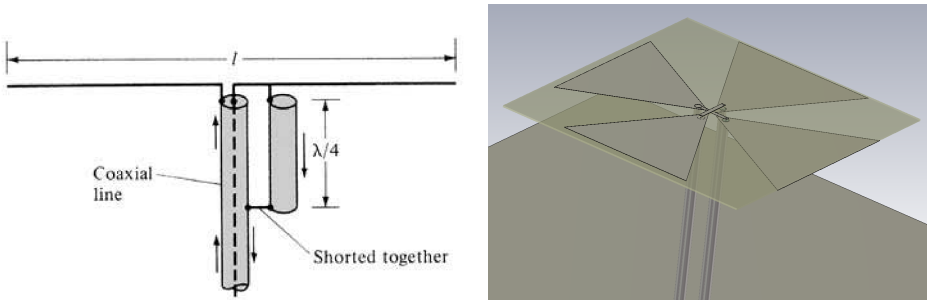

(a) (b)

Figure 4.45: (a) Quarter-wave coaxial balun, from [7], (b) The balun as modelled in CST with the crossed bowtie antenna

4.6.2 Prototype

The antenna support structure is shown in Figure 4.46 and is made out of Divinycell which is a closed cell medium density foam with high compression strength and low water absorption under long-term conditions.The material has a relative permittivity $\epsilon_r \approx 1.1$ which is close to that of air, reducing the influence of the support structure on the antenna performance. In Figure 4.46 there are 2 plastic pins inserted in order to mount the PCB to the Divinycell and the whole structure to the ground plane. The support structure measures 40x40x130 mm.

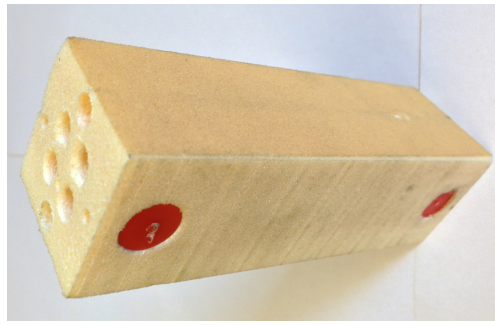

Figure 4.46: Divinycell support structure with 2 M3 holes for PCB mounting and holes for the coaxial feed lines.

As the quarter-wave coaxial balun has an impedance transformation ratio of 1:1 and that the crossed bowtie antenna is matched to 50Ω, the coaxial cable used in the balun must have 50Ω characteristic impedance. The coaxial cable used in the prototype is a semi-rigid cable from Huber & Suhner, model EZ-141 together with suitable panel mount SMA connectors. Figure 4.47 shows the prototype element (a) viewed from the side, showing the coaxial baluns and (b) viewed from top.

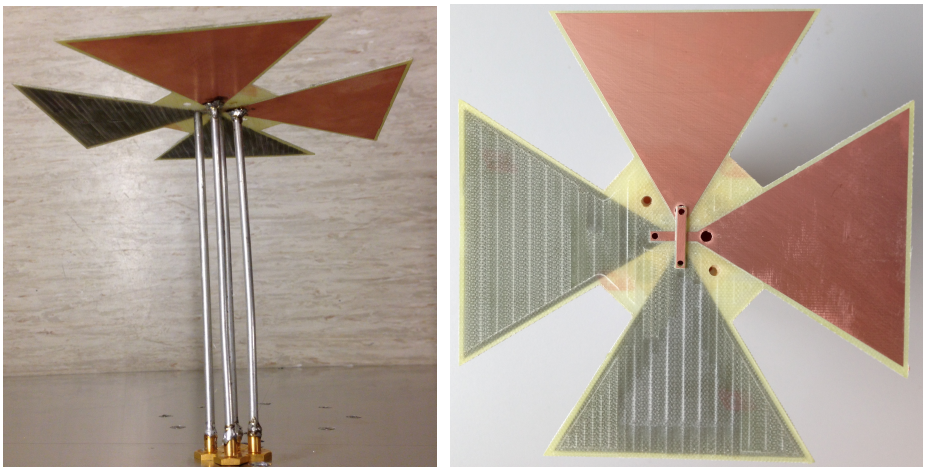

(a) (b)

Figure 4.47: (a) Side view of the array element without support structure, showing the coaxial balun. (b) Top view of the array element before soldering

The final array prototype is shown in Figure 4.48, with 5 elements mounted on a ground plane of size 1540x880 mm^2

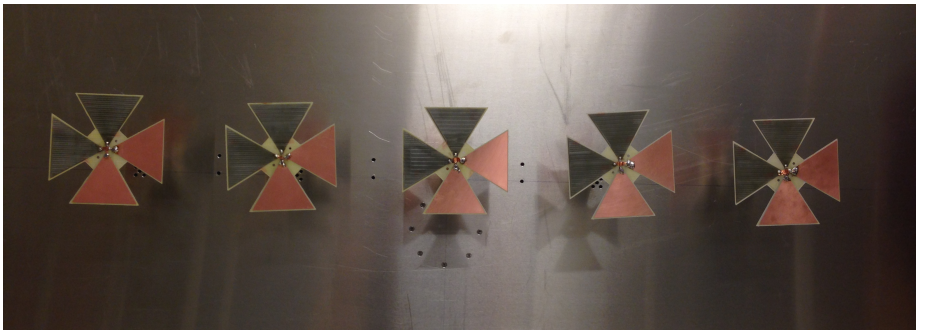

Figure 4.48: 5-element array prototype

Chapter 5

Measurements and results

5.1 Method

Measurements on the 5-element prototype array was conducted in the anechoic chamber at NTNU, which is suitable for frequencies between 800 MHz and 18 GHz. The reference antenna in the chamber was a wideband dual-ridged horn antenna (EMCO Model 3115[36]), covering the same frequency range. As the frequency range of interest (622 MHz - 750 MHz) is slightly below the specifications of both the chamber and reference antenna, it is expected slightly higher side-lobe levels due to reflections from the surrounding walls. Figure 5.1 shows the antenna array mounted on a rotating platform inside the anechoic chamber at NTNU. The radiation pattern of the *center element* is obtained by rotating the structure while measuring the transmission parameter S_{21} in the scattering matrix using a network analyser. As the reference antenna is not characterized at the frequencies of interest only the normalized radiation pattern is presented here, which is simply the recorded radiation pattern normalized with respect to its maximum value. The cross-polarization is normalized with respect to the maximum values of the co-polar patterns

Figure 5.1: The 5-element crossed bowtie array mounted in the anechoic chamber at NTNU

Measurement of input reflection coefficients and mutual coupling between the elements was done using a two-port network analyser, calibrated for the frequency range of interest using the SOLT (short-open-load-through) calibration routine (cal. kit HP85052D). When two ports were measured, all the other ports in the array were terminated using 50Ω SMA terminations.
The following results presents a comparison between the simulated results from a 5-element array in CST versus those obtained from measurements on the prototype. If the results obtained from measurements are close to those obtained from simulations in CST, then one can assume that the same will apply for a full 11 element array with performance according to the simulations shown in the previous section.

5.2 Impedance bandwidth

Figure 5.2 and 5.3 shows the simulated and measured input reflection coefficients for both the horizontally and vertically polarized elements. S_{33} corresponds to the center element in the array shown in Figure 5.1. For the horizontally polarized elements, it can be seen from Figure 5.2(b) that the resonance frequency of the center element is shifted up approximately 30 MHz, compared to the simulated results in Figure 5.2(a). The obtained reflection coefficient for the center element is below the -10 dB limit between 660 MHz to 800 MHz, which does not fulfill any of the required impedance bandwidths. However, the impedance bandwidth is approximately 140 MHz, which would fulfill the requirements if the length of the horizontal bowtie could be increased slightly to lower the resonance frequency 30 MHz.

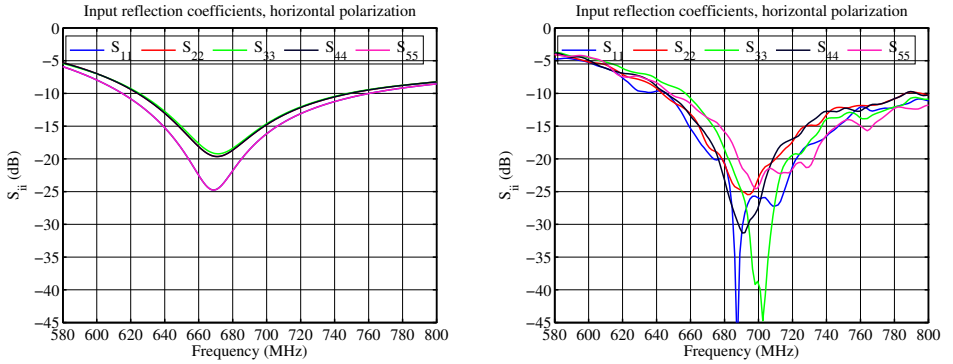

(a) Simulated

(b) Measured

Figure 5.2: Simulated (a) and measured (b) input reflection coefficient for each horizontally polarized bowtie in the 5-element array. S_{33} represents the center element, and the measured impedance bandwidth is approximately 140 MHz with a resonance frequency shifted up 30 MHz compared to the results obtained from simulations in CST.

The measured reflection coefficients for each vertically polarized element in the array is shown in Figure 5.3. Again, comparing the measured results with the simulated in Figure 5.3(a) shows there is significant difference between the two. The reflection coefficient

for the center element is below the -10dB limit from 615 MHz and beyond 800 MHz, fulfilling the second bandwidth requirement of 622 MHz to 750 MHz. Measurements above 800 MHz were not conducted since this is outside the frequency range of interest and the calibrated frequency range of the VNA.

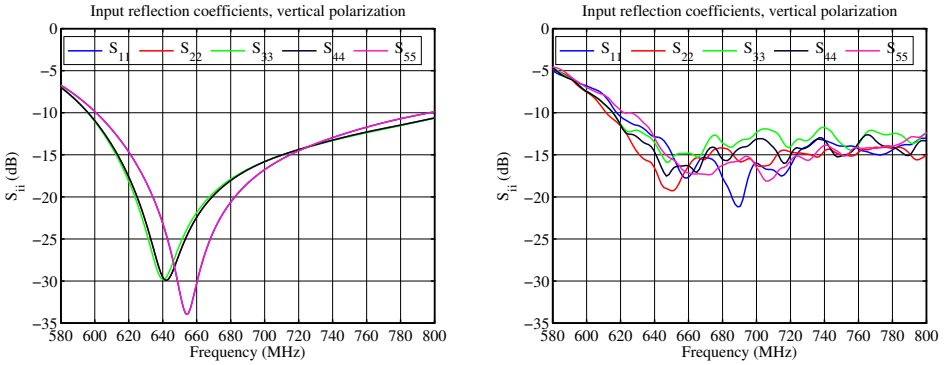

(a) Simulated

(b) Measured

Figure 5.3: Simulated (a) and measured (b) input reflection coefficient for each vertically polarized element in the array. The measured reflection coefficient for the center element is at an acceptable limit from 615 MHz and beyond 800 MHz.

In both Figure 5.2 and 5.3 there is a significant difference between the results obtained from simulations in CST and those from measurements on the prototype array. From a geometrical perspective the length and flare angle of prototype bowtie was more or less equal to the one simulated in CST, limited only by the accuracy of the milling machine. However, the quarter wave balun used to feed the crossed bowtie was not modelled in CST due to lengthy simulation runs. In CST the impedance reference plane was at the feed points of the bowtie, while the prototype array had an impedance reference plane at the end of the balun. In Figure 5.3(b) , the measured reflection coefficient for the center element crosses the -10 dB limit at approximately 615 MHz, shifted up approximately 20 MHz compared to the results from CST. For the horizontally polarized element, the -10dB crossing is shifted approximately 30 MHz up compared to the simulation results, which is a comparable amount applying to both elements. It is therefore suspected that the balun itself changes the resonance frequency of the antenna.

5.3 Mutual coupling

The simulated and measured mutual coupling between the center element and its neighbours is shown in Figure 5.4 and 5.5. Examining the pairs S_{23} & S_{43} and S_{13} & S_{53} which are pairwise identical in the results obtained from simulations, are no longer identical for the prototype array. This is to be expected solely based on differences in production. Aside from this difference, the coupling between both horizontally and vertically elements follow the same trend as the results obtained from CST. The shift in resonance frequency, discussed previously, is visible in both of the figures when comparing to the simulation results. For the horizontally polarized elements the frequency of maximum coupling is shifted from approximately 640 MHz to 670 MHz, while the shift is from roughly 615 MHz to 625 MHz for the vertically polarized elements.

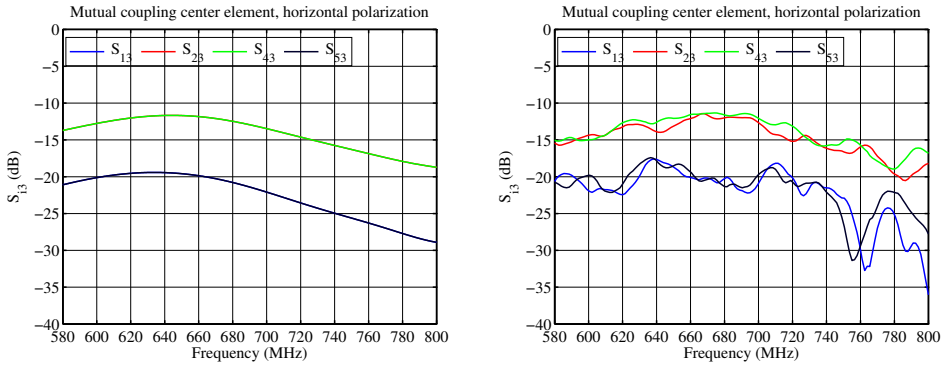

(a) Simulated (b) Measured

Figure 5.4: Simulated (a) and measured (b) mutual coupling between the center element and neighbouring elements, horizontal polarization.

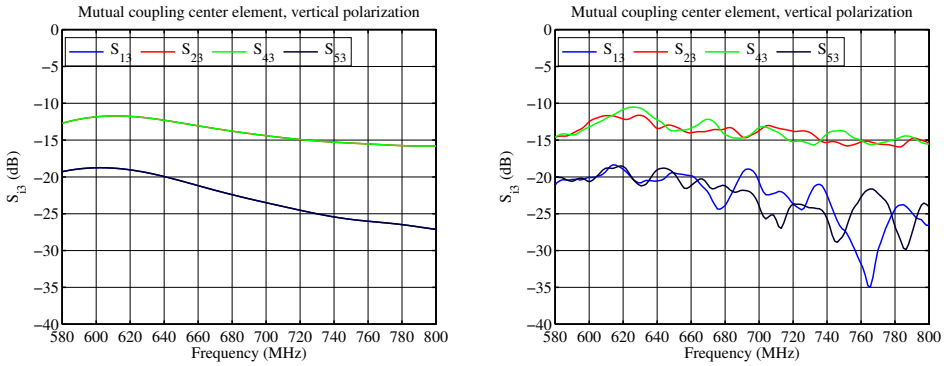

(a) Simulated (b) Measured

Figure 5.5: Simulated (a) and measured (b) mutual coupling between the center element and neighbouring vertically polarized elements

5.4 Cross-polar mutual coupling

In the design chapter, the mutual coupling between the horizontally and vertically polarized bowtie in the crossed bowtie antenna was formidable. For the 5-element array of crossed bowtie antennas, the simulated coupling is shown in Figure 5.6(a) with the measured in Figure 5.6(b). The measured coupling is over three orders of magnitude stronger than the simulated results.

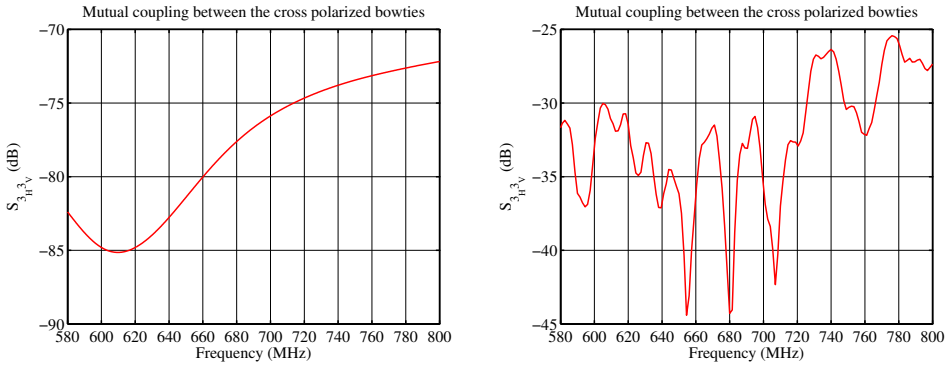

(a) Simulated (b) Measured

Figure 5.6: Simulated (a) and measured (b) isolation between the horizontally and vertically polarized bowtie in the center element crossed bowtie antenna. The coupling to the cross-polarized bowtie in the prototype is ≈ -27dB within the frequency band of interest. This approximately 46 dB less isolation than what was simulated.

The coupling obtained from simulations in CST is somewhat expected to be low, since each element was fed with two completely isolated discrete face ports. The discrete ports were not overlapping in any way like the overlap bridge needed for the balun in the prototype element. Compared to the isolation obtained in [34] ($S_{12} \approx -30$dB) which was regarded as a high-isolation element, the results from the measured crossed bowtie antenna should be satisfactory, being ≤ -30dB up to 725 MHz with a maximum of -27dB at 740 MHz.

5.5 Center Element Radiation Patterns

Radiation pattern measurements in the anechoic chamber was done by fixing the array on a rotating platform and measuring S_{21} using a vector network analyser. Since only the center element radiation pattern was of interest, all the other elements were terminated using 50Ω sma terminations. Rotating the array as shown in Figure 5.1 resulted in horizontal polarization co-polar E-plane radiation pattern, and by rotating the reference antenna $90°$, the cross-polar radiation pattern were obtained. Measurements of the H-plane co- and cross-polar was done in the same manner, only by rotating the array itself $90°$ with respect to its center. The same set of measurements were conducted for vertical polarization.

5.5.1 Horizontal polarization

Figure 5.7 & 5.8 displays the normalized simulated and measured co-polar E-plane and H-plane directivity for four different frequencies within the second bandwidth requirement (622MHz-750 MHz). The resulting radiation patterns in both planes are more or less equal to those obtained from simulations in CST, except for the higher side-lobe levels, which was anticipated as a consequence of measuring at frequencies below the specified frequency range of the chamber. The increased side-lobe level is especially noticeable at 622 MHz in both figures.

Table 5.1 shows the simulated and measured half-power beamwidths in the two principal planes, where the measurements shows a smaller beamwidth in the two planes for all frequencies except 622 MHz. At 622 MHz, the measured E-plane beamwidth is smaller than the simulated, however the H-plane beamwidth is wider.

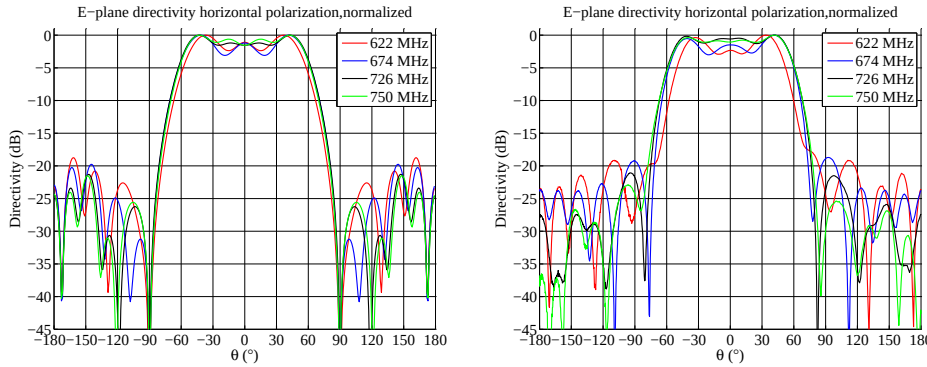

(a) Simulated (b) Measured

Figure 5.7: Simulated (a) and measured (b) normalized co-polar E-plane directivity for the center element, horizontal polarization

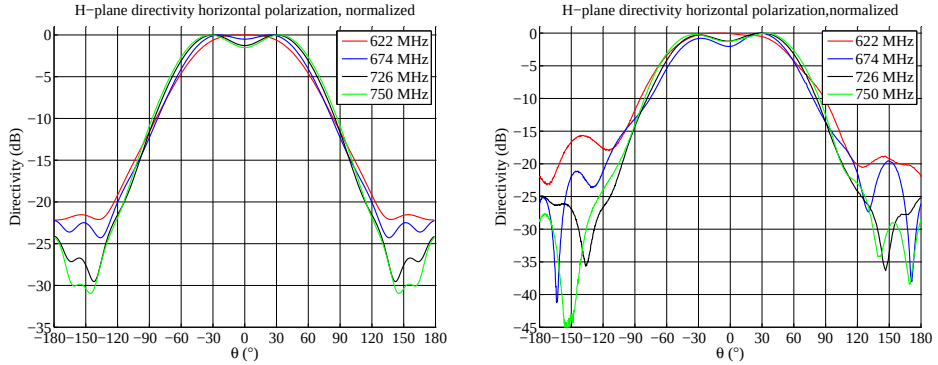

(a) Simulated (b) Measured

Figure 5.8: Simulated (a) and measured (b) normalized co-polar H-plane directivity for the center element, horizontal polarization

Table 5.1: Simulated and measured half-power beamwidth (HPBW), horizontal polarization

HPBW	**E-plane**		**H-plane**	
Frequency	Simulated	Measured	Simulated	Measured
622 MHz	106°	93°	102°	114°
674 MHz	116°	108°	109°	99°
726 MHz	116°	111°	119°	110°
750 MHz	115°	109°	123°	118°

The cross-polar radiation patterns are shown in Figure 5.9 & 5.13. It is evident that the cross-polarization levels on the prototype are severely higher than those obtained from simulations. The maximum E-plane cross polarization is approximately -17dB at 726 MHz compared to -66dB at 750 MHz simulated, a deviation of $\Delta \approx 50$dB.

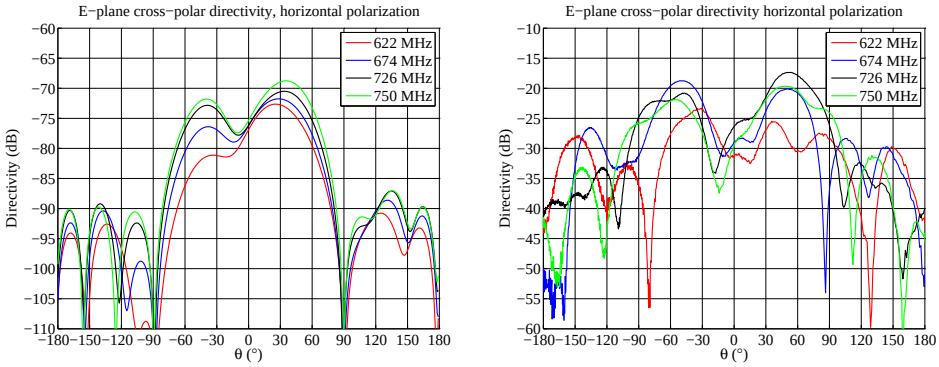

(a) Simulated (b) Measured

Figure 5.9: Simulated (a) and measured (b) normalized cross-polar E-plane directivity for the center element, horizontal polarization

In the H-plane, the cross-polarization has its maximum at -23dB measured, comparing to the simulated -69 dB the deviation is $\Delta \approx 46$dB. This increase in cross-polarization levels in both planes can be expected due to the increased mutual coupling between the vertical and horizontal bowtie in the center element. As shown in Figure 5.6, the deviation of $\Delta \approx 47$dB between the simulated and measured cross coupling are approximately equal to the difference between the simulated and measure cross-polarization levels in both planes. Comparing the achieved results with those in [34], where a cross-polar level of -24dB was obtained and regarded as *low* cross-polarization, the results obtained from the prototype array are satisfactory at a level of -25dB at zenith.

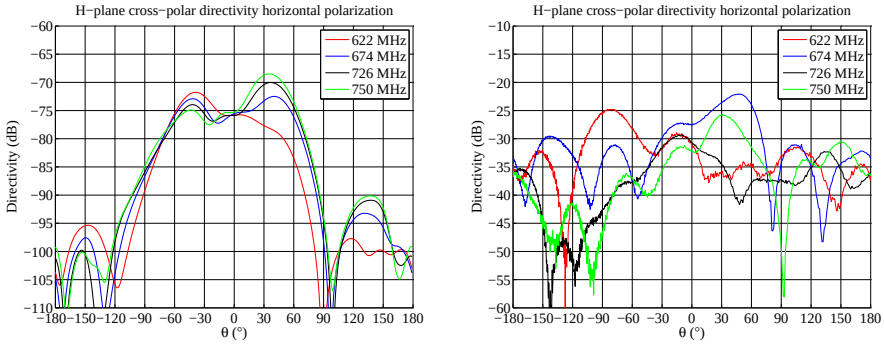

(a) Simulated (b) Measured

Figure 5.10: Simulated (a) and measured (b) normalized cross-polar H-plane directivity for the center element, horizontal polarization

5.5.2 Vertical polarization

Figure 5.11 & 5.12 shows the measured co-polar E- and H-plane radiation patterns, again with the simulated results.

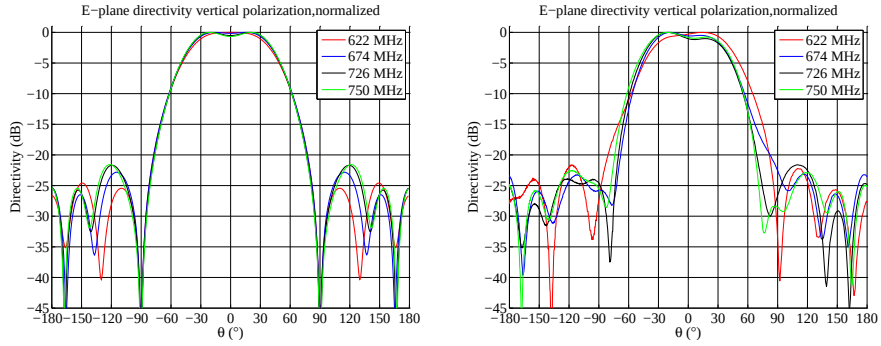

(a) Simulated (b) Measured

Figure 5.11: Simulated (a) and measured (b) normalized co-polar E-plane directivity for the center element, vertical polarization

The measured E-plane radiation pattern in Fig. 5.11, is not as symmetrical as the pattern obtained from simulations. At first, it was suspected that errors in the quarter-wave balun were causing a slightly unsymmetrical excitation of the antenna, which could result in a beam squint as that in the E-plane pattern. However, the beam squint is not visible in the measured H-plane pattern, which is symmetrical and almost equal to that of the simulated result. It is therefore suspected that the beam squint is due to non-perpendicular installation of the element above the ground plane, resulting in a poor short circuit between the coaxials at the ground plane, which is needed for the balun to work properly. The simulated and measured half-power beamwidths is shown in Table 5.2.

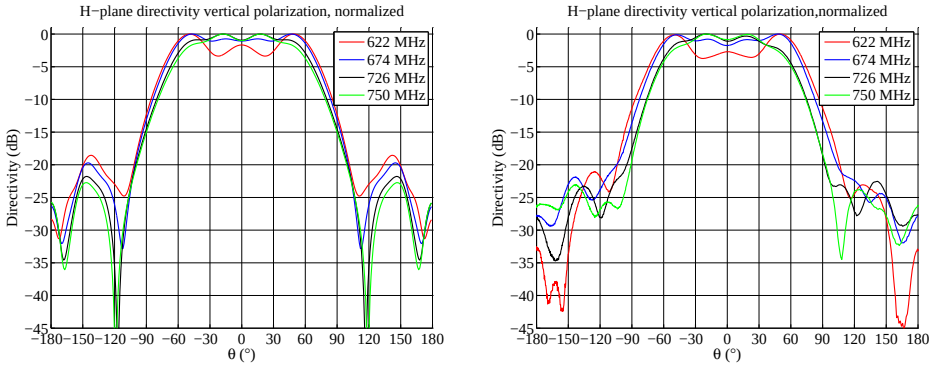

(a) Simulated (b) Measured

Figure 5.12: Simulated (a) and measured (b) normalized co-polar H-plane directivity for the center element, vertical polarization

Table 5.2: Simulated and measured half-power beamwidth (HPBW), vertical polarization

HPBW	**E-plane**		**H-plane**	
Frequency	Simulated	Measured	Simulated	Measured
622 MHz	83°	88°	136.4°	136°
674 MHz	86°	80.4°	132°	130°
726 MHz	87°	84.8°	120°	112°
750 MHz	87.6°	89.9°	113.6°	108°

Figure 5.13 & 5.14 shows the measured and simulated cross-polar radiation patterns in both E- and H-plane for the vertically polarized bowtie. In both planes the maximum cross-polar levels are at ≈ -23dB, again at level approximately 50dB above the simulated results.

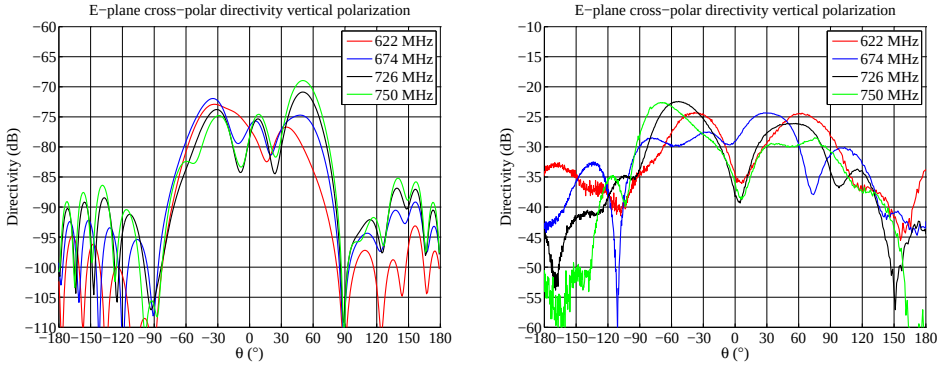

(a) Simulated (b) Measured

Figure 5.13: Simulated (a) and measured (b) normalized cross-polar E-plane directivity for the center element, vertical polarization

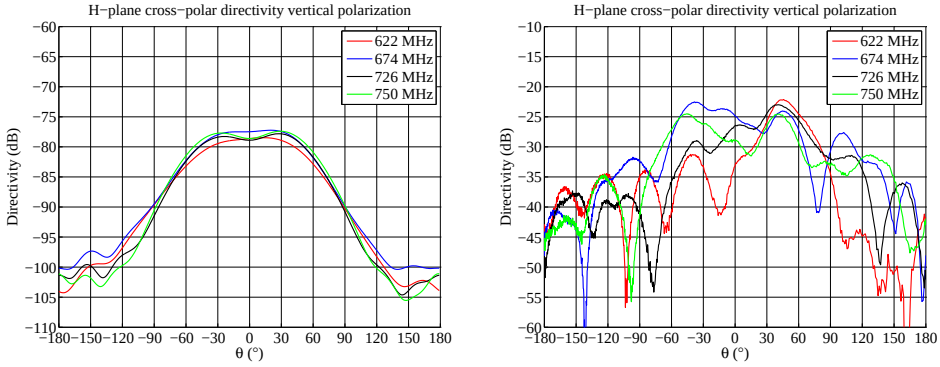

(a) Simulated (b) Measured

Figure 5.14: Simulated (a) and measured (b) normalized cross-polar H-plane directivity for the center element, vertical polarization

Chapter 6

Discussion

Most of the results obtained in both simulations and measurements have been discussed throughout the thesis and will not be repeated here. However, this might be a good time to discuss some of the practical issues related to the prototype array and how this may have affected the measurement results. Secondly a short discussion on the design approach used in the thesis is given and finally suggestions for future work are presented.

6.1 Practical issues

There were some practical issues related to the prototype array itself which may have had an effect on the measurements. The ground plane on which all the elements are mounted, was made out of a 2 mm thick aluminium plate to keep the weight as low as possible. As the size of the ground plane was quite large (1540 mm x 880 mm), it was twisting and turning and difficult to keep completely flat. This resulted in skewed element positioning, which is quite visible in Figure 4.48. Furthermore, since the quarter-wave coaxial balun is dependent on a good short circuit at the ground plane, the performance of the balun may have been deteriorated as an effect of a non-planar ground plane.

Looking at the layout of the crossed bowtie in Figure 4.47, both layers of the substrate were used to make it easier to solder outer conductor of the main coaxial cable to the bottom layer triangle, and letting the center conductor go through the substrate to be connected to the other triangle using a solder bridge. Under array production an issue related to this revealed itself, where the sma panel connectors and the bottom layer of the antenna could not be solder on with the support structure in between. For this reason, the Divinycell support structure had to be omitted in the measurements as there was no more time left to make new antenna elements. Using just the semi-rigid coaxial cables as support structure was good enough during measurements, however if the only thing actually keeping the antenna in place is the soldering to the coaxial cables, then only a small amount of force on the antennas could break it.

The idea of using the Divinycell structure was to make it easier to connect and disconnect the elements from the array, as well as giving additional support. By fastening the crossed bowtie to the Divinycell using two m3 screws, the solution would be sturdy and fit for assembly/disassembly as the array is tried out in different locations. Whether this had a substantial effect on the measured result is hard to determine, as the structure was modelled as a loss-free material having a relative permittivity of 1.1, close to that of air. Judging from the measured results, the radiation patterns from the simulations and measurements were approximately the same. This could indicate that the missing Divinycell did not affect the results substantially.

For future reference, the ground plane should be replaced with a wire approximation resulting in reduced wind resistance and weight, as well as a more manageable array. The layout must be re-designed in order to use the Divynicell support structure, which can be done by having all the arms of the crossed bowtie on the upper layer, using a soldering bridge to connect the center conductor to the opposite arm. Furthermore, since the thin copper layer on the FR4 substrate tends to oxidise, a thin coat of clear lacquer should be added on the elements.

6.2 Array prototype results

The usage of a simulation tool such as CST emphasizes the need to verify the results on a prototype, especially when the structure being simulated is only an approximation, which was the case here. The 5-element prototype array was built due to the limited space in the anechoic chamber at NTNU, and the hypothesis was that if the center element in a 5 element array would perform according simulations, then one can assume that the same applies for an 11-element array. This could serve as a motivation to build the full array.

As the measurements in the previous chapter shows, the simulated and measured performance of the center element in the 5-element array were almost identical in terms of co-polarization radiation pattern in both planes. The measured input reflection coefficient and mutual coupling to neighbouring elements both showed a positive frequency shift compared to the simulated results. It was suspected that the balun was the cause of this frequency shift, since this was the only part of the antenna which was left out from simulations in CST. Figure 6.1(a) and Figure 6.1(b) illustrates the differences between the two methods used to feed the antenna in CST and on the prototype respectively. The discrete face port used in CST (Fig.6.1(a)) spreads the excited signals evenly on the two edges of the bowtie triangles, where the two ports exciting the horizontally and vertically polarized bowties are completely isolated. Compared to the antenna excitation using the coaxial quarter-wave balun in Figure 6.1(b), there are some significant differences regarding effective point of excitation and port overlap.

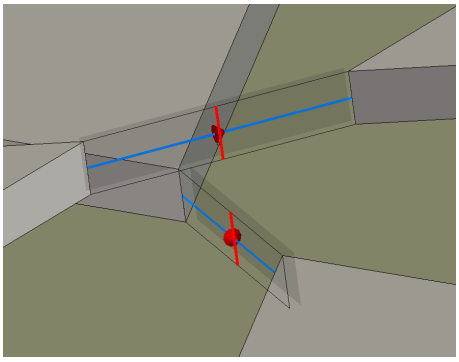

(a) CST bowtie feed

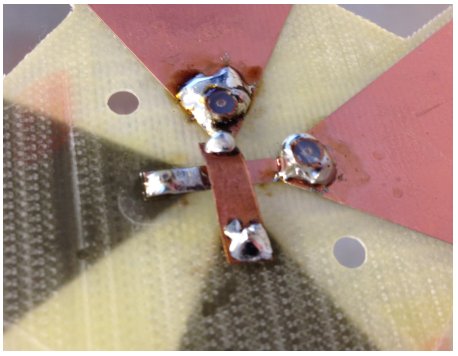

(b) Prototype balun feed

Figure 6.1: (a) shows the discrete face port excitation of the two bowties. (b) The bowtie feed of the prototype antenna

The effective feed points of the quarter-wave balun is somewhat difficult to determine, however as it can be seen from the figure the two bowtie triangles are not excited equally. The outer conductor of the coaxial cable is soldered to the bottom layer triangle and an extra piece of copper trace is used to connect the other triangle to the center conductor. Bailey used the same type of balun in his wideband bowtie antenna and points out that the triangle connected to the center conductor had to be slightly shorter than the other to compensate for the extra length the copper trace introduces to the antenna [33]. When the quarter wave balun is used in a crossed dipole antenna, the two extra copper traces have to cross each other, comparing this to the totally isolated ports in CST, one could expect that the mutual coupling between the crossed dipoles would be stronger, resulting in higher cross-polarization levels. A combination of the two may well be the source of the frequency shift and for future reference, the coaxial balun should be taken into account to investigate the effect this has on the resonance frequency of the antenna and the cross-polar coupling. Another type of balun which should be considered is the bazooka balun, as used in [34], which is a quarter wave metal sleeve encapsulating the coaxial cable that is shorted at the ground plane[7, p.539]. Furthermore, the feed gap between the bowtie triangles could be decreased to a point where the center conductor of the feed coaxial could simply be bent and soldered to the other triangle.

6.3 Design method

One of the goals of the thesis was to derive the design specifications for a DVB-T based passive bistatic radar. Whether dual polarized elements will prove useful is yet to be determined, but with basis in the measurement survey at FFI it may increase the probability of detection if the two polarizations could be used simultaneously or by switching between them, as mentioned.

Using CST Microwave Studio as design tool was proven very useful during the design phase. The user friendly CAD engine made modelling quick and simple, and with the adaptive mesh refinement system, good accuracy was obtained. However, none of the results obtained from simulations in CST was verified using another tool, in e.g. HFSS. As HFSS uses the finite element method as compared to the finite integration technique in CST, one can avoid pitfalls such as erroneous mesh settings leading to false results. Even so, the simulated and measured radiation pattern of the center element in the 5-element array were almost equal. This is taking simplifications in CST simulations and poor prototyping into account. With the obtained results from measurements, it is expected that the 11 element array prototype will have approximately the same performance as simulated. However for future reference the balun should be taken into account during simulations.

The choice of a suitable array element was solely based on the elements used in commercial PBR systems and those reported in literature. Furthermore, the decision was backed by the wideband bowtie element by Bailey[33] which was suggested as an array element in a wideband phased array. As there are no details available on the performance of the crossed wire bowtie in the Fraunhofer FHR CORA radar, no direct comparison can be made here. In addition, no other elements were considered in this thesis due to the limited time available. However, the results from this thesis indicate that the bowtie antenna may be a suitable array element for the DVB-T based passive bistatic radar. It should be mentioned that no conclusion on whether the level of mutual coupling in the array is too high for the digital beamforming and direction of arrival estimation algorithms. The effect of mutual coupling on these algorithms can be severe, especially on the estimation of DOA using the MUSIC algorithm [37]. Methods for mutual coupling compensation in antenna arrays exists [38], but whether the level of coupling in this array is too high for compensation is not known and should be investigated.

6.4 Suggestions for future work

The goal of this thesis was not to design an optimal array for the DVB-T based passive bistatic radar, however to serve as a first design iteration. There is still a lot of work which needs to be done regarding the phased array design, and suggestions for future work which may further increase the radar performance are presented.

6.4.1 11 element array

Only a 5 element array was built and measurements were in good correspondence with the simulated results on the same array in CST. If a full 11 element array is to be built, the issues related to the frequency shift in the prototype should be addressed first. Either by including the balun in CST simulations and increasing the total computational load, or by trial and error on produced elements. It is recommended that this issue is resolved by first characterizing the effect of the quarter-wave balun on a single element and see if the bowtie arms needs to have slightly different lengths to compensate for the solder bridge in the balun, as was pointed out in [33]. Or if a different type of balun should be used, such as the bazooka balun used in [34]

6.4.2 Adding another row of elements

The simulated beamwidth of the center elements in the vertical plane was over $120°$, which is more than the double of the required $45°$. In order to reduce the beamwidth in this plane and increase the directivity of the array, another row of elements can be added as discussed in the specifications chapter. Figure 6.2 shows how such an array could look, using the same inter-element spacing horizontally and vertically. From the array factor directivity in Figure 3.4, the half power beamwidth in the vertical plane would be approximately $60°$ when the column elements are excited simultaneously in-phase with uniform amplitude. In order to do this, a -3dB power splitter/combiner such as the Wilkinson divider [39]. With another row of elements the aperture of the array is doubled, resulting in a doubling in array directivity.

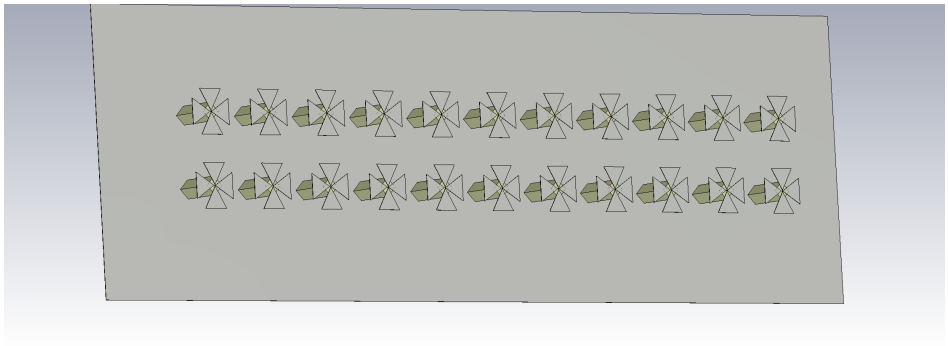

Figure 6.2: Future antenna array with two rows of elements where each column is excited simultaneously using a -3dB power splitter such as the Wilkinson divider

6.4.3 Active impedance matching, filter and LNA

According to Allen [8], the optimum receiver impedance to extract as much energy as possible from incoming plane waves is the same as the optimal generator impedance for an array transmitting in the same direction. Using the active reflection coefficient obtained from Equation (2.27), the optimal receiver impedance for broadside scan can be found for the center element. Since the mutual coupling between the elements is strong in this array, the active reflection coefficient is deteriorated, reducing the *realized* gain of each antenna. By matching each antenna element to the active reflection coefficient, the active impedance bandwidth may be increased and stay below the -10 dB limit in the desired frequency band.

It was mentioned that the antenna elements should be band limited to the DVB-T spectrum only due to the possibility of high power cellular base stations close to the passive radar receiver. In the frequency allocation plan from the Norwegian Post and Telecommunications Authority [40], the DVB-T broadcasting frequency band ends at 790 MHz where the slot between 790MHz and 862 MHz is reserved for mobile services. Experiments at FFI shows that these transmitters severely deteriorates the signal-to-noise ratio at the upper DVB-T channels. It is therefore suggested that a filter is added to the antenna, which should have low in-band losses and high attenuation at 790 MHz and up.

As filters, impedance matching networks and power divider circuits have losses it is suggested that a low-noise amplifier is added to the whole solution. With high gain and low noise figure, the losses from passive networks can be compensated for. Figure 6.3 illustrates how this may look, where the two antennas correspond to one column in the full two-row antenna array in Fig. 6.2. Obviously, there have to be one circuit like this for each polarization.

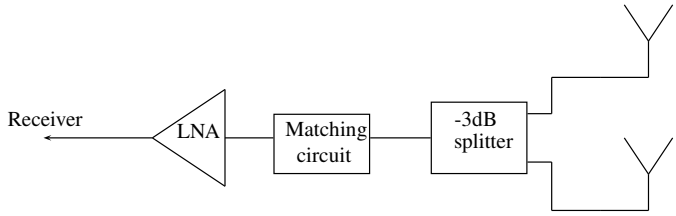

Figure 6.3

To further increase the complexity of the system, a switch network can be added to the two feed networks (one for each polarization), making it possible to switch between the two polarizations while doing measurements. One can then obtain both co- and cross-polar components of the target echoes, which may increase the chance of target detection.

Chapter 7

Conclusion

This thesis presents the design of a phased array antenna for a DVB-T based passive bistatic radar. The design specifications were derived based on the required sectoral coverage of the radar and transmitters in the vicinity of the Oslo fjord. Modelling and simulations were done in CST Microwave Studio.

An 11 element horizontal linear array with dual polarized crossed bowtie antennas was found suitable, resulting in maximum directivity and angular resolution in the horizontal plane where digital beamforming is to be performed. Simulation results on this array showed an impedance bandwidth of 624-748 MHz for the horizontally polarized elements and 600-800 MHz for vertically polarized, corresponding to DVB-T channels 40-55 for both polarizations. In terms of radiation patterns, the half-power beamwidth in the horizontal plane was 122° and 130° for horizontal and vertical polarization respectrively. In the vertical plane the corresponding beamwidths were 120° and 88°. These results fulfill the required 90° horizontal surveillance sector with a 45° vertical coverage. When the array was scanned, the grating-lobe free scan range was $\theta_s = \pm 50^\circ$ at the highest operating frequency of 750 MHz, where the active reflection coefficient at the center element was lower than -7dB throughout the whole band when scanned to this angle.

Due to size limitations of the anechoic chamber at NTNU only a 5-element prototype array was produced and measured. The objective was to compare results obtained from simulations on the same array and those from measurements to see the validity of the CST simulations. The results in terms of co-polar radiation patterns for the center element were almost equal to those obtained from simulations. One of the major differences was an increased cross-polarization level in the prototype, and a slight shift in the center frequency.

The measured impedance bandwidth of the center element was 660-800 MHz and 620-over 800 MHz for the horizontal and vertical polarization respectively. This is above the required bandwidth, however with a 30 MHz shift in center frequency which needs to be adjusted for in the next prototype. The cross-polar mutual coupling in the center element was approximately -27dB, and the mutual coupling to the neighbouring element was -12 dB and -10.7 dB for horizontal and vertical polarization respectively. In terms of radiation pattern for the center element at 674 MHz, the horizontal plane HPBW was 108° horizontal polarization and 130° for vertical polarization. In the vertical plane the corresponding beamwidths were 99° and 80.4°. The cross-polar radiation was at -23dB in both planes for vertical polarization. For the horizontal polarization the cross-polar radiation was -23dB in the E-plane and -17dB in the H-plane. A probable reason for the frequency shift was the fact that the quarter-wave balun used in the prototype was not included in CST simulations. An almost 50dB increase in cross-polarization and cross-polar coupling in the center element of the prototype was found, and the reason for this difference was again linked to the balun not being included in CST simulations.

To summarize, the results from measurements on the 5-element prototype array suggests that the simulation results in CST on the 11-element array could be expected from a full array prototype if the issue related to the shifted center frequency is sorted out. This antenna array could potentially be used as a sensor for a DVB-T based passive bistatic radar, covering channels 40-55 with a horizontal plane scan range of $\pm 50^\circ$ with both horizontal and vertical polarization. For future work, another row of elements in the vertical plane should be considered to further reduce the beamwidth in the vertical plane, resulting in higher antenna directivity and increased sensor detection range.

Bibliography

[1] K. E. Olsen. *Investigation of Bandwidth Utilization Methods to Optimise Performance in Passive Bistatic Radar*. PhD thesis, University of London.

[2] Wikipedia. Dowding system — Wikipedia, the free encyclopedia, 2014. [Online; accessed 24-May-2014].

[3] H. Griffiths and N. Willis. Klein heidelberg;the first modern bistatic radar system. *Aerospace and Electronic Systems, IEEE Transactions on*, 46(4):1571–1588, Oct 2010.

[4] N.J. Willis. *Bistatic Radar, Second Edition*. Institution of Engineering and Technology, 2005.

[5] Wikipedia. Passive radar — Wikipedia, the free encyclopedia, 2014. [Online; accessed 24-May-2014].

[6] Jonas Myhre Christiansen. Dvb-t based passive bistatic radar. Master's thesis, NTNU, 2010.

[7] C.A. Balanis. *Antenna Theory: Analysis and Design*. Wiley, 2012.

[8] J.L. Allen and B.L. Diamond. Mutual coupling in array antennas. Technical report, Massachusetts inst. of tech. Lexington Lincoln lab., 1966.

[9] G. H. Brown and O. M. Woodward Jr. Experimentally determined radiation characteristics of conical and triangular antennas. *RCA Rev.*, 1952.

[10] H. Kuschel. Approaching 80 years of passive radar. In *Radar (Radar), 2013 International Conference on*, pages 213–217, Sept 2013.

[11] K.E. Olsen and K. Woodbridge. Fm based passive bistatic radar range resolution improvement. In *Radar Symposium (IRS), 2011 Proceedings International*, pages 327–332, 2011.

[12] K.E. Olsen, K. Woodbridge, and I.A. Andersen. Fm based passive bistatic radar target range improvement - part ii. In *Radar Symposium (IRS), 2010 11th International*, pages 1–8, 2010.

[13] J.M. Christiansen and K.E. Olsen. Range and doppler walk in dvb-t based passive bistatic radar. In *Radar Conference, 2010 IEEE*, pages 620–626, 2010.

[14] M. Malanowski, K. Kulpa, and K.E. Olsen. Extending the integration time in dvb-t-based passive radar. In *Radar Conference (EuRAD), 2011 European*, pages 190–193, 2011.

[15] Karl Erik Olsen and Karl Woodbridge. Classification aspects of passive bistatic radar based on dvb-t. In *Radar Systems (Radar 2012), IET International Conference on*, pages 1–6, 2012.

[16] M. Cherniakov. *Bistatic Radars: Emerging Technology*. Wiley, 2008.

[17] H. Griffiths and C. Baker. The signal and interference environment in passive bistatic radar. In *Information, Decision and Control, 2007. IDC '07*, pages 1–10, 2007.

[18] P.E. Howland, D. Maksimiuk, and G. Reitsma. Fm radio based bistatic radar. *Radar, Sonar and Navigation, IEE Proceedings* -, 152(3):107–115, 2005.

[19] A.J. Fenn. *Adaptive Antennas and Phased Arrays for Radar and Communications*. Artech House radar library. Artech House, Incorporated, 2008.

[20] H. D. Griffiths. Passive bistatic radar and waveform diversity. Technical report, Cranfield University, 2009.

[21] *Introduction to Radar Systems*. Tata McGraw Hill, 2003.

[22] Historic American Engineering Record. Cape cod air station, technical facility-scanner building and power plant, massachusetts military reservation, sandwich, barnstable county, ma. In *Historic American Engineering Record (Library of Congress)*.

[23] A.K. Bhattacharyya. *Phased Array Antennas: Floquet Analysis, Synthesis, BFNs and Active Array Systems*. Wiley Series in Microwave and Optical Engineering. Wiley, 2006.

[24] R.J. Mailloux. *Phased Array Antenna Handbook*. Antennas and Propagation Library. Artech House, Incorporated, 2005.

[25] D.M. Pozar. The active element pattern. *Antennas and Propagation, IEEE Transactions on*, 42(8):1176–1178, Aug 1994.

[26] T. Hohne and V. Ranki. Phase noise in beamforming. *Wireless Communications, IEEE Transactions on*, 9(12):3682–3689, December 2010.

[27] D.W. O'Hagan, V. Basavarajappa, P. Knott, H. Kuschel, M. Ummenhofer, and M. Simeoni. A wideband antenna array for dvb-t based passive bistatic radar applications. In *Radar Systems (Radar 2012), IET International Conference on*, pages 1–6, 2012.

[28] M. Malanowski and K. Kulpa. Digital beamforming for passive coherent location radar. In *Radar Conference, 2008. RADAR '08. IEEE*, pages 1–6, 2008.

[29] F. Belfiori, S. Monni, W. van Rossum, and P. Hoogeboom. Antenna array characterisation and signal processing for an fm radio-based passive coherent location radar system. *Radar, Sonar Navigation, IET*, 6(8):687–696, 2012.

[30] Norkring. Dekningskart. `http://c-apps.nordeca.com/ntv/?location=rikstv&address=2007`, 2014.

[31] M.A. Richards, J.A. Scheer, J. Scheer, and W.A. Holm. *Principles of modern radar*. Number v. 1 in Principles of Modern Radar. SciTech Publishing, Incorporated, 2010.

[32] T.A. Milligan. *Modern Antenna Design*. Wiley, 2005.

[33] M.C. Bailey. Broad-band half-wave dipole. *Antennas and Propagation, IEEE Transactions on*, 32(4):410–412, 1984.

[34] Zengdi Bao, Xianzheng Zong, and Zaiping Nie. A novel broadband high-isolation cross dipole utilizing strong mutual coupling. In *Antennas Propagation (ISAP), 2013 Proceedings of the International Symposium on*, volume 02, pages 1237–1240, Oct 2013.

[35] CST - Computer Simulation Technology. *Antenna Arrays*. Application Note CST Studio Suite. September 2012.

[36] EMCOM. Double-ridged waveguide horn datasheet. `http://www.atecorp.com/ATECorp/media/pdfs/data-sheets/EMCO-3106-3115-3116_Datasheet.pdf`. [Online; accessed 02-June-2014].

[37] Benjamin Friedlander and A.J. Weiss. Direction finding in the presence of mutual coupling. *Antennas and Propagation, IEEE Transactions on*, 39(3):273–284, Mar 1991.

[38] Hoi-Shun Lui, Hon Tat Hui, and Mook-Seng Leong. A note on the mutual-coupling problems in transmitting and receiving antenna arrays. *Antennas and Propagation Magazine, IEEE*, 51(5):171–176, Oct 2009.

[39] E.J. Wilkinson. An n-way hybrid power divider. *Microwave Theory and Techniques, IRE Transactions on*, 8(1):116–118, 1960.

[40] The Norwegian Post and Telecommunications Authority. Norway, frequency allocations. `http://http://www.npt.no/teknisk/frekvens/frekvensstrategi-og-frekvensplan/informasjon-om-nasjonal-frekvensplan`, 2014. [Online; accessed 28-May-2014].